A new paradigm for the role of disturbance waves on heat transfer and dryout in annular two-phase flow

by

Roman W. Morse

A dissertation submitted in partial fulfillment of
the requirements for the degree of

Doctor of Philosophy
Mechanical Engineering

at the
UNIVERSITY OF WISCONSIN-MADISON (2023)

Date of final oral examination: 12/07/2023

The dissertation is approved by the following members of the Final Oral Committee:

Gregory F. Nellis, Professor, Mechanical Engineering
Arganthaël Berson, Lecturer, Mechanical Engineering
Allison Mahvi, Assistant Professor, Mechanical Engineering
Mark Anderson, Professor, Mechanical Engineering
Michael Corradini, Professor, Nuclear Engineering and Engineering Physics
Jean-Marie Le Corre, Engineering Fellow, Westinghouse
Kristofer M. Dressler, Teaching Professor, Mechanical Engineering

To Dress. In memory of Dress. Because of Dress.

Acknowledgements

To the late Dr. Kristofer Dressler (Dress)
Thank you, for everything. Thank you for introducing me to my passion, and for guiding me through my academic career. I really wish you could be here while I reach this milestone since you're almost solely responsible for setting it in motion. You would be proud of the work we have accomplished in the time you've been gone. I miss you and I love you big guy. I promise to always do my best to show enthusiasm and to get more people excited about math and science.

To the current MFVAL team
To Prof. Greg Nellis, thank you for being down-to-earth, a straight shooting, and a real-life wizard. You have been extremely consistent over the past year, and this has been vital to my successful completion of my doctorate. Thank you Prof. Arganthaël Berson, for among other things, teaching me how to write effectively. Thanks for being the rock to which we clung during times of chaos. I'm happy you're back. Finally, thanks to my PhD partner in crime, Jason Chan. You are truly the most widely-skilled, well-rounded engineer I know. It has been an absolute pleasure to work with you as a team mate.

The humble giants
Thank you Dr. Evan Hurlburt of the Naval Nuclear Lab.Your guidance during my time in the MFVAL has been absolutely invaluable. You have always encouraged the MFVAL team to investigate interesting behavior and to follow the science. Your positive attitude and belief in our research team have been unwavering. It has been a great pleasure to get to know you and to learn from you during my time in the MFVAVL. I would like to also say thank you to Dr. Jean-Marie Le Corre of Westinghouse Electric Sweden. You have chosen to spend your own free time working with Jason and myself on multiple projects. Not many people can enjoy spending an entire dinner (and two bottles of wine) discussing thermal hydraulics and answering my seemingly unending string of questions. Not sure anyone else in the world would be willing to debate nomenclature with me for several hours. Thank you both for taking an interest in the careers of both Jason and myself.

To Faculty within the ME department
Thank you Prof. Mark Anderson, for the interest that you have taken in my well-being after finishing my PhD. You went out of your way to offer me a recommendation and connect me with your peers. I am extremely grateful for this. Thank you Prof. Doug Reindl for taking the time to encourage me after I gave what was perhaps the worst presentation of my life during COVID era SEL talks. And for pulling strings in your world to help me find some

working fluid for my experiment. Thank you Prof. Jaal Ghandi for the manner in which you advised me during a time where I was extremely volatile. Thank you to Prof. Allison Mahvi, for allowing me to take part in research proposals and learn from you while in the process. Finally, thank you Prof. Alejo Roldan for the amount of love and compassion you show towards the Dressler family. I appreciate you for being just as quick to join in giving Dress a standing ovation after his talk at DresslerFest. I'm extremely grateful for how you offered to be my advisor after Dressler's passing. Thank you, and I will never forget this act of kindness.

To Former MFVAL

Without contributions from past MFVAL members, this work would again not have been possible. Thank you Dr. Tiago Moreira for being my Brazilian counterpart, and for the continuous stream of advice you provide me. Brian Fehring for sciencing in the lab with me for 8-10 hours at a time (jamming of course), and for greatly enhancing the integrity of the experimental facility. Thank you to fellow OG member of the new era MFVAL: James Doherty, Sydney Wagner, and Jared Valois. Finally, huge thanks to Dr. Tim Shedd and Dr. Mark Rodarte whose work established the MFVAL foundation. It is rather easy for me to stand on the shoulders of those who came before me. The experimental measurement techniques and procedures you developed have allowed for an incredible amount of insight into physical phenomena.

To Family

Thank you to my family. Thank you Mama for always encourage me to follow my dreams. Thank you for teaching me what it means to work hard, to be kind, and to care for others. Thank you Noah and Pups, for among other things, for coming to Madison and spending time with me. Thank you to my daily support team, Kylie and Nero. Thank you Kylie, for being my best friend, for doing your best to deal with my chaotic schedule, and for being my adventure partner. You inspire me on a daily basis, you make me smile, and you're a great panther mom. From the time Dress was diagnosed with cancer, I have been battling with cycles of deep depression. I am sorry that I relied so heavily on you during this time and did not seek out a mental health specialist. You carried me for a long time, and I'm sorry you had to experience me in this state. But you have been and continue to be a source of light in my life. I love you and I appreciate all that you do.

To Science

To the beautiful and mysterious universe, stay sexy.

Contents

List of Tables

List of Figures

Chapter 1

Introduction

1.1 Introduction

Flow boiling is an effective method for cooling high heat flux devices. In flow boiling, energy is transferred from the walls of a heated channel to a saturated fluid by a combination of forced convection and evaporation. A very important phenomenon that can occur during flow boiling is the onset of the boiling crisis, which is characterized by a severe reduction in heat transfer from the heated surface to the fluid and results in a rise in surface temperature. To prevent such situations, it is important to understand the mechanisms that lead to the boiling crisis.

In flow boiling systems, the fluid progresses through a series of flow regimes as vapor quality is increased. The process is visualized in Figure 1.1. The figure can be interpreted in two ways: (1) heat flux is constant and quality increases along the axis of the channel; or (2) the location is fixed and quality increases with increasing heat flux at the wall. As the vapor quality increases, the two-phase mixture progresses through the flow regimes until it reaches the annular flow regime. Annular flow is characterized by a vapor core, liquid film on the wall, and liquid droplets entrained within the core. Shear at the liquid-vapor interface drives the flow of the liquid film along the heated surface. A qualitative description of the heat transfer coefficient (HTC) between the channel wall and working fluid is shown in the

bottom of Figure 1.1.

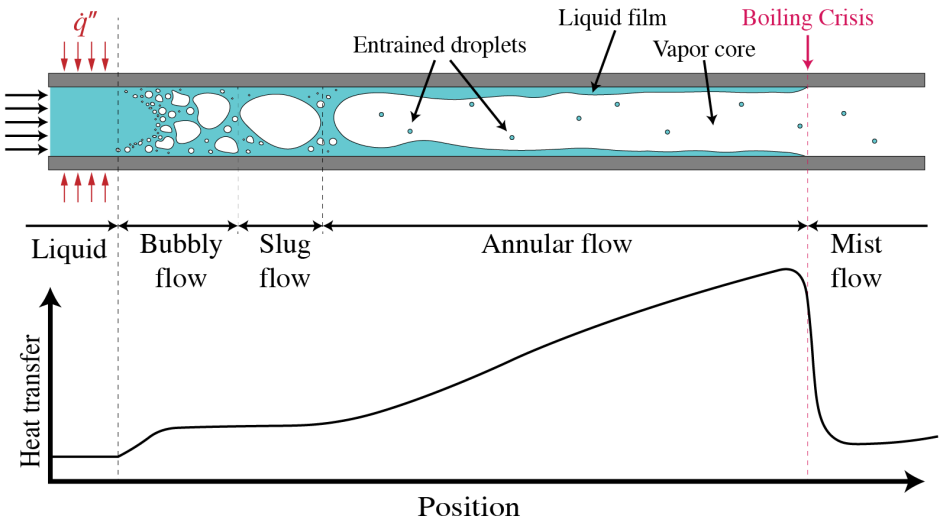

Figure 1.1: Flow boiling regime progression (top) and qualitative description of heat transfer coefficient (bottom).

1.1.1 Heat transfer in saturated flows

The heat transfer coefficient is the proportionality constant defined by Newton's Law of Cooling that relates the heat flux to the temperature difference between the fluid and heated surface:

$$h \triangleq \frac{\dot{q}"}{T_{wall} - T_{sat}} , \tag{1.1}$$

where $\dot{q}"_{eff}$ is the effective heat flux, T_{wall} is the heated surface temperature, and T_{sat} is the saturation temperature which is assumed to be the bulk temperature of the fluid under saturated conditions. In general, the two-phase HTC increases for increasing vapor quality. However, for each combination of local flow conditions, there exists a heat flux such that the local HTC reaches a maximum. Increasing the heat flux or vapor quality past this critical point results in a reduction in heat transfer coefficient.

1.2 Critical boiling transition

The critical boiling transition (CBT) occurs when a system goes from a flow regime with high HTC to a flow regime where the HTC is significantly lower Commission (2016). Note that the term 'critical boiling transition' is used in this paper following the latest terminology proposed by the United States Nuclear Regulatory Commission (NRC) Commission (2016). This is visualized in Figure 1.1 using a qualitative description of the HTC. The reduction in HTC corresponding to the CBT is largely due to one of two mechanisms depending on the flow conditions. The term critical heat flux (CHF) is used to generically describe the phenomenon associated with critical heat flux, departure from nucleate boiling and dryout.

1.2.1 Critical heat flux

It is necessary to define the nomenclature used to describe this work because nomenclature in the literature is inconsistent among authors. Table 1.1 contains different definitions for flow boiling CHF provided in the literature. The majority of the descriptions provided for flow boiling CHF in the literature have been qualitative. Only the final two entries in the table provide quantitative descriptions, neither of which can be used universally.

The inconsistencies throughout literature impede progress. This is another reason why CBT is preferred over CHF. However, the reader should be aware that they are referring to the same phenomenon.

1.2.2 Modes of critical boiling transition

Departure from nucleate boiling

For sub-cooled boiling flows and saturated flows at low vapor qualities the main heat transfer mechanism is nucleate boiling. In this regime, the CBT occurs when the flow departs from nucleate boiling (DNB), as vapor bubbles impede the ability of the liquid to rewet the surface. There is, however, no consensus on the detailed mechanism. Even so, significant

Author & year	Nomenclature	Definition
Collier and Thome (1994)	Critical heat flux	Heat flux at which, and local to a point, the characteristic reduction in HTC first occurs.
Nellis and Klein (2009)	Critical heat flux	The heat flux at which the burnout point occurs, a small increase in heat flux results in a large increase in excess temperature.
Shah (1987)	Critical heat flux	Exceeding this heat flux results in inefficient heat transfer and can result in the catastrophic failure of device.
Del Col and Bortolin (2012)	Onset of dryout	Temperature fluctuations due to the liquid-film dryout.
Kim and Mudawar (2013)	Critical heat flux	The point at which dryout completion is reached.
Borhani and Thome (2014)	Onset of critical heat flux	At CHF the liquid film covering a heated wall dries out, thus exposing the surface to the vapor flow; resulting in a significant drop in the HTC.
Nascimento et al. (2019)	Critical heat flux	Drastic reduction in HTC associated to the surface dryout, which implies a drastic increase in surface temperature.
Revellin et al. (2008)	Critical heat flux condition	Occurring when the interfacial wave amplitude is equal to the local film thickness, exposing the heated surface to the vapor core.
Wojtan et al. (2006)	Critical heat flux	$CHF = Aq_{max}$, $q_{max} = \rho_v i_{lv}\sqrt{RT/2\pi M}$, where $A = 0.1$ for water, and $A = 0.01$ for refrigerants.
Ong and Thome (2011b); Tibiriçá et al. (2012)	Critical heat flux	The heat flux that results in the surface temperature reaching a temperature that is 40 K greater than the saturation temperature.

Table 1.1: Different terms and definitions used to describe CHF in flow boiling

progress has been made recently in understanding the mechanisms leading to CBT during nucleate boiling Richenderfer et al. (2018). As a result, better heat transfer surfaces were designed, significantly increasing the value of heat flux at CBT in this flow regime Su et al. (2022). For high void fraction flow regimes, the CBT is associated with loss of liquid film, or dryout, which is the topic of this current work.

Liquid film dryout

For saturated flows in the annular two-phase regime, the reduction in local HTC is associated with the vaporization of the liquid film, broadly referred to as 'dryout'. Film dryout is the topic of this current work.

1.3 Dryout

Because of the inconsistencies found in the literature, it is necessary to clearly define, and expand, the nomenclature used to describe the dryout phenomenonMorse et al. (2024, 2023). The nomenclature in this work is consistent with that of Morse et al. (2024). Working definitions for terms related to dryout are the following:

- **Dryout** - a phenomenon in annular two-phase flow in which the liquid film is completely vaporized and the heated surface is exposed to the vapor core
- **Dryout event** - dryout at a local position lasting a finite amount of time, typically ending with the arrival of a disturbance wave
- **Cyclic dryout** - conditions in which successive dryout events are observed to occur between disturbance waves
- **Optimum Boiling Conditions (OBC)** - the boiling conditions that result in peak HTC
- **Intermittent dryout** - transitional flow regime between annular flow and mist flow; beginning with dryout inception, progressing to cyclic dryout, OBC, CBT, and eventually dryout completion
- **Dryout inception** - conditions in which the flow transitions from the annular flow regime to the intermittent dryout flow regime, where the first dryout events occur

- **Dryout completion** - conditions in which the flow transitions from the intermittent dryout flow regime to the mist flow regime; rivulets of liquid may be observed but a coherent liquid film no longer persists

Within the literature, many authors have modeled the dryout phenomenon with respect to vapor quality (Wojtan et al. (2005); Revellin et al. (2008); Del Col and Bortolin (2012); Marathe and Webb (2008); Kanizawa et al. (2016); Diani et al. (2018); Lillo et al. (2019); Kim and Mudawar (2013); Borhani and Thome (2014)). Authors have developed correlations for dryout vapor quality. However, new research has shown that the difference in vapor quality between the inception of dryout and the CBT is on the order of 1%. Morse et al. (2021) use a time-average dry fraction to characterize the HTC during intermittent dryout, which captures the change in HTC over the entire range of possible dry fractions (0 to 1).

Each flow condition of G, P, and x results in two-phase flows with varying characteristics such as void fraction, droplet entrainment, and most importantly to the annular regime, characteristics of the liquid film. The evolution of the liquid film along a heated surface is simplified in the schematic shown in Figure 1.2.

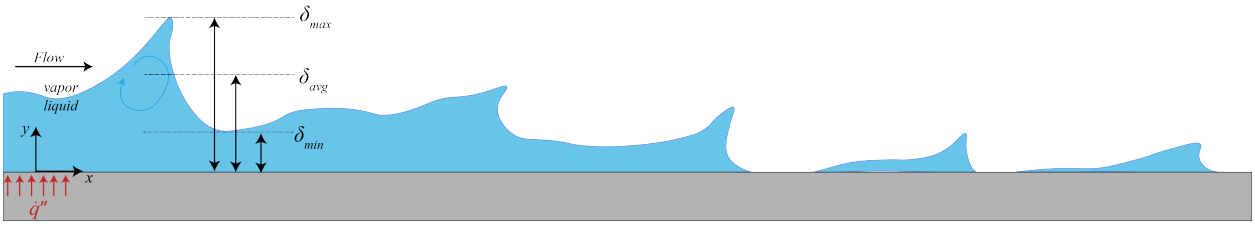

Figure 1.2: Schematic showing the evolution of the liquid film as it moves along the heated surface.

1.4 Purpose of this work

The general purpose of this research is to experimentally investigate phenomena associated with disturbance waves and to take a data-driven approach to mechanistic modeling efforts in order to predict dryout in a more robust way.

Chapter 2

Literature review

2.1 Liquid film and waves in annular flow

2.1.1 Introduction

Hewitt (1969) performed flow visualization and was able to record an axial view of the flow field under annular flow conditions. Using a combination of experimental measurements and direct observation, Hewitt (1969) established two distinct types of wave structures within the liquid film: disturbance waves and ripples. The schematic in Figure 2.1 illustrates the fundamental properties of both disturbance waves and ripples. The ripples exist in the base film region and can be seen in the figure as small oscillations at the liquid-vapor interface. Ripples act as waves in the traditional sense, meaning ripples transport energy and not mass. Ripples are continuously being generated at the interface, due in large part to droplets hitting the surface; rain droplets hitting the surface of a lake create ripples in the same manner. The ripples propagate outwards and eventually dissipate due to viscous forces (Hewitt (1969); Borhani et al. (2010)). In general, ripples and other minor perturbations at the liquid-vapor interface have almost no impact on the overall, or time-averaged, flow conditions.

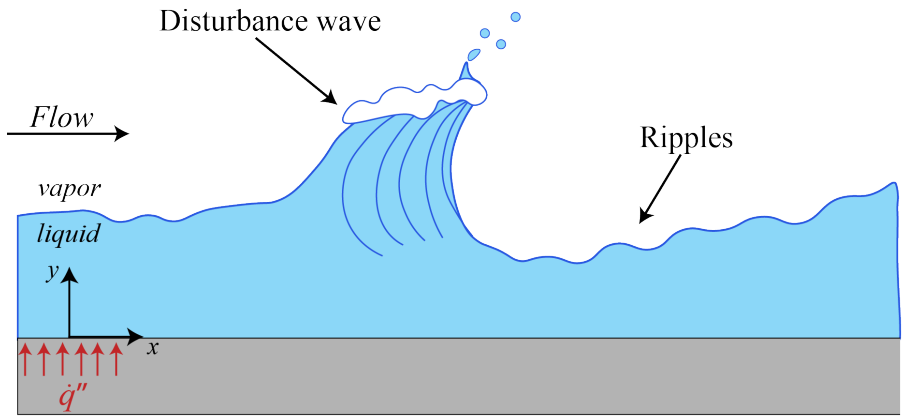

Figure 2.1: Illustration showing the two different wave classifications: disturbance waves and ripples.

Disturbance waves, on the other hand, are the dominant structure of the flow in two-phase annular flow. The liquid film is typically on the order of microns and experiences large shear stress at the liquid-vapor interface due to friction between the relatively slow liquid and relatively fast vapor. The shear stress causes the liquid film to stack up into structures, called disturbance waves, that look similar to ocean waves. The disturbance waves are identified as a structure because they contain a relatively large mass of fluid traveling at a similar velocity. Under annular flow conditions, disturbance waves have large wave heights, with amplitudes on the same order of magnitude as the mean liquid-film thickness. The images provided by Hewitt (1969) confirm the presence of turbulent characteristics in the disturbance waves. The turbulent characteristics of the waves include the creation and dissipation of vortices at varying length scales, obvious mixing with the rolling waves, and the overall stochastic behavior of the waves.

Wave characteristics

Hewitt (1969) was one of the first authors to provide experimental measurements of wave velocity and frequency of disturbance waves. The author found that for all flow conditions, the velocity of the disturbance waves is greater than the average velocity of the liquid phase. In general, for increasing flow rate (liquid or vapor) there is an increase in wave velocity and

wave frequency. In fact, Hewitt (1969) found that for any flow conditions that result in the same mean liquid-film thickness, the distance between wave crests, or the wavelength, L_{wave}, was constant:

$$L_{wave} = \frac{u_{wave}}{f_{wave}} \approx \text{Constant} \tag{2.1}$$

where u_{wave} and f_{wave} are the wave velocity and frequency, respectively. Under the flow conditions shown in the Figure 2.3, the distance between waves is

$$L_{wave} = \frac{u_{wave}}{f_{wave}} = \frac{1.5 \text{ m/s}}{15 \text{ Hz}} = 0.10 \text{ m}$$

.

2.1.2 Modeling as turbulent boundary layer

Due to the visible turbulence in the waves, most efforts to model the velocity profile of the liquid film have treated the problem as a turbulent boundary layer (TBL) and employed the wall-bounded flow theory equations (Dobran (1983); Hurlburt and Newell (1996)).

Wall shear, τ_{wall}, is the normalizing quantity that must be known in order to normalize the problem into wall units. In general, τ_{wall}, is calculated as

$$\tau_{wall} = \tau_{int} - \frac{dP}{dz}\delta + \rho_l g_z \delta \tag{2.2}$$

where $\frac{\mathrm{d}P}{\mathrm{d}z}$ is the stream-wise frictional pressure gradient, δ is the mean liquid-film thickness, ρ_l is the density of the liquid phase, g_z is gravitational acceleration, and τ_{int} is the interfacial shear that results from friction at the liquid-vapor interface. In the case of vertical upwards flow, g_z = - 9.8 m/s. The τ_{int} can be estimated by

$$\tau_{int} = \frac{1}{2}\rho_v u_v^2 f_{int} \tag{2.3}$$

where ρ_v is the density of the vapor phase, and u_v is the time-average bulk vapor velocity. The interfacial friction factor, f_{int}, has been correlated by previous authors, most recently Moreira et al. (2020). The Wallis-type friction factor correlation is,

$$f_{int} = 0.005 \left(1 + 300 \frac{\sigma_\delta}{D_h}\right) \tag{2.4}$$

where σ_δ is the standard deviation of the liquid film thickness, and D_h is the hydraulic diameter. Substituting Equations 6.11 and 6.10 into Equation 2.2 provides an estimate for τ_w, the normalizing parameter.

The problem is normalized in the manner described by Pope (2000). The friction velocity, u^*, is calculated as

$$u^* = \sqrt{\frac{\tau_w}{\rho_l}} \,. \tag{2.5}$$

The normalized distance from the wall, y^+, and normalized liquid-film thickness, δ^+, are calculated as

$$y^+ = \frac{y u^*}{\nu_l} \; ; \; \delta^+ = \frac{\delta u^*}{\nu_l} \quad \text{with } y \in [0, \delta] \tag{2.6}$$

where y is the distance from the wall, and $\nu_l = \frac{\mu_l}{\rho_l}$ is the dynamic viscosity of the liquid phase. Finally the thickness of the viscous sublayer, δ_{vs}, is estimated as

$$\delta_{vs} = \frac{y^+_{vs} \nu_l}{u^*} \tag{2.7}$$

where y^+_{vs} is the size of the viscous sublayer in wall-units. For fully developed turbulent boundary layers, the size of the viscous sublayer is $y^+ = 5$.

Shortcomings of TBL approach to liquid film

Traditional universal velocity profiles, such as von Karman, Spalding, or Van Driest, are not a good description of the liquid film. As stated previously, any of the turbulent features

in the liquid film are related to waves. In addition, the fluid in the wake region of disturbance waves has been observed to be nearly stagnant (Morse et al. (2021)). This flow behavior is inconsistent with the assumptions made in order to obtain the TBL equations.

2.1.3 Wave-base approach

Direct observation and liquid-film thickness measurements have identified two predominant features within shear-driven liquid films: the base film and disturbance waves (Hewitt (1969); Dobran (1983); Moreira et al. (2020); Morse et al. (2021)). The base-film is the fluid that is near the interface with a surface. Viscous interaction dominates the fluid motion within the base film. The base film serves as the lubricating layer for the disturbance waves to travel downstream. The disturbance waves apply a shear to the fluid in the base film and accelerate the base film in the streamwise direction. When exposed to the vapor, the liquid-vapor interface possesses ripples (or capillary waves) but is otherwise very smooth. Droplets are deposited in the base film, but no droplets are detached from the base film region.

The disturbance waves that occur in two-phase annular flow are the result of large velocity gradients, or shear, at the liquid-vapor interface; this defines the waves as Kelvin-Helmholtz in type. The liquid in the wave crests has high velocity, and under certain conditions, mass from the crests is transported directly to the slow-moving base film ahead of the wave. A significant amount of liquid mass is stored in the wave crests, and the disturbance waves are the dominant source of liquid-mass transport in the stream-wise direction (Moreira et al. (2020), Morse et al. (2021)).

Recently, Le Corre (2022) presented a mechanistic model using a wave-base treatment for the liquid film. The model is a 4-field, transient, and 1-dimensional model; the four fields are the vapor core, liquid droplets, the base film, and the waves. The model of Le Corre (2022) (outlined in the next section) is capable of predicting downstream liquid-film characteristics along a heated length. In order to accurately predict the downstream liquid-

film characteristics, the model includes terms that describe different modes of mass transport that within the system depending on the local flow conditions. On the far left of Figure 2.2 is a region labeled wave-base transport. Within this region, the base-film thickness remains relatively constant, as the waves continue to provide mass to the base film until the waves are no longer fast enough to catch up with the evaporating front, and/or excess mass in the wave crests has been depleted. The interaction between the base and wave regions is of particular interest to this study. Figure 2.2 illustrates this type of framework.

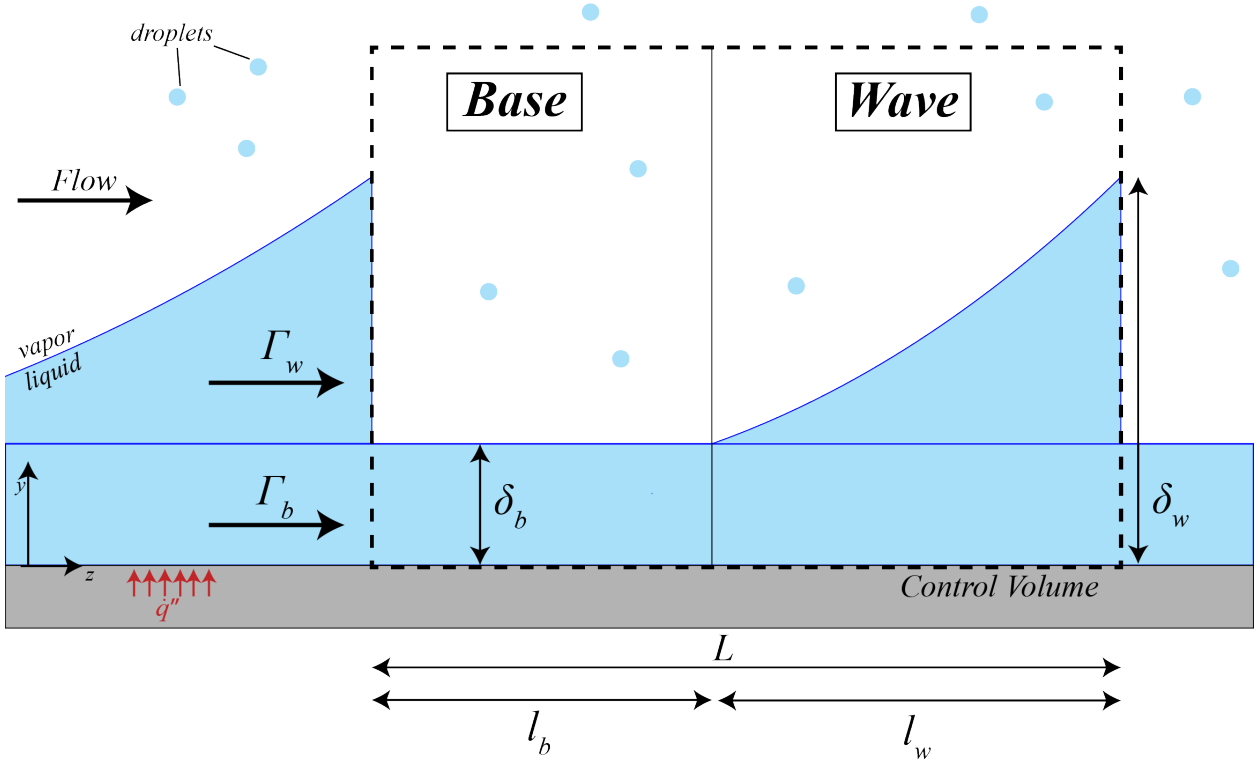

Figure 2.2: Schematic showing the wave and base components of liquid film.

2.1.4 Shortcomings of available experimental data

One issue with currently available experimental data related to disturbance wave characteristics is that most of it is produced in facilities that use air-water two-phase flows (Dobran (1983); Hurlburt and Newell (1996), Schubring et al. (2010)). The air-water interface is simplified compared to a single-species saturated fluid, which possesses a phase change

in addition to the already complex wave features. Only recently have researchers been able to study disturbance wave characteristics in single species two-phase flows (Moreira et al. (2020)). However, the experiments were performed for adiabatic flow conditions only. More studies of this study type must be performed for flows under heated conditions.

2.1.5 Liquid film descriptions - summary

The predominant wave structures in annular flow are ripples and disturbance waves. The ripples have little impact on the overall flow and show no turbulent features. The disturbance waves dominate the motion of the liquid mass and possess turbulent features such as mixing and generation of vortices. The velocity and frequency of the waves is difficult to predict and seem to be dependent on flow configuration. However, the ratio u_{wave}/f_{wave} remains relatively constant for any flow conditions (G and x) that result in the same mean liquid-film thickness.

Traditional turbulent boundary layer treatment is insufficient for the velocity profile of the liquid film. The disturbance waves possess some turbulence, and therefore the treatment may be appropriate during the passage of a wave. However, the wake regions possess no turbulent features and therefore are misrepresented by the use of these models. Therefore, a wave-based approach is preferred because it more accurately describes the underlying physics governing the liquid-film behavior.

2.2 Dynamic behavior of disturbance waves

2.2.1 Adiabatic conditions

The passage of a disturbance wave in unheated conditions can be seen in Figure 2.3. The dark areas of the figure correspond to the wave crest, where turbulent characteristics such as liquid detachment and rolling waves are present. For the adiabatic case, the disturbance wave frequency is observed to be approximately 15 Hz and the velocity of the waves is between 1

- 2 m/s.

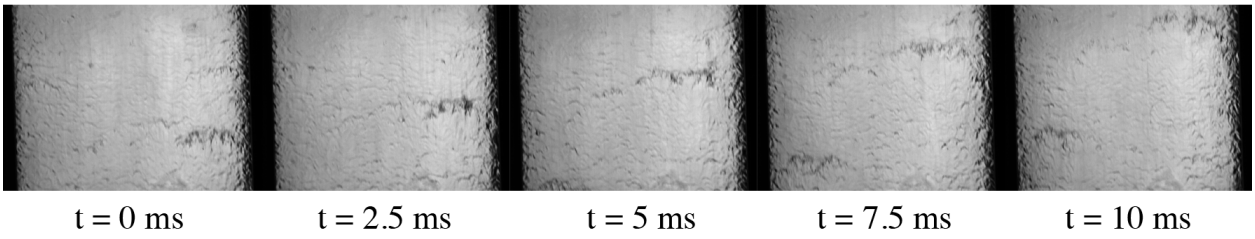

Figure 2.3: Disturbance wave passing in adiabatic conditions over the sequence of 5 images, $G = 167.4$ kg/m^2-s, $X_{local} = 0.765$, $\dot{q}''_{eff} = 0$ kW/m^2

The images in Figure 2.4 capture the flow for unheated conditions and same mass flux, but for higher vapor quality than the data set shown in Figure 2.3. The height of the waves as well as the turbulent characteristics are reduced under higher vapor quality and lower film thickness flow conditions. The average wave velocity is around 1 m/s and frequency of the waves was observed to be approximately 15 Hz, the same as for the previous case. The observed wave velocity and wave frequency for the adiabatic cases agree with the previous observations made in Moreira et al. (2020).

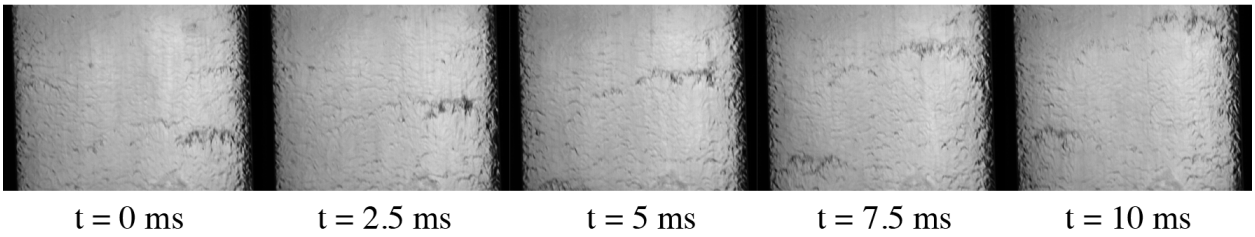

Figure 2.4: Disturbance wave passing under adiabatic conditions: $G = 167.4$ kg/m^2-s, $x_{local} = 0.86$, $\dot{q}''_{eff} = 0$ kW/m^2

2.2.2 Heated conditions

Figure 2.5 shows the passage of a disturbance wave for a heated case with effective heat flux of $\dot{q}''_{eff} = 30.7$ kW/m^2. The mass flux is again the same, and the local vapor quality in the heated case is very near that of the unheated case shown in Figure 2.4. The wave velocity and amount of turbulence was observed to be similar to the adiabatic flow conditions with

the same vapor quality. However, the waves in the heated case are observed to break up into smaller wave segments that travel slightly upstream or downstream from the other segment. In addition, the frequency of the disturbance waves for the heated case is between 3-5 Hz, much lower than that of the adiabatic case. There is a fundamental change in the behavior of the waves when heating is applied to the liquid film.

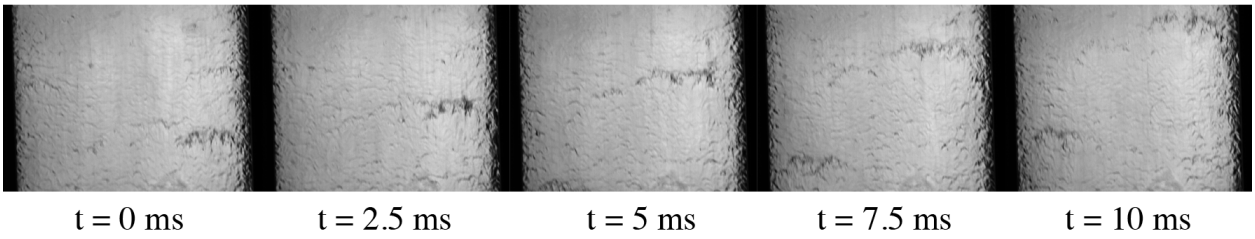

Figure 2.5: Disturbance wave passing under heated conditions: $G = 167.4$ kg/m^2-s, $x_{local} = 0.85$, $\dot{q}''_{eff} = 30.7$ kW/m^2

2.3 Heat transfer coefficient

2.3.1 Introduction

The combined two-phase HTC, h, follows Newton's Law of Cooling, and can be measured experimentally as,

$$h = \frac{\dot{q}''}{T_w - T_{sat}} \tag{2.8}$$

where $\dot{q}''$ is the heat flux into the fluid from the heated surface, T_w is the temperature heated surface, and T_{sat} is the saturation temperature of the bulk fluid. The temperature of the bulk fluid remains constant during saturated flow boiling. Therefore, a proper assumption is that all the heat input into the two-phase mixture is utilized by converting liquid to vapor.

The two mechanisms for generating vapor are: nucleate boiling at the wall-liquid interface, and convective boiling which leads to vaporization at the liquid-vapor interface. Chen (1966), and many other authors since, have modeled the combined two-phase HTC, h, as a

sum of the contributions from nucleate boiling and convective boiling:

$$h = h_{nb} + h_{conv} \tag{2.9}$$

where h_{nb} and h_{conv} are the nucleate boiling and convective HTC, respectively. Under the flow conditions that are of interest to this current study the contribution from nucleate boiling is negligible, i.e. $h_{nb} \to 0$.

Significant progress has been made recently in understanding the mechanisms of nucleate boiling (Galloway and Mudawar (1993)). As a result, better heat exchangers have been designed to take advantage of this new physical understanding (Zhang et al. (2012); Ahn et al. (2010)). However, a proper understanding of mechanisms that govern heat transfer associated with convective vaporization remains elusive. For this reason, the focus of this study is heat transfer in saturated systems with vaporization as the main mode of phase change.

2.3.2 Modeling

Modeling efforts can generally be sorted into three categories: empirical, semi-empirical, and mechanistic. Many versions of empirical and semi-empirical models exist; one of each variety is reviewed in this current work. The empirical method used by Chen (1966) and the semi-empirical approach of Dobran (1983) have provided the foundation for many modeling efforts since. Each of the correlations was originally produced for vertical flows in conventional-sized channels ($D_h > 6$ mm).

Dimensionless quantities

It is useful to define dimensionless quantities that naturally occur in the analysis of thermo-fluids problems, such as the Reynolds and Prandtl numbers. The Reynolds number,

Re, is defined as

$$\mathrm{Re} = \frac{\rho u d}{\mu} \tag{2.10}$$

where ρ is fluid density, u is the velocity, d is a characteristic length and μ is the viscosity of the fluid. The Prandtl number is defined as

$$\mathrm{Pr} = \frac{\mu}{\rho}\frac{\rho c}{k} = \frac{\nu}{\alpha} \tag{2.11}$$

where ν is the kinematic viscosity of the fluid and α the thermal diffusivity. Finally, the Nusselt number, Nu, is defined as

$$\mathrm{Nu} = \frac{h d}{k} \tag{2.12}$$

where h is the local HTC, d is a characteristic length, and k is the thermal conductivity of the fluid. The output of heat transfer correlations is a predicted Nusselt number, $\mathrm{Nu}_{\mathrm{pred}}$. The predicted two-phase HTC, h_{pred}, can then be calculated as,

$$h_{\mathrm{pred}} = \left(\frac{k}{d}\right) \mathrm{Nu}_{\mathrm{pred}} \, . \tag{2.13}$$

Chen (1966)

Many empirical correlations exist for HTC in two-phase flows, each developed using a database containing varying flow conditions and working fluids. One of the earliest and simplest two-phase HTC correlations is that of Chen (1966), who proposed a modified single-phase correlation of Dittus and Boelter (1930).

The Dittus and Boelter (1930) correlation predicts a Nusselt number for turbulent single-phase flows,

$$\mathrm{Nu}_{DB} = 0.023 \, \mathrm{Re}^{0.8} \, \mathrm{Pr}^{0.4} \, . \tag{2.14}$$

The Dittus and Boelter (1930) prediction for HTC is,

$$h_{DB} = \left(\frac{k}{d}\right) 0.023 \ \mathrm{Re}^{0.8} \ \mathrm{Pr}^{0.4} \ . \tag{2.15}$$

The Dittus and Boelter (1930) correlation has been shown to work consistently for a wide variety of single-phase flow conditions. Chen (1966) proposed for the correlation convective portion of the two-phase HTC. The correlation uses a modified Dittus-Boelter expression:

$$h_{\mathrm{pred}} = h_{\mathrm{DB},l} \, \mathcal{F}$$

where $\mathcal{F}$ is a two-phase factor. The two-phase heat transfer factor, $\mathcal{F}$, is proposed to be

$$\mathcal{F} = \left(\frac{\mathrm{Re}_{2p}}{\mathrm{Re}_l}\right)^{0.8} \tag{2.16}$$

where Re_l is the Reynolds number of the liquid phase, and Re_{2p} is the two-phase Reynolds number. A minimization of error against a database was used to determine the exponent of 0.8 in the expression for $\mathcal{F}$. The liquid Reynolds number is,

$$\mathrm{Re}_l = \frac{dG(1-x)}{\mu_l}$$

where x is the vapor quality of the two-phase mixture, and G is the two-phase mass flux. The two-phase Reynolds number is calculated as

$$\mathrm{Re}_{2p} = \frac{\rho_l D}{\mu_l} \frac{G}{\overline{\rho} A_c}$$

where A_c is the cross sectional area of the flow channel, and $\overline{\rho}$ is the average two-phase mixture density ($\overline{\rho} = x\rho_v + (1-x)\rho_l$). Finally, the correlation of Chen (1966) provides

$$h_{\mathrm{Chen}} = 0.023 \mathrm{Re}_l^{0.8} \mathrm{Pr}_l^{0.4} \frac{k_l}{D} \mathcal{F} \tag{2.17}$$

as an estimate for the convective HTC in two-phase systems. As stated previously, Chen (1966) is but one of many correlations of this type. The performance of this type of correlation is heavily reliant on the database source from which it was developed. Increasing the amount of experimental data available will make these type of correlations more robust.

Dobran (1983)

A semi-empirical (or semi-mechanistic) correlation is one that attempts to model the system using first principles, but eventually will require empirical correlation(s) for closure. An example of a semi-empirical model is that of Dobran (1983), who hypothesized that the liquid film in annular flows act as a turbulent boundary layer.

Liquid-film thickness measurements and direct observations under two-phase annular flow conditions have established two predominant structures in the liquid film: disturbance waves and ripples in a base region of the film (Hewitt (1969)). Dobran (1983) incorporated this observation to better capture the actual physics governing the two-phase heat transfer. A turbulent form of Fourier's Law can be written as

$$\dot{q}'' = -\left(k_l + \rho_l c_l \varepsilon_H\right) \frac{\partial T}{\partial y} \tag{2.18}$$

where c_l is the heat capacity of the liquid phase, and ε_H is the eddy-diffusivity of heat. A partial differential equation that describes the temperature gradient through the liquid film can be obtained by normalizing the problem. The governing energy equation then becomes,

$$1 = \frac{\partial T^+}{\partial y^+} \left(\frac{1}{\mathrm{Pr}_l} + \frac{\varepsilon_H}{\nu_l} \right) . \tag{2.19}$$

where y^+ is the normalized distance from the wall, and T^+ is the normalized temperature. Dobran (1983) proposed that for the wave regions, where $\delta_b < \delta$, the equation can be written in the form of,

$$1 = \frac{\partial T^+}{\partial y^+} \left(\frac{\mu_{eff}}{\mu_l} \frac{1}{\mathrm{Pr}_{eff}} \right) . \tag{2.20}$$

The turbulent contributions are a function of the normalized film thickness, δ^+. For base layer regions, Dobran (1983) proposes,

$$\frac{\varepsilon_H}{\nu_l} = \begin{cases} 0 & \text{, if } 0 < y^+ \leq 5 \\ \frac{1}{5}y^+ - 1 & \text{, if } 5 < y^+ \leq 30 \\ \frac{5}{2}y^+ - 1 & \text{, if } 30 < y^+ \leq \delta_b^+ \end{cases} \tag{2.21}$$

and for wave regions

$$\frac{\mu_{eff}}{\mu_l} = 1 + \mathcal{C}\left(\delta^+ - \delta_b^+\right)^n \quad \text{if } \delta_b^+ < y^+ \leq \delta^+ \tag{2.22}$$

It should be noted that the thickness of δ_b is much larger than the typical viscous sublayer, and Dobran (1983) states the value will need to be determined through future experiments. In addition, the term provided for the turbulent contribution in the wave region is purely empirical, and the constants have been determined through a curve fit process($\mathcal{C} = 1.6 \times 10^{-3}$ and $n = 1.8$). The time-averaged HTC is obtained by weighting the contributions of the waves and base regions with the temporal fraction of each.

2.3.3 HTC - summary

In general, empirical and semi-empirical models utilize historical databases to make predictions. Meanwhile, models of a mechanistic nature are capable of describing physics occurring in an arbitrary situation. Empirical correlations are needed in order to safely operate systems that take advantage of underlying physics which has yet to be properly understood. Discovering a method for accurately modeling the physics will lead to enhanced heat transfer surfaces in a wide range of industrial applications.

Chapter 3

Experimental

3.1 Experimental apparatus

In this experiment, a two-phase annular flow with known enthalpy enters a test section with electrically heated walls. A simple thermal resistance model is employed to account for energy losses, allowing for accurate prediction of the amount of energy transferred to the two-phase fluid and enabling calculations of outlet enthalpy and vapor quality.

Figure 3.1 shows a schematic of the experimental annular flow facility. The working fluid in the two-phase annular flow loop is R-245fa (1,1,1,3,3-pentafluoropropane, Honeywell), a low-pressure refrigerant that possesses fluid properties similar to that of high-pressure steam. The fluid is driven through two circuits, one for vapor and the other for liquid, which combine at the inlet of the developing section to create a two-phase annular flow. The fluid within the vapor circuit starts in the storage tank where the pressure (Omega PX409, 0-344.74 kPa) and temperature (Omega Type K) of the fluid are monitored. From the storage tank, the fluid is driven through the loop by a gear pump (Micropump GJ-N27). Upstream of the pump, there is a plate heat exchanger supplied with cold water (T_{cold} = 10 °C) that is used to cool the fluid below the saturation temperature and avoid cavitation in the pump. Downstream of the pump, the fluid passes through a Coriolis flow meter (Micro Motion F025) and an electronic proportional control valve (Omega ECV-2506-4X). The mass flow rate from the Coriolis flow

meter is read into LabView where a PID controller maintains a specified and constant mass flow rate. After the flow meter, the fluid is evaporated and superheated in a plate heat exchanger supplied with hot water ($T_{hot} = 40$ °C) before entering the flow loop at the vapor inlet. Liquid from the storage tank goes through an identical circuit, without a vaporizing heat exchanger. At the mixing tee, the subcooled liquid from the liquid circuit is injected into the flow through small holes in the channel wall to minimize droplet entrainment and induce annular flow, thus reducing the required two-phase flow development length. Temperature (Omega Type K) and pressure (Omega PX409, 0-344.74 kPa) of the liquid and vapor flows are measured at the inlet and again at the outlet of the mixing tee.

Downstream of the mixing tee, the flow channel transitions smoothly from a 1-inch diameter copper pipe to a stainless steel rectangular channel. It is followed by an insulated channel with length 150 times that of the hydraulic diameter, $D_h = 18$ mm to achieve fully developed flow Zhao et al. (2013). The test section consists of an Ultem (polyetherimide) plastic frame, aluminum plates, and two windows coated with a layer of fluorine-doped tin oxide (FTO) thickness around 450 nm (estimated by the manufacturer). The flow channel cross section is 36 mm x 12 mm and the heated length is equal to the length of the windows, 0.525 m. By passing an electric current through the FTO coating, the inner wall of the test section can be heated. Constant electrical power is supplied to the windows by two 6 kW Xantrex-XDC power supplies. The uniformity of heating at the windows was verified by measuring the temperature field in the absence of flow with an infrared camera.

The bulk fluid temperature within the test section is measured at four locations using Omega Type E thermocouples with a bare junction of 0.076 mm. The thickness of the liquid film is on the order of tens of microns and is inherently unstable. It is important that any instrumentation within the test section be installed in such a manner as to minimize disruption to the liquid film. To accomplish this, a volume is hollowed out of the Ultem midsection and a plug is inserted into the volume. The circular plug has a small slit across the diameter and the thermocouple is placed within the slit. It was verified that the thermocouples do not

protrude into the flow channel using calipers. Each of the thermocouples is calibrated using a refrigerated water circulator to an average uncertainty of 0.05 °C. After calibration, it was verified that the thermocouples accurately measured the saturation temperature calculated from the test section absolute pressure sensor.

Pressure drop measurements are made along the test section using a slow but very accurate sensor (Rosemont 3051cd 0-4.982kPa, response time $\sim$ 700 ms and uncertainty of 7 Pa) and also a fast, less accurate model (Omega PX409-2.5DDUI, response time $\sim$ 1 ms and uncertainty of 70 Pa). A non-invasive optical technique primarily used to measure inner wall temperature is adapted and used to indicate dryout Fehring et al. (2020). High-speed video is taken at the same location as the film thickness using a Phantom V311 high-speed camera at 4000 fps. Using the same camera, a non-invasive optical method is used to measure liquid-film thickness at a frequency of 4000 Hz Hurlburt and Newell (1996); Shedd and Newell (1998); Moreira et al. (2020). The location of these measurements is near the top of the test section. After leaving the heated test section, the fluid enters a separation tank that acts as a buffer and prevents large pressure oscillations in the test section. The fluid condenses in a plate heat exchanger supplied with cold water and then reenters the storage tank.

Temperatures within the loop are controlled with a separate water/glycol loop. A 10 kW heat pump (Trane WPWD07230D22000T) and a 17 kW heat pump (Trane EXWE06011) extract energy from the cold water side and provide it to the hot water side. The heat pumps are controlled via process controllers (OmegaCal9400). The water/glycol mixture from an 189 L cold reservoir is pumped through counter-flow heat exchangers to condense and cool the refrigerant in the two-phase loop. Water/glycol mixture from a 76 L hot side reservoir is pumped through a single counter-flow heat exchanger where the heat vaporizes the refrigerant.

A data acquisition system from National Instruments and a personal computer is used to control and monitor the experimental apparatus and record the data. This data acquisition

system consists of a chassis model cDAQ-9179, a NI-9401 digital module, two NI-9203 current input modules, two NI-9263 voltage output modules, a NI9205 voltage input module, two NI-9213 temperature input modules, and a NI-9215 voltage series input module. An interface program was developed in LabVIEW National Instruments (2019) to control and monitor the experimental apparatus and record the data. Process data is sampled at 2000 Hz.

Two-phase calculations

For two-phase flow conditions, an energy balance is performed on the mixing tee to determine the specific enthalpy of the saturated mixture, i_{tp}. The enthalpies of both the slightly superheated vapor phase, $i_{v,sh}$, and slightly subcooled liquid phase, $i_{l,sc}$, are known through measurements of temperature and pressure prior to the two-phase mixing tee. The enthalpy of the two-phase fluid that exits the mixing tee is given by

$$i_{tp,in} = \frac{\dot{m}_v i_{v,sh} + \dot{m}_l i_{l,sc}}{\dot{m}_v + \dot{m}_l} \ , \tag{3.1}$$

where $\dot{m}_v$ and $\dot{m}_l$ are the vapor and liquid mass flow rates, respectively. The development section immediately following the mixing tee is well insulated and the two-phase mixture is near ambient temperature. It has been verified through an energy balance on the single-phase flow that the heat losses through this section are negligible. Therefore the enthalpy of the fluid entering the test section is equal to that leaving the mixing tee. The vapor quality at the inlet of the test section is calculated as

$$x_{in} = \frac{i_{\mathrm{tp,in}} - i_{l,sat,in}}{i_{v,sat,in} - i_{l,sat,in}} \ , \tag{3.2}$$

where $i_{v,sat,in}$ and $i_{l,sat,in}$ are the enthalpies of saturated vapor and liquid, respectively, evaluated at the saturation pressure at the inlet of the test section. The enthalpy of the two-phase fluid at the outlet of the test section is calculated with an energy balance on the fluid moving

through the test section:

$$i_{\text{tp,out}} = i_{\text{tp,in}} + \frac{\dot{q}_{eff}}{\dot{m}_v + \dot{m}_l} \ , \tag{3.3}$$

and the outlet vapor quality is given by

$$x_{out} = \frac{i_{\text{tp,out}} - i_{l,sat,out}}{i_{v,sat,out} - i_{l,sat,out}} \ , \tag{3.4}$$

where the enthalpies $i_{v,sat,out}$ and $i_{l,sat,out}$ are the enthalpies of saturated vapor and liquid, respectively, evaluated at the pressure measured at the outlet of the test section.

The experimentally measured local heat transfer coefficient, h, is given by

$$h = \frac{\dot{q}''_{eff}}{T_w - T_{sat}} \ , \tag{3.5}$$

where T_w is calculated using Equation 3.13.

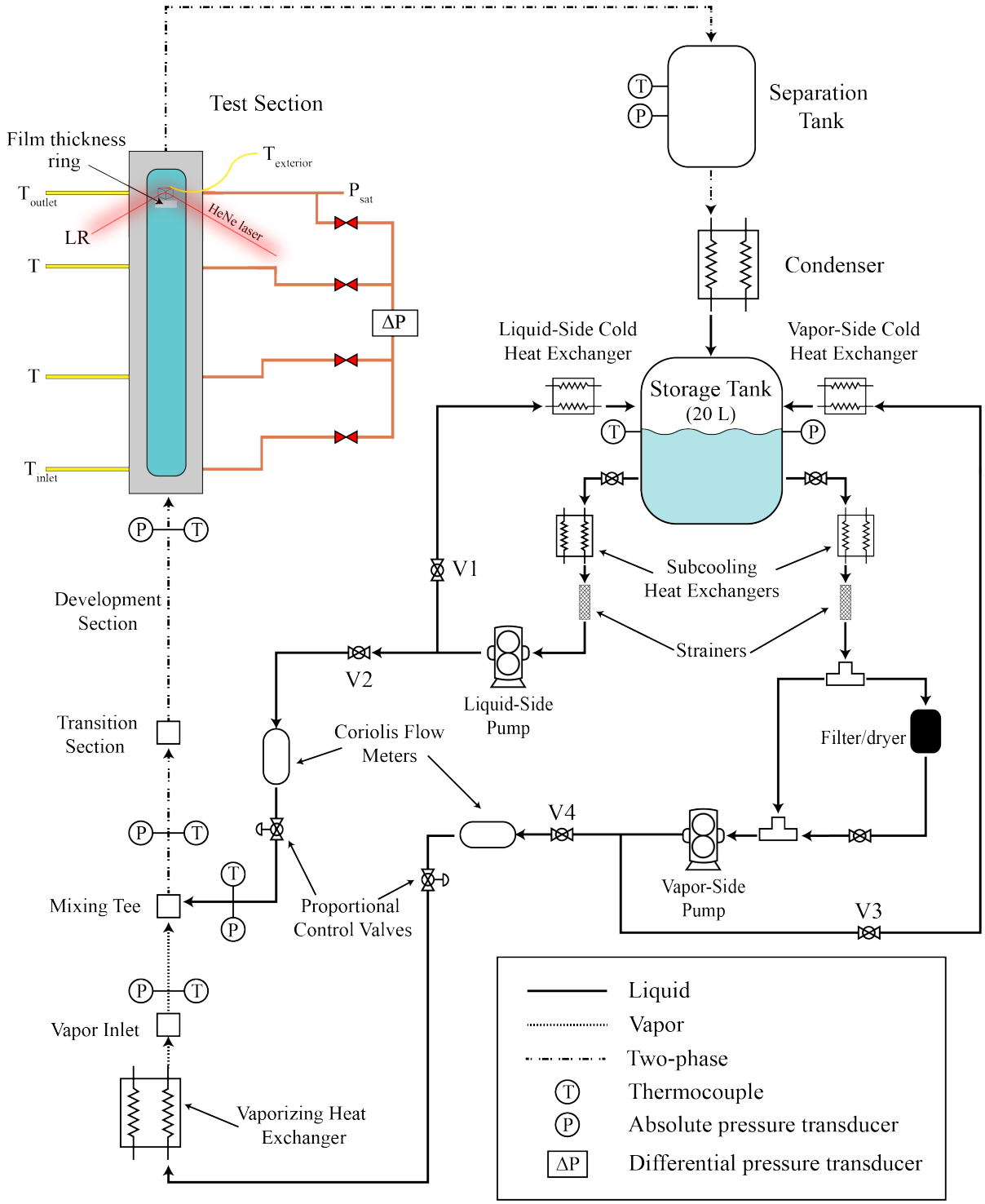

Figure 3.1: Schematic of the MFVAL two-phase flow loop

3.2 Validation

The goal for the current work is to investigate the flow characteristics that lead to CHF conditions, and also to characterize the behavior of the liquid film during intermittent dryout. A combination of time averaged process data and highly time-resolved data is employed to facilitate this investigation.The experimental apparatus and procedure, are validated by comparing single-phase vapor R245fa data to predictions obtained from correlations in the literature.

3.2.1 Pressure drop

A comparison between experimental and predicted frictional pressure drop is performed for varying vapor mass flow rates in order to verify that the test section used in this study behaves in a manner similar to a conventional smooth channel and check the instrumentation. Under single-phase conditions, the pressure difference measured along the test section is a combination of pressure loss due to friction, the hydrostatic pressure change due to gravity, and the pressure difference associated with changes in momentum. The latter contribution is negligible. As a result, the gravitational pressure drop is subtracted from the total measured pressure difference to obtain the experimental pressure loss due to friction. It was verified that the flow is fully developed by comparing pressure drop measurements along the development section to measurements made along the test section. Therefore, the pressure gradient is assumed to be constant along the test section. From the pressure gradient and the absolute pressure measured at the outlet of the test section, the pressure at any point within the test section can be inferred and is used to calculate local fluid properties. All fluid properties of R245fa were calculated using Klein (2019).

The experimental friction factor is calculated from the measured frictional pressure drop

between two ports along the test section. It is given by

$$f_{exp} = \frac{\Delta P_{exp}}{L} \frac{2D_h}{\rho_v u^2} \ , \tag{3.6}$$

where ΔP_{exp} is the measured frictional pressure drop, D_h is the hydraulic diameter, ρ_v is the density of vapor R245fa, and L is the distance between the high pressure and low pressure ports. The mean velocity, u, of the flow is

$$u = \frac{\dot{m}_v}{\rho_v A_c} \ , \tag{3.7}$$

where $\dot{m}_v$ is the measured mass flow rate of the vapor refrigerant, and A_c is the cross sectional area of the test section. The Reynolds number of the single-phase vapor is calculated by

$$\mathrm{Re} = \frac{\rho_v u D_h}{\mu_v} \ , \tag{3.8}$$

where μ_v is the viscosity of the vapor.

3.2.2 Calculation of effective heat input

An energy balance in single-phase vapor R245fa is used to characterize heat losses from the test section, which is necessary to calculate the effective heat input into the refrigerant. Heat is generated at the inner wall of the channel by applying electrical power, $\dot{q}_{applied}$, across the FTO coating on the inner wall of the test section. The applied power is calculated with Ohm's law using real-time measurements of the voltage and current in the circuit (accounting for voltage drop across connectors). Only a portion of the applied power is transferred to the refrigerant and the rest is lost to the surroundings. The heat input to the refrigerant is measured using an energy balance on the fluid in single-phase conditions. Pressure and temperature of the superheated vapor are measured at the inlet and outlet of the test section to determine the local specific enthalpies. The measured energy transferred

to the fluid, $\dot{q}_{measured}$, is given by

$$\dot{q}_{measured} = \dot{m}(i_{v,sh,out} - i_{v,sh,in}) \ , \tag{3.9}$$

where $i_{v,sh,in}$ and $i_{v,sh,out}$ are the specific enthalpies of superheated vapor at the inlet and outlet respectively. The heating power lost to the surroundings is calculated as the difference between the applied heating power and the measured change in fluid enthalpy,

$$\dot{q}_{loss} = \dot{q}_{applied} - \dot{q}_{measured}. \tag{3.10}$$

Heat in the test section is lost by conduction through the window and natural convection to the surroundings, and by conduction through the Ultem sidewalls and then natural convection to the surroundings. A thermal network analysis is used to identify the thermal resistances associated with these two pathways, illustrated in Figure 3.2. These resistances can later be used to calculate heat loss in two-phase flow conditions where the local enthalpy measurements are not possible.

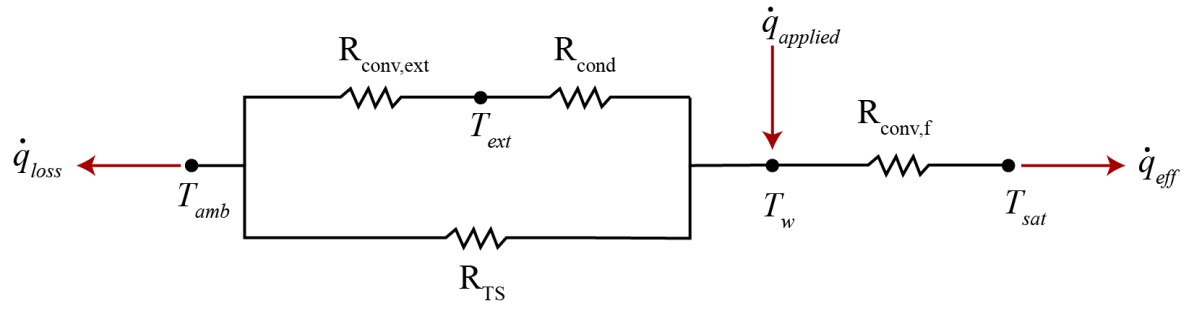

Figure 3.2: Schematic illustrating the thermal resistance network associated with the test section heating apparatus.

The heat loss is given by

$$\dot{q}_{loss} = \frac{T_{ext} - T_{amb}}{R_{\text{conv,ext}}} + \frac{T_w - T_{amb}}{R_{\text{TS}}} \ , \tag{3.11}$$

with

$$R_{\text{conv,ext}} = \frac{1}{\overline{h}_{ext} A_{TS}} \ , \tag{3.12}$$

where T_{ext} is the temperature of the outer wall in contact with the surroundings, $\overline{h}_{ext}$ is the heat transfer coefficient associated with natural convection on the exterior of the test section, and R_{TS} is the combined thermal resistance associated with conduction through the Ultem and natural convection to the surroundings. Values of $\overline{h}_{ext}$ = 10 W/m^2-K and R_{TS} = 0.95 K/W were obtained through regression of the data. The effect of temperature on both $\overline{h}_{ext}$ and R_{TS} was found to be negligible. The inner wall temperature, T_w, is calculated by setting the steady-state conduction through the window equal to the energy released by natural convection so that

$$T_w = \left(\frac{T_{ext} - T_{amb}}{R_{\text{conv,ext}}} \right) R_{\text{cond}} + T_{ext} \ , \tag{3.13}$$

and

$$R_{\text{cond}} = \frac{th_g}{k_g A_{TS}} \ , \tag{3.14}$$

where k_g = 1.2 W/m-K is the thermal conductivity of glass, and th_g = 3.0 mm is the thickness of the glass wall. The effective heat input, $\dot{q}_{eff}$, is obtained from

$$\dot{q}_{eff} = \dot{q}_{applied} - \dot{q}_{loss} = I \Delta V - \dot{q}_{loss} \ , \tag{3.15}$$

where I is electrical current, ΔV is the voltage potential across the FTO coating, and $\dot{q}_{loss}$ is obtained from Equation 3.11. The effective heating power divided by the surface area of the heated section gives the effective heat flux, $\dot{q}''_{eff}$, received by the fluid at the wall-fluid interface.The local heat transfer coefficient for vapor R245fa at the inner surface of the channel is calculated by

$$h_v = \frac{\dot{q}''_{eff}}{T_w - T_\infty} \ , \tag{3.16}$$

where T_∞ is the mean bulk fluid temperature measured from the test section outlet thermo-

couple. The experimental Nusselt number for single-phase vapor R245fa is calculated from the single-phase heat transfer coefficient:

$$\mathrm{Nu} = \frac{h_v D_h}{k_v} \,, \tag{3.17}$$

where k_v is the thermal conductivity of vapor R245fa.

3.3 Validation of experimental facility and procedure

The experimental friction factor is shown in Figure 3.3 as a function of the vapor Reynolds number. The friction factor behaves as expected and agrees with the correlations for flow inside of a smooth channel by Blasius (1913), Colebrook (1939), and Petukhov (1970). The external flow correlation of Blasius (1913) tends to slightly underestimate the experimental friction factor, which is to be expected. The internal flow correlations of both Colebrook (1939) and Petukhov (1970) provide accurate estimates of the measured values. The fact that the experimental data agrees with well-established correlations provides confidence that the experimental test section behaves as a conventional flow channel and that mass flow rate, temperature, pressure, and pressure drop are all accurately measured within the facility.

The accuracy of heat flux measurements is validated by comparing with predictions from two well-established correlations from the literature by Gnielinski (1975) and by Dittus and Boelter (1930), shown in Figure 3.4. The experimental Nusselt number is shown as a function of the single-phase Reynolds number defined by Equation 3.8. Agreement between the experimental data and both correlations provide confidence in our ability to accurately predict the heat input to the fluid within the test section as well as the performance of the instrumentation required by these tests.

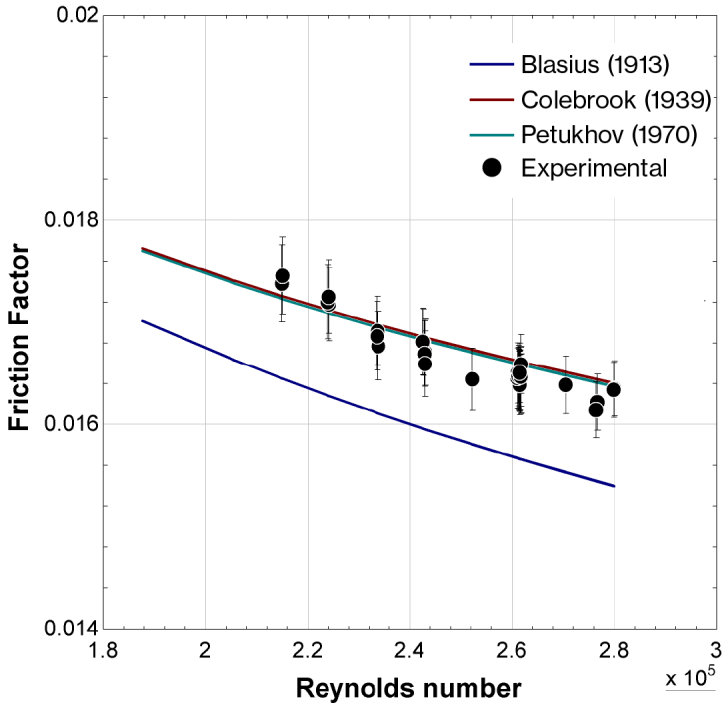

Figure 3.3: Friction factor for single-phase vapor refrigerant as a function of Reynolds number

3.3.1 Uncertainty of measurements

Temperature measurements were calibrated and their uncertainties were evaluated according to the procedure suggested by Abernethy and Thompson (1973). The manufacturer's uncertainties of the pressure transducers, power supplies, and mass flow meters were adopted. For a given calculated parameter, the uncertainty was estimated accounting for the error of the instruments and measurement procedures using the method of sequential perturbation as proposed by Taylor and Kuyatt (1994). The experimental uncertainties associated with the sensors, estimation procedures, and calculated parameters are given in Table 5.1. It is worth highlighting that there are different values of uncertainty for the absolute value of vapor quality, x, and changes in vapor quality δx. The uncertainty of the effective heat flux ($\dot{q}''_{eff}$) has contributions from the uncertainty associated with the power supply and the uncertainty associated with heat losses. The uncertainty for the power supply is provided by the manufacturer. The uncertainty in heat losses is primarily due to the uncertainty in

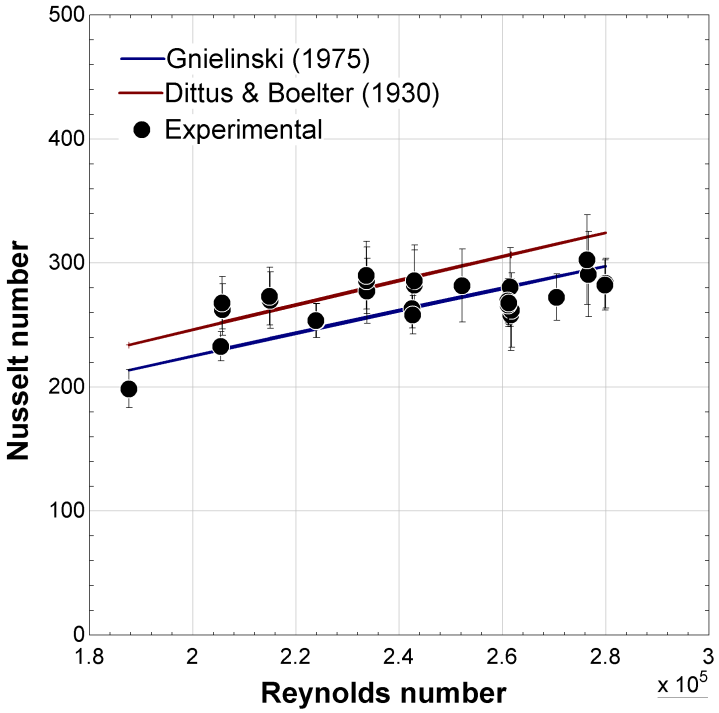

Figure 3.4: Nusselt number for heat transfer to the single-phase vapor refrigerant as a function of Reynolds number

the regressed variables. However, under two-phase flow conditions, approximately 99% of the supplied heat is transferred to the refrigerant. The uncertainty in $\dot{q}''_{eff}$ in Table 5.1 is listed for two-phase flow conditions and therefore is very small. The uncertainty in CHF is taken to be the uncertainty in $\dot{q}''_{eff}$.

Parameter	**Symbol**	**Uncertainty**
Absolute pressure	P	300 Pa
Differential pressure	ΔP	7 Pa
Mass flux	G	0.7%
Temperature	T	0.05 °C
Supplied heating power	$\dot{q}_{applied}$	6 W
Heat losses	$\dot{q}_{losses}$	10%
Effective heat flux	$\dot{q}''_{eff}$	0.5%
Heat transfer coefficient	h	1.5%
Local vapor quality	x	0.003
Change in vapor quality	δx	0.0005
Critical heat flux	CHF	0.5%

Table 3.1: Uncertainties of process measurements

3.3.2 Time-resolved measurements

Methodology for detection of dryout

The loss of liquid film at the wall is detected in several ways. The first and most obvious method is the use of images from high-speed videos. Image analysis allows for visualization of the dryout and rewetting process with good time resolution. However, recording high-speed videos is challenging because the duration is limited by the camera memory. Thus, it is difficult to resolve dryout events occurring in a fraction of a second and dryout periods lasting several minutes. In addition, many events must be recorded to obtain meaningful statistics.

A laser reflectance technique is therefore preferred for indication of a dryout event. Although it gives only local information about the state of the wall (wet or dry), it can record data at high speed over very long periods of time (the data sets used in this study range between 15 and 20 minutes). The laser reflectance is derived from an optical technique used to measure temperature within our facility Fehring et al. (2020). A laser beam is directed to the glass wall of the test section. At the glass/fluid interface, a portion of the beam is reflected and the rest is transmitted into the refrigerant. After passing through a prism and a mirror, the intensity of the reflected beam is measured by a photodiode (Thorlabs PDA55). The ratio of the intensity of the reflected beam to the intensity of the incident laser beam is referred to here as the intensity ratio.

The difference in the index of refraction between liquid and vapor R245fa is such that, with the appropriate incidence angle, most of an incident laser beam is transmitted into the liquid film whereas most of the light is reflected when vapor is in contact with the window. This leads to a large change in intensity ratio when the wall transitions from wet to dry, as seen in Figure 3.5, during intermittent dryout events.

The laser reflectance measurement location is 1 cm upstream from the exterior thermocouple and 2 cm downstream from the location where film thickness and high-speed video are taken. With this instantaneous indication of wet or dry conditions, a temporally averaged

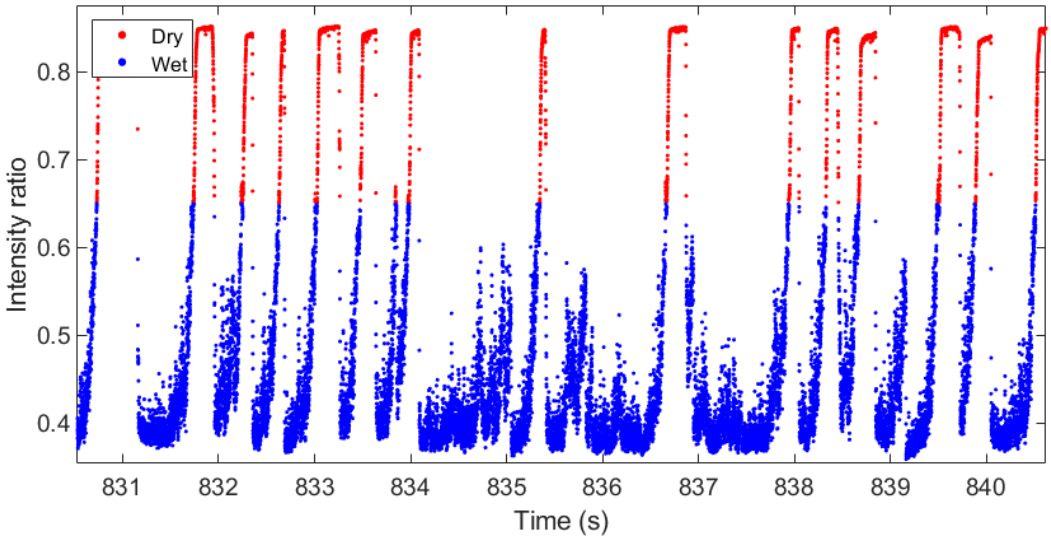

Figure 3.5: Time trace of the intensity ratio signal during dryout events.

dry time fraction f_{dry} can be calculated,

$$f_{dry} = \frac{\text{Cumulative dry time}}{\text{Total time}}. \tag{3.18}$$

The extent of individual dryout events and time between dryout events is also easily recorded using the intensity ratio signal. The uncertainty of f_{dry} is taken as the time it takes for the signal to change from fully wet to fully dry, multiplied by the number of dryout events and divided by the total time. The uncertainty was found to be on average 0.4%.

High-speed video and liquid-film thickness

High-speed video of the liquid film is captured through the transparent test section using a Phantom V311 high-speed camera. The images are acquired at a frame rate of 4000 Hz. In addition, liquid-film thickness is measured during cycles of intermittent dryout-rewet using a non-invasive optical technique Hurlburt and Newell (1996); Shedd and Newell (1998); Moreira et al. (2020). The film thickness data are also acquired at a rate of 4000 Hz. The uncertainty in the liquid-film thickness measurement is taken as 8.6 μm, which was shown through previous work in this facility to be the maximum uncertainty in the film thickness

measurements Moreira et al. (2020). It has been verified that changes in the refractive index of the fluid due to temperature variations when the test section is heated induce an error that is much less than the uncertainty.

3.4 Experimental procedure

Figure 5.3 shows an example of time traces of the signals used to identify dryout characteristics of the flow within the test section. The black line represents the effective heat flux applied to the window, $\dot{q}''_{eff}$, the red line represents the exterior wall temperature, T_{ext}, and the blue line represents the local saturation temperature, T_{sat}. The orange data represents the intensity ratio from the laser reflectance measurement. Finally, the vertical black dotted lines indicate when the camera trigger is activated and liquid-film thickness is measured. The camera takes approximately 5 minutes to save each data set. When the camera has finished saving one recording and as soon as the flow has reached a new quasi-steady equilibrium, the camera is triggered again to catch the liquid-film thickness of the new flow condition. This process is repeated throughout the data collection.

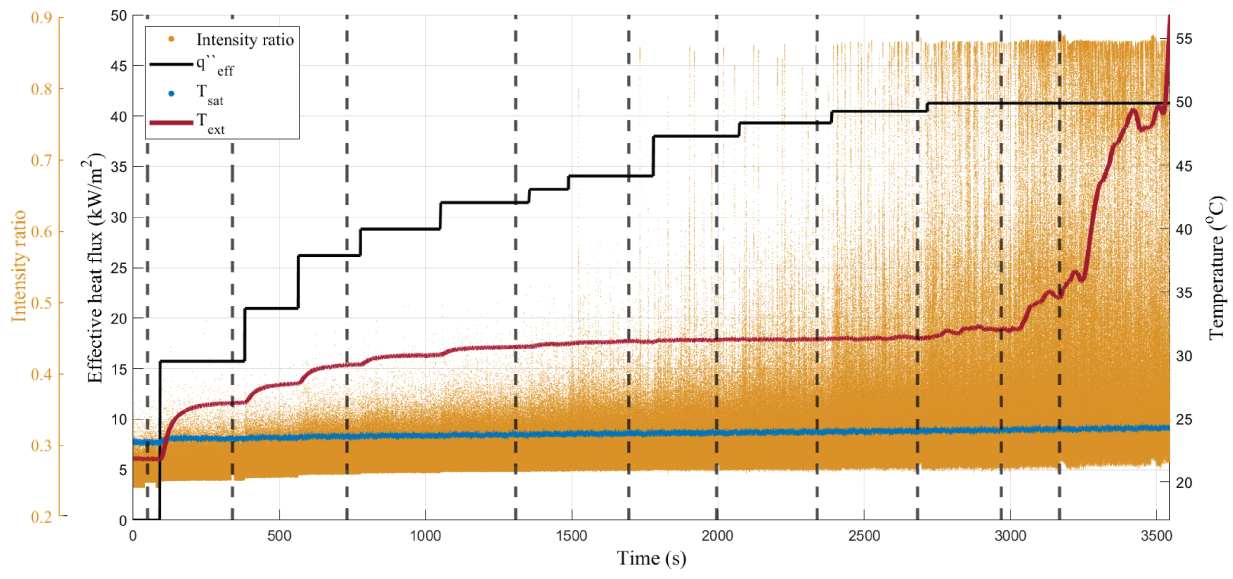

Figure 3.6: Example of MFVAL data time trace for flow conditions of $G = 150$ kg/m^2-s, $x_{in} = 0.742$.

The data recording begins with the heating power off. At this point, the test section temperature is near ambient temperature and there is negligible heat transferred between the test section and the surroundings. The liquid-film thickness measurement is taken during unheated conditions and serves as a good representation of the behavior at the test section inlet. After this initial liquid-film thickness measurement, the heaters are turned on; this can be seen as the first step increase in heat flux in Figure 5.3. The test section exterior temperature, which serves as a proxy for the inner wall temperature during testing, is allowed to reach a new equilibrium temperature for at least 60 seconds prior to increasing the heating power again. The measured instantaneous deviations in temperature, pressure and pressure drop are within the uncertainty of the measurements. The camera takes approximately 5 minutes to save each data set. When the camera has finished saving one recording and the flow has reached a new equilibrium, the camera is triggered again to catch the liquid-film thickness of the new flow condition. This process is repeated throughout the data collection until runaway temperature conditions are observed in the test section due to a significant reduction in HTC corresponding to the CBT. The experiment is then concluded.

Chapter 4

Dryout under steady flow

4.1 Results

The experimental results for time-averaged local HTC data are presented first. Later in this section, liquid-film behavior is analyzed using time-resolved measurements of the liquid-film thickness and high-speed data. The mass flux investigated was within the range of $G = 110$ - 170 kg/m^2-s, and the range of vapor quality considered was from 0.7 to 1. The pressure within the test section was held constant at 150 kPa. The effective heat flux was varied between 0 - 50 kW/m^2.

4.1.1 Heat transfer coefficient

Figure 5.7 shows time-averaged data for the local HTC as a function of local vapor quality in black, and the time-averaged temporal dry fraction, f_{dry}, as a function of vapor quality in red. For $x < 0.845$, no dryout events are detected, and therefore $f_{dry} = 0$. These data points are unseen on the plot because of the logarithmic axis for f_{dry}. It is only once dryout events are detected that the data for f_{dry} appears on the plot. The initial increase in f_{dry} from 0 to 10^{-2} coincides with an increase in the local HTC. For these flow conditions (and all others as seen in the next section), the local HTC increases when dryout events first occur and reaches a maximum under conditions that result in $f_{dry} \approx 0.05$.

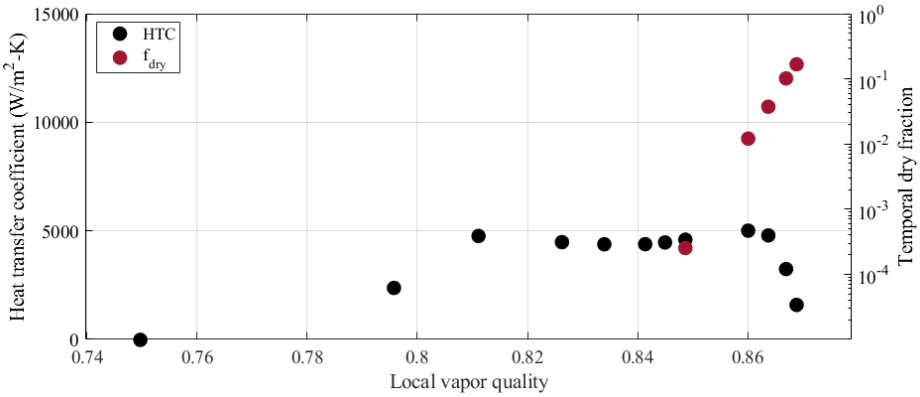

Figure 4.1: Local HTC and f_{dry} as a function of local vapor quality taken under conditions corresponding to Figure 5.3.

4.1.2 Behavior of HTC for varying dry time

This section characterizes how the local time-averaged HTC, h, behaves for varying f_{dry}. The maximum measured HTC prior to the occurrence of dryout events, h_{tp}, and the single-phase vapor HTC, h_v, both increase with increasing mass flux. In an effort to compare data for varying mass flux, a time-averaged and normalized HTC, $\mathcal{H}$, is defined as,

$$\mathcal{H} \triangleq \frac{h - h_v}{h_{tp} - h_v} \ , \tag{4.1}$$

where h is the measured time-averaged HTC. The single-phase Dittus-Boelter correlation is used to provide accurate estimates for h_vDittus and Boelter (1930). In addition, a weighted and normalized HTC, $\mathcal{H}_{weighted}$, based on simply weighting h_v by the dry time and h_{tp} by the wet time is calculated as,

$$\mathcal{H}_{weighted} = 1 - f_{dry} \ . \tag{4.2}$$

If the local HTC could be modeled as a simple time-weighted average of the two-phase HTC, h_{tp}, and the dry HTC, h_v, it would follow $\mathcal{H}_{weighted}$. For this reason, $\mathcal{H}_{weighted}$ is used as a reference from which to compare the experimentally measured behavior.

In Figure 4.2, experimentally measured $\mathcal{H}$ and $\mathcal{H}_{weighted}$ are shown as a function of the time-averaged dry fraction. The black data points are steady-state data, and the colored

data are taken under conditions in which the vapor flow is pulsedMorse et al. (tion). For the conditions at which dryout events are first observed ($f_{dry} < 10^{-3}$), there is no obvious change in the value of $\mathcal{H}$. Between $10^{-3} < f_{dry} < 0.05$, there is an increase in the value of $\mathcal{H}$ with increasing f_{dry}. At $f_{dry} \approx 0.05$, the value of $\mathcal{H}$ has increased by approximately 10-25% compared to its initial value prior to any dryout events. The local maximum in $\mathcal{H}$ at $f_{dry} \approx 0.05$, corresponding to the OBC. For $f_{dry} > 10^{-1}$, there is a significant decrease in $\mathcal{H}$ for increasing values of f_{dry} associated with CBT. Further increasing f_{dry} results in the value of $\mathcal{H}$ approaching zero as the HTC approaches the value for single-phase vapor.

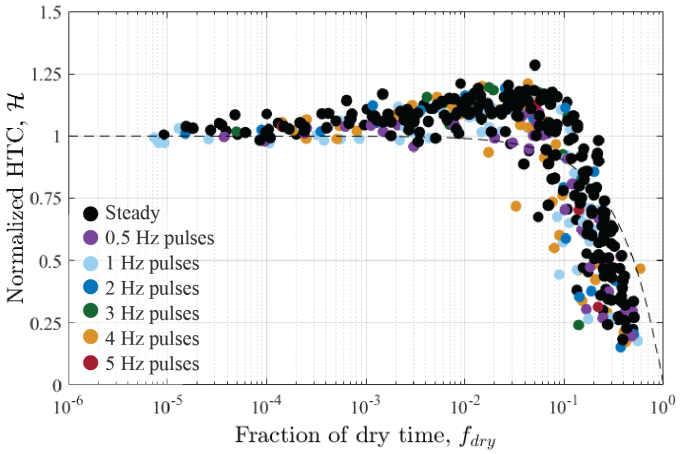

Figure 4.2: Normalized heat transfer coefficient as a function of fraction of dry time.

A mechanistic approach to modeling the local HTC using liquid-film thickness and other local flow quantities is presented in later d of this work. The mechanistic model is capable of providing accurate estimates of two-phase heat transfer coefficient for annular flow conditions up to and including OBC. The model accurately predicts the measured behavior of $\mathcal{H}$ with respect to f_{dry} as shown in Figure 4.2. The increase in local HTC under flow conditions with small f_{dry} is related to the reduction in effective conduction length (and hence reduction in the thermal resistance) as the base film is vaporized between disturbance waves.

4.1.3 Liquid film behavior in the intermittent dryout flow regime

Film thickness has long been known to be an extremely important characteristic of flows within the annular flow regime. Film thickness measurements made in boiling systems will allow for better understanding of the film behavior, which will allow the development of more robust models of the liquid film, and, in turn, better heat transfer predictions. In this work, further insight into dryout and rewet mechanisms is gained by taking time-resolved measurements of the liquid-film thickness during dryout. The subfigures in Figure 4.3 are snapshots of film thickness data plotted with the intensity ratio.

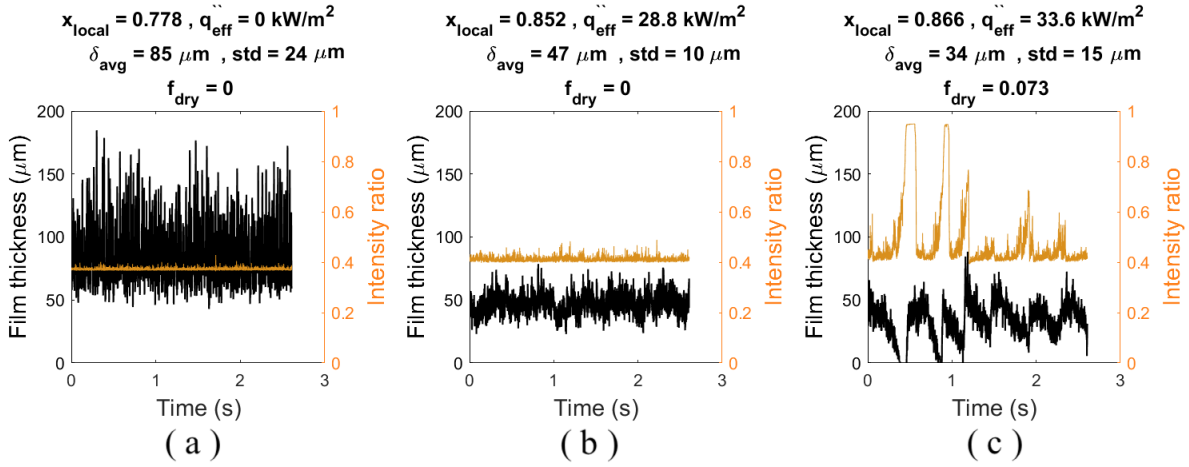

Figure 4.3: Liquid-film thickness and intensity ratio of laser reflectance overlay at flow conditions varying from unheated to dryout for $G = 167$ kg/m^{2}s and $x_{in} = 0.778$.

Figure 4.3a displays the film thickness for the inlet (or unheated) conditions. The large variance in film thickness is related to the passage of disturbance waves at a relatively high frequency ($\approx$ 15 Hz). Figures 4.3b and 4.3c display measurements for heated conditions. It can be seen in Figure 4.3b that under heated conditions, the mean liquid-film thickness and the wave height have decreased. The passage of waves can still be seen as spikes in the film thickness signal. The magnitude and frequency of the waves are significantly reduced. Cyclic dryout between disturbance waves, such as those shown in Figure 4.3c, is observed to occur prior to thermal runaway conditions (CBT). The disturbance wave frequency decreases as the flow transitions between the annular to intermittent dryout flow regimes, as seen in

Figure 4.3c.

4.1.4 Visualizing dryout

Liquid-film thickness data have shown the importance of disturbance waves in the cyclic dryout-rewetting process. Analysis of high-speed video allows for direct observation of the dryout and rewet mechanisms. Figure 4.4 shows a sequence of images capturing the dryout of the base film and subsequent rewetting by a disturbance wave. The first image shows a liquid film that is relatively thick, associated with a disturbance wave (t = 0 ms). The base film in the wake of the disturbance wave is thin and nearly stagnant; mass is removed from this region via vaporization (t = 100 ms). Once enough mass is vaporized, the base film is no longer thick enough to maintain a stable film. A dryout event occurs when the base film ruptures, and the red-shaded area on Figure 4.4 indicates a dry region on the heated surface (t = 200 ms). The heated surface is rewetted when a disturbance wave passes the local position (t = 300). The dryout mechanism (vaporization of the base film) and the rewetting mechanism (passage of a disturbance wave) occur on time scales that differ by approximately one order of magnitude.

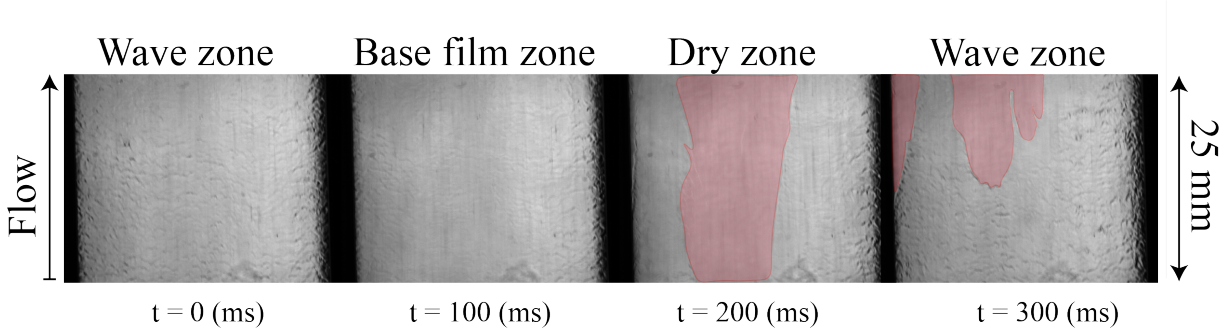

Figure 4.4: Annotated sequence of images capturing dryout and rewet with flow conditions: $G = 167.5$ kg/m^2-s, $\dot{q}''_{eff} = 30.6$ kW/m^2, $X_{local} = 0.837$, $f_{dry} = 0.023$

For this study, the authors identified the flow conditions at which nucleate boiling did occur and intentionally avoided these flow conditions. The suppression of nucleate boiling was confirmed by direction observation using high-speed video of the flow field during dryout,

such as that shown in Figure 10.

Chapter 5

Dryout under forced oscillations

Abstract

The dryout of liquid film and the role of disturbance wave frequency is investigated. The Multiphase Flow Visualization and Analysis Laboratory (MFVAL) at UW-Madison has built a facility capable of providing vapor pulses (or density-wave oscillations) with consistent flow rate for long periods of time. Experimental results for heat transfer coefficient (HTC), liquid-film thickness, temporal dry fraction, and dryout statistics under pulsatile conditions are presented. A normalized time-averaged HTC is compared with the fraction of time that the surface is dry. The maximum in HTC associated with local optimal boiling conditions (OBC) occurs when the surface is dry 5% of the time, independent of pulse amplitude and frequency. Liquid-film measurements, dryout statistics, and direct observation indicate that disturbance-wave frequency can be manipulated by density-wave oscillations in the flow field.

5.1 Introduction

The most common instability in commercial boiling water reactors are density-wave oscillations, or flow-channel oscillations March-Leuba (1992). Density waves are instabilities due to oscillations in fluid vapor density due to oscillations in pressure gradient that prop-

agate downstream the channel Yadigaroglu and Bergles (1972). The role of instabilities concerning the boiling crisis is not well understood. The purpose of this current work is to experimentally investigate the impact of density-wave oscillations on the liquid film in annular two-phase flow.

5.1.1 Flow oscillations

For boiling water reactors, the density-wave oscillations are recorded over a distribution of frequencies March-Leuba (1992). Under nominal flow conditions, the highest amplitude density-wave oscillations occur at a frequency on the order of 1 HzMarch-Leuba (1992). Ozawa et al. (1993) performed experimental work on oscillating flows and investigated the nucleate boiling regime. In their experiment, the flow was oscillated using an oscillating piston on subcooled liquid prior to a heated section. Ozawa et al. (1993) reported a reduction in the heat flux needed to reach CBT for increasing pulse amplitude and increasing pulse period. Cherdantsev et al. (2021) investigated how high-frequency oscillations affect disturbance waves in downward annular flow using an air-water loop. In the experiments, flow oscillations were generated by pulsating the liquid-mass flow into the system. Cherdantsev et al. (2021) observed a 'natural frequency', and for frequencies around the natural frequency, it was possible to excite and amplify the disturbance waves using their liquid-flow oscillating apparatus. For oscillation frequencies much higher than the natural frequency, there was no observable impact on the disturbance waves. For the highest frequencies investigated, the disturbance waves resemble those of steady flow conditions. 3

5.1.2 Contribution of current work

The goal of the current work is to investigate how flow oscillations, specifically density waves, influence flow behavior near the CBT. This work investigates how density-wave oscillations (in the form of vapor pulses) change the flow characteristics, namely disturbance waves, heat transfer, and dryout for conditions within the intermittent dryout flow regime.

Experimental measurements are made under oscillating-flow conditions within the annular and intermittent dryout flow regimes. A mechanistic approach to modeling dryout provides an explanation for the trends observed by previous authors related to pulse frequency and dryout.

5.2 Experimental

5.2.1 Flow loop

In this experiment, heat transfer and liquid-film characteristics are measured during flow boiling using R-245fa (1,1,1,3,3-pentafluoropropane, Honeywell) as the working fluid. Superheated vapor and subcooled liquid are mixed to form a two-phase mixture. The two-phase mixture is of relatively high vapor quality ($x > 0.70$) and mass flux ($G > 100$ kg/m^2-s) and therefore in the annular flow regimeOng and Thome (2011a). The two-phase mixture flows through the test section where it is subjected to a constant heat flux through the electrically heated walls. A simple thermal resistance model is employed to account for energy losses, allowing for accurate prediction of the amount of energy transferred to the two-phase fluid and enabling calculations of outlet enthalpy and vapor quality, as well as heat transfer coefficient. The steady-state portion of the facility has been outlined in great detail in a previous manuscriptMorse et al. (2021).

5.2.2 Vapor pulse generator

An additional flow circuit provides vapor pulse injections to the steady-state vapor stream at a desired frequency. Figure 5.1 displays a full schematic of the annular flow facility. The pre-existing steady-state loop and the transient circuit are represented in the schematic by black and red lines, respectively. The transient vapor mass is generated within a heated storage tank, referred to as the 'pulse generator' and labeled as such in Figure 5.1. The pulse generator is a 62-liter tank fitted with 6 cartridge heaters in order to provide heat

to the refrigerant and increase the saturation pressure within the tankFehring et al. (2020). The liquid-fill ratio of the tank is monitored closely and maintained between 20-35% during data collection in order to provide consistent vapor pulses.

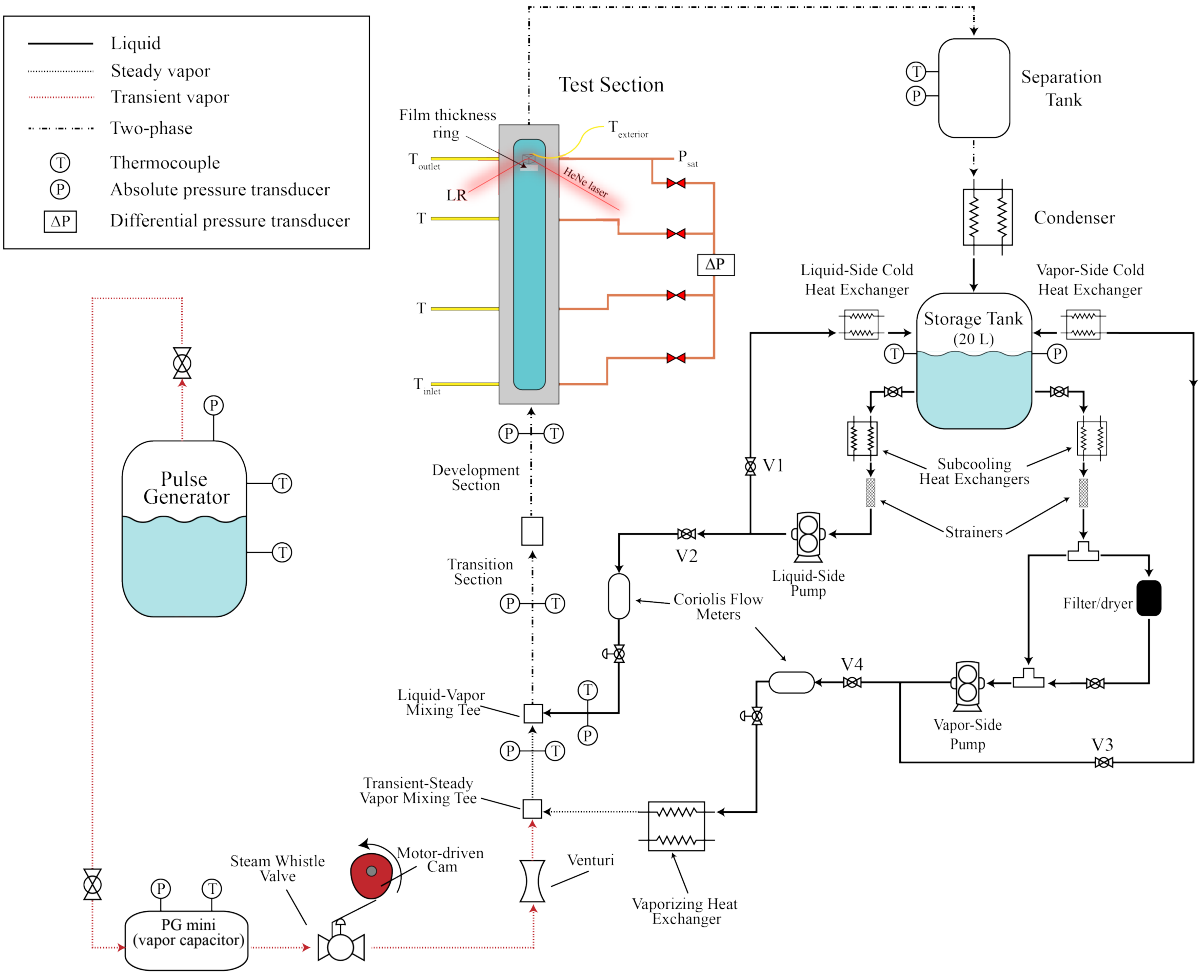

Figure 5.1: Schematic of MFVAL experimental two-phase flow loop including transient circuit.

The pressure difference between the pulse generator tank and the vapor mixing tee drives the motion of the vapor refrigerant through the transient circuit. The pressure difference between the main pulse generator tank and the test section is controlled in order to send pulses of a specified amplitude. From the pulse generator, refrigerant is vaporized and allowed to escape through the top of the tank. The vapor refrigerant leaves the pulse generator and travels through a section of 3/8 inch copper pipe towards a small storage tank which

serves as a vapor-mass capacitor, labeled as 'PG mini' in Figure 5.1. This segment of the loop is heated using a self-regulated heating wire and insulated in order to prevent any condensation prior to injection. Vapor is allowed to escape into the main flow loop by opening a steam-whistle valve (Kingston, Model 425-5). The valve is actuated by a cam mounted on the shaft of an electric stepper motor (Anaheim Automation, 34Y-108D-LW8). The stepper motor continuously rotates at a specified frequency for the entirety of each data set. The settings, such as frequency, duration, and ramp time, are adjusted using a LabView programChan (2020). When the valve is opened, vapor flows downstream through a custom Venturi flow meter (Primary Flow Signal, HBX-1). The differential pressure across the Venturi is measured with a differential pressure transducer (Omega, PX409-10WDDU5V).

5.2.3 Vapor pulse mass-flow measurement

Figure 5.2 shows time traces of the differential pressure signal measured across the Venturi for two different pulse frequencies. Pulse frequencies of 1 Hz and 5 Hz are shown in Figures 5.2a and 5.2b, respectively. The time traces show that for each case, vapor pulses of consistent amplitude and shape are generated continuously. In Figures 5.2a and 5.2b, the power spectrum density (PSD) is plotted for the Venturi differential pressure and test section absolute pressure signals. The PSD of the signal from the Venturi indicates that the system is providing pulses at the desired frequency. The PSD of the test section's absolute pressure signal indicates that the vapor pulses persist downstream and travel through the test section without being significantly changed. It is worth noting that what appears to be the system natural frequency ($\approx$ 2.5 Hz) can be seen in the absolute pressure PSD plots in Figures 5.2a and 5.2b.

The transient vapor exits the Venturi and immediately enters into a custom-designed mixing annulus which smoothly combines the steady and transient streams into a single stream of superheated vaporRodarte (2015). The combined superheated vapor exits the mixing tee and travels downstream to the liquid-vapor mixing tee, where subcooled liquid and super-

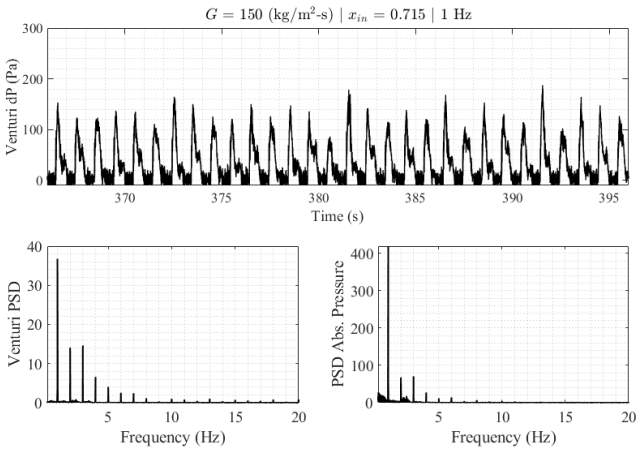

(a) Time trace of differential pressure signal across Venturi (top), and PSD plots of the Venturi differential pressure and the test section absolute pressure signals (bottom); for 1 Hz pulses.

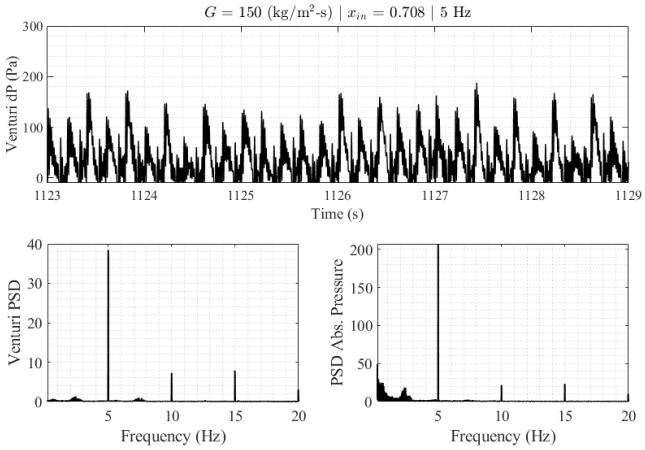

(b) Time trace of differential pressure signal across Venturi (top), and PSD plots of the Venturi differential pressure and the test section absolute pressure signals (bottom); for 5 Hz pulses.

Figure 5.2: Example of Venturi differential pressure signal used for calculating vapor pulse mass flow rate.

heated vapor are combined to form a saturated mixture. The enthalpy and vapor quality of the single-phase flow streams are known prior to mixing. Therefore an energy balance is used to obtain the enthalpy of the mixture, which allows for calculation of the vapor quality. After the mixing tee, the flow enters a component designed to provide a smooth transition from a 1-inch diameter circular cross-section, to a 36 mm x 12 mm rectangular cross-section ($D_{\mathrm{h}} = 18$ mm). After the transition section, the mixture flows through an insulated channel with length of 150 times that of the hydraulic diameter to become fully developed Zhao et al. (2013). The fully-developed two-phase mixture then proceeds downstream to the test

section.

5.2.4 Test section

The transparent test section allows for optical access and a unique opportunity to observe flow boiling phenomena through a heated surface. Liquid-film thickness, a temporal dry fraction, and dryout statistics are measured using non-invasive optical techniques Fehring et al. (2020); Moreira et al. (2020); Morse et al. (2021).

A laser reflectance technique is utilized for instantaneous indication of a dryout event. The laser reflectance is derived from an optical technique used to measure temperature within our facilityFehring et al. (2020). The optical technique takes advantage of the significant difference in refractive index between the liquid and vapor phases. The output is a binary time-resolved signal which indicates the phase of fluid that is in contact with the heated surface. With the instantaneous indication of phase at a heated surface, a time-averaged temporal dry fraction, f_{dry}.The value of f_{dry} is a measure of the time-average fraction that the surface spends dry under prescribed flow conditions. The measurement technique, interpretation of the signal, and method for estimating uncertainty using this technique are discussed in great detail between Morse et al. (2021) and Morse et al. (2024).

5.2.5 Data regression

Validation of experimental apparatus and procedures

The experimental flow channel and heating procedures used in this work have been validated through previous experiments performed using single-phase vapor refrigerant (Morse et al. (2021)). The experimentally measured pressure drop due to friction in the test section flow channel can be predicted with high accuracy using classical correlations from Colebrook (1939) and Petukhov (1970). The agreement between experimental data and predictions made by well-established correlations instills confidence that the test section flow channel behaves the same as a conventional smooth channel and also that the measurement techniques are accurate.

The time-averaged effective heat input can be calculated by subtracting heat losses from the total power supplied. Heat losses to the surroundings are taken into account using a thermal resistance networkMorse et al. (2021). The accuracy of the thermal resistance network is validated by comparing measured and predicted Nusselt numbers in single-phase vapor flows. Predictions from two well-established correlations in the literature, Gnielinski (1975) and Dittus and Boelter (1930), are in good agreement with the experimental data. This validation provides confidence in the methodology for predicting heat losses in the test section.

Process conditions

The two-phase data regression under pulsed flow conditions includes an energy balance to account for the mixing of transient and steady vapor. The transient stream, $\dot{m}_{v,\text{pulse}}$, mixes with the steady stream, $\dot{m}_{v,\text{steady}}$ in a well-insulated mixing component. The total

time-averaged vapor mass, $\dot{m}_v$, is calculated as the sum of the transient and steady streams,

$$\dot{m}_v = \dot{m}_{v,\text{steady}} + \dot{m}_{v,\text{pulse}} \ . \tag{5.1}$$

The time-averaged enthalpy of the steady vapor stream, $i_{v,\text{steady}}$, is known by measuring the temperature and pressure of the flow immediately after the fluid exits the vaporizer and prior to the mixing tee. The time-averaged enthalpy of the transient vapor stream is known by measuring the temperature and pressure of the transient stream within the vapor capacitor. The time-averaged enthalpy of the combined superheated vapor stream, $i_{v,sh}$, is calculated using an energy balance on the transient-steady mixing tee:

$$i_{v,sh} = \frac{\dot{m}_{v,\text{steady}} i_{v,\text{steady}} + \dot{m}_{v,\text{pulse}} i_{v,\text{pulse}}}{\dot{m}_v} \ . \tag{5.2}$$

After the steady vapor and transient vapor streams mix, the regression is executed in a manner identical to that done by Morse et al. (2021). The calculations performed in order to obtain local time-averaged values of heat flux, vapor quality, and heat transfer coefficient are outlined in Morse et al. (2021).

Uncertainty of measurements

The experimental uncertainties associated with the sensors, estimation procedures and calculated parameters are provided in Table 5.1. A thorough discussion on the methodology used for calculating uncertainty, specifically that of local HTC, local vapor quality, effective heat flux, and temporal dry fraction is provided in previous manuscripts Morse et al. (2021, 2024).

5.2.6 Experimental procedure

Prior to the start of data collection, the pulse generator tank is filled such that the tank is 35% liquid by volume. The saturation temperature of the two-phase mixture within the pulse

Parameter	Symbol	Uncertainty
Absolute pressure	P	300 Pa
Differential pressure	ΔP	7 Pa
Steady mass flux	G	0.7%
Transient mass flux	G_{pulse}	5%
Temperature	T	0.05 °C
Supplied heating power	$\dot{q}_{applied}$	6 W
Heat losses	$\dot{q}_{losses}$	10%
Effective heat flux	$\dot{q}''_{eff}$	0.5%
Heat transfer coefficient	h	1.5%
Local vapor quality	x	0.003
Change in vapor quality	δx	0.0005
Time-average dry fraction	f_{dry}	0.4%
Liquid-film thickness	δ	8.6 μm

Table 5.1: Uncertainties of process measurements

generator is increased to a desired set point by adding heat to the mixture. The pressure in the pulse generator is maintained within ±500 Pa by controlling the heating elements using a PID program within LabView. Steady-state vapor and liquid are introduced to the flow loop while the pulse generator builds pressure. When the pulse generator reaches the pressure set point, the transient vapor pulses are introduced to the flow loop. The pressure in the test section is adjusted by controlling the cold water supply to the condenser. After the test section pressure has reached the desired value and has stabilized for longer than 30 seconds, data acquisition begins.

Figure 5.3 shows an example of time traces of the signals used to identify dryout characteristics of the flow within the test section. The black line represents the effective heat flux applied to the window, $\dot{q}''_{eff}$, the red line represents the exterior wall temperature, T_{ext}, and the blue line represents the local saturation temperature, T_{sat}. The orange data represents the intensity ratio from the laser reflectance measurement. Finally, the vertical black dotted lines indicate when the camera trigger is activated and liquid-film thickness is measured. The camera takes approximately 5 minutes to save each data set. When the camera has finished saving one recording and as soon as the flow has reached a new quasi-steady equilibrium, the camera is triggered again to catch the liquid-film thickness of the new flow condition.

This process is repeated throughout the data collection.

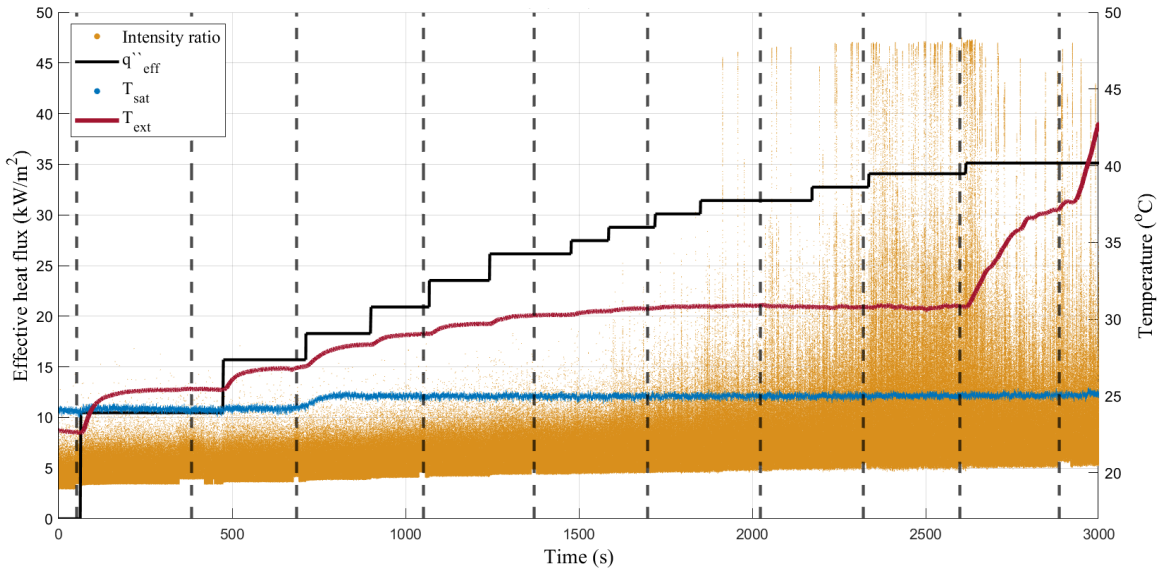

Figure 5.3: Example of data-trace taken under pulsed conditions at a pulse frequency of 0.5 Hz, $G = 148 \pm 8$ kg/m^2-s, and $x_{in} = 0.792$.

The dataset begins with the heating power off. At this point, the test section temperature is near ambient and there is very little heat transfer between the surroundings at the test section. Liquid-film thickness measurement is taken during unheated conditions and serves as a good representation of the behavior at the test section inlet. After this initial liquid-film thickness measurement, the heaters are turned on; this can be seen as the first step increase in heat flux in Figure 5.3. The test section exterior temperature, which serves as a proxy for the inner wall temperature during testing, is allowed to reach a new equilibrium temperature for at least 60 seconds prior to increasing the heating power again. This process is repeated until runaway temperature conditions are observed in the test section. The experiment is then concluded.

5.3 Results

In this section, a combination of time-averaged and time-resolved techniques are utilized to investigate what influence flow oscillations have on engineering quantities of interest, namely heat transfer coefficient and dryout heat flux.

All of the experimental results were obtained using saturated R245fa as the working fluid. The mass flux investigated was $G = 150$ kg/m^2-s, and the range of vapor quality considered was from 0.7 to 1. The saturation pressure within the test section was held constant at 150 kPa. The effective heat flux was varied between 0 - 50 kW/m^2. The pulse amplitudes were 5% and 10% of G, and the pulse frequencies investigated ranged from 0 - 5 Hz.

5.3.1 The influence of pulse amplitude

This section investigates the evolution of the liquid film under oscillating flow conditions. The figures in this section display snapshots of liquid-film thickness (black data) and intensity ratio (orange data) measurements for varied heating power. The power spectrum density (PSD) calculated from both intensity ratio and liquid-film thickness are to the right of each time trace. The heat input to the fluid is increased in subsequent subfigures; the first shows data for adiabatic conditions in the annular flow regime, and the final shows data taken under heated conditions resulting in intermittent dryout flow.

The data shown in Figure 5.4 are time traces for steady flow conditions under varying heater power. Figure 5.4a shows liquid-film thickness measurements for unheated conditions. There is no large peak indicating the disturbance wave frequency in the PSD liquid-film thickness signal. The high-speed video recorded to make the liquid-film thickness measurement is used to estimate a disturbance wave frequency of 13 Hz for the conditions shown in Figure 5.4a. The disturbance wave frequency and velocity for adiabatic flow conditions in Figure 5.4a is equivalent to the inlet conditions for heated flow conditions, such as those in Figures 5.4b and 5.4c. Disturbance waves occur over a distribution of wave frequencies.As heat is

input into the fluid and mass is vaporized from the liquid film, the disturbance wave characteristics are dynamic. The measurements in Figures 5.4b and 5.4c show that for heated flows there is a decrease of both disturbance wave velocity and frequency that occurs prior to the transition from annular to intermittent dryout flow. This behavior agrees with previous observationsMorse et al. (2021, 2024).

Figure 5.5 displays data for small amplitude pulses, at frequency of 1 Hz. For the unheated conditions shown in Figure 5.5a, the liquid film is relatively thick having a mean thickness of over 100 μm. The liquid-film thickness PSD show peaks corresponding to the pulse frequency. This means that even small transient oscillations in the vapor flow are capable of influencing the liquid film. The snapshot shown in Figure 5.5b are for heated conditions. Peaks of the corresponding pulse frequency occur in the PSD at nearly the same magnitude as in the unheated case. Only a small increase in heating power results in cyclic dryout conditions, as seen in Figure 5.5c. The peaks in liquid-film thickness PSD have increased in magnitude for both frequencies. A peak in the intensity ratio PSD can be seen at the pulse frequency in Figure 5.5c for 1 Hz pulses. Under these flow conditions, cyclic dryout occurs at a frequency equal to that of the pulses.

The influence of the transient vapor on the liquid film is even more obvious with larger amplitude pulses. Data taken under conditions with pulse amplitude of $\pm$ 10% of G can be seen in Figure 5.6 for 0.5 Hz pulses. Figure 5.6a displays the film thickness measurements for unheated conditions. The peak in the liquid-film thickness PSD for pulses of $\pm$ 10% of G is similar to that seen for $\pm$ 5% of G in the previous section. However, once heat is introduced the peaks in the PSD have magnitudes that are similar to the standard deviation of the liquid-film thickness, as seen in Figure 5.6b. Under cyclic dryout conditions, the large pulses dominate the motion of the liquid film. In Figures 5.6c, the peaks in liquid-film thickness PSD at the corresponding pulse frequency have increased further. In addition, peaks in the intensity ratio PSD indicate that the cyclic dryout occurs at the pulse frequency.

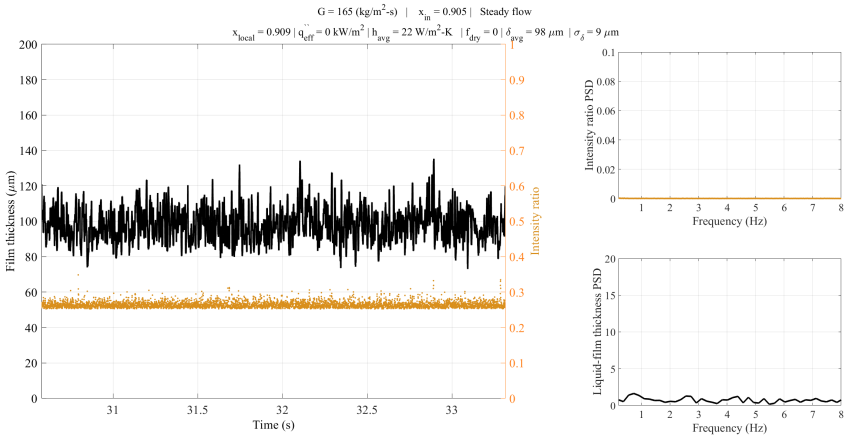

(a) Unheated conditions

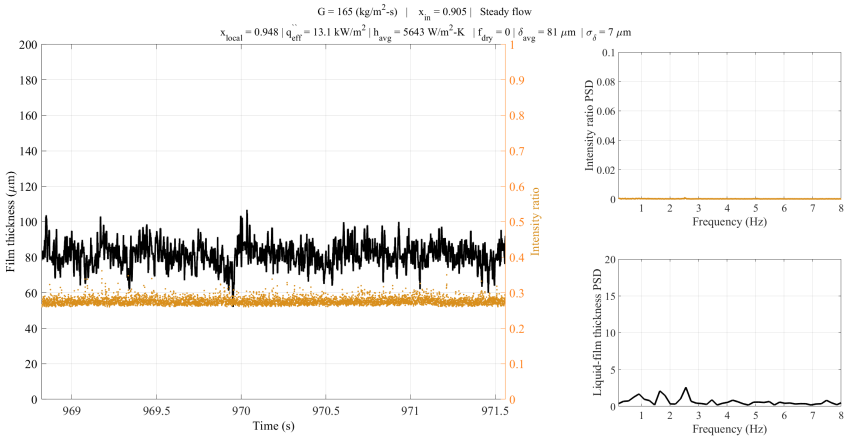

(b) Heated conditions

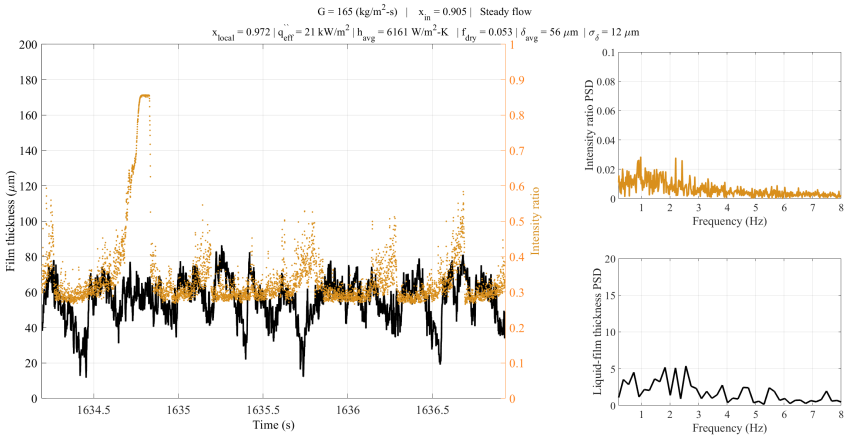

(c) Dryout conditions

Figure 5.4: Steady state flow conditions.

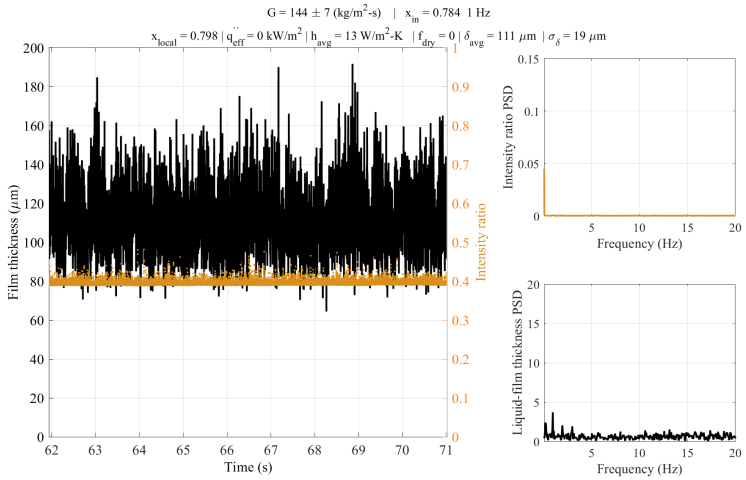

(a) Unheated conditions

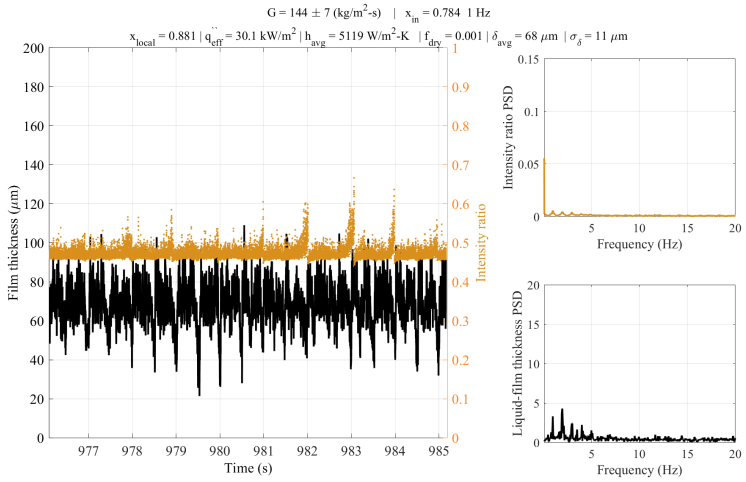

(b) Heated conditions

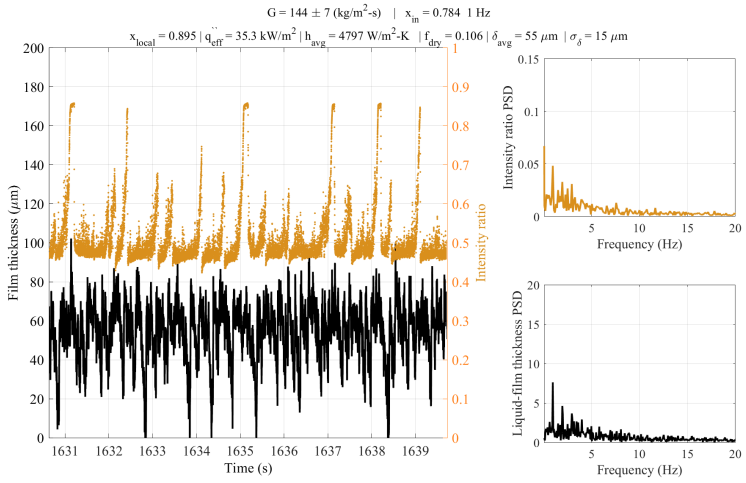

(c) Dryout conditions

Figure 5.5: 1 Hz pulses ± 5% of G; small amplitude pulses

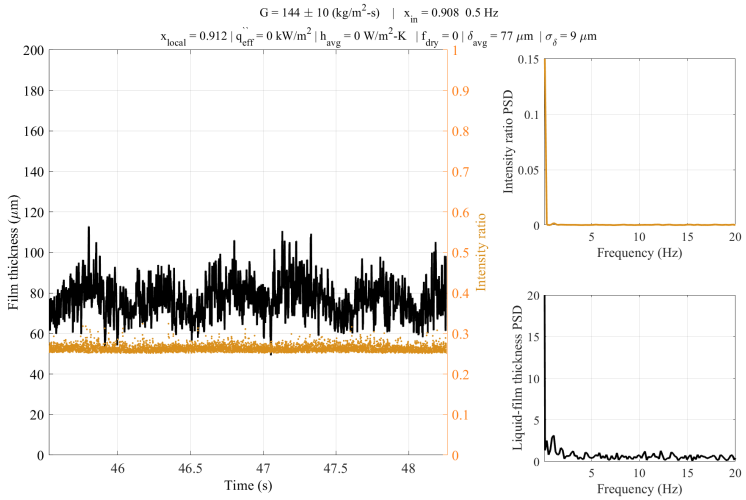

(a) Unheated conditions

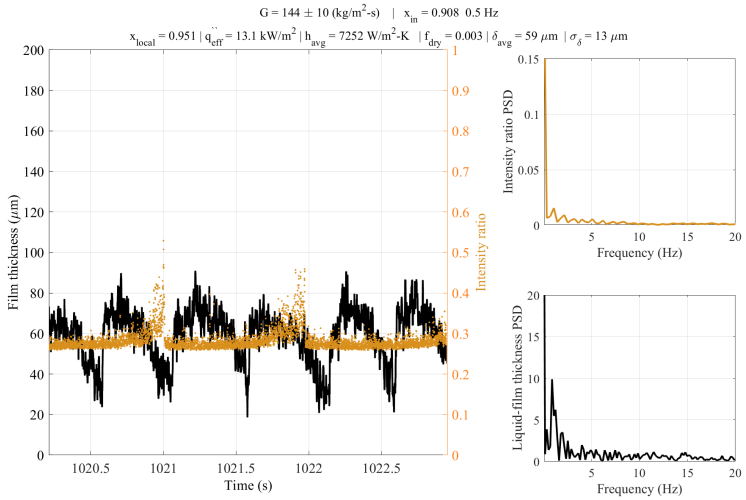

(b) Heated conditions

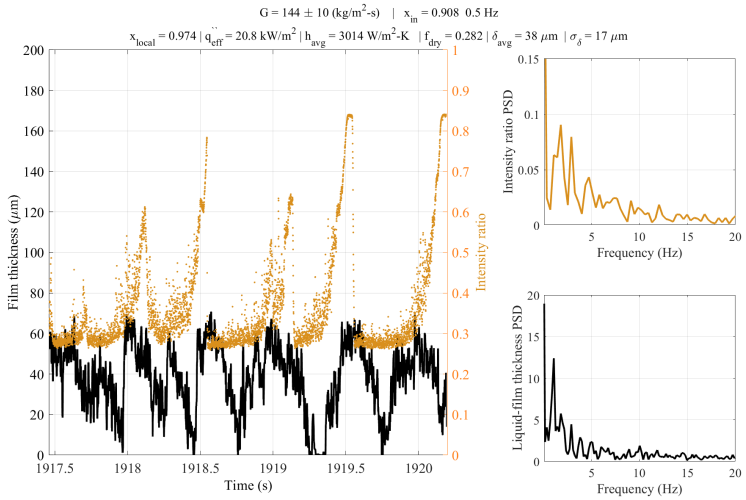

(c) Dryout conditions

Figure 5.6: 0.5 Hz pulses ± 10% of G; large amplitude pulses

5.3.2 Heat transfer coefficient

Figure 5.7 shows the time-averaged HTC as a function of local vapor quality in black, and the temporal dry fraction, f_{dry}, as a function of vapor quality in red. For $x < 0.845$, no dryout events are detected and therefore $f_{dry} = 0$. These data points are unseen on the plot because of the logarithmic axis for f_{dry}. It is only once dryout events are detected that the data for f_{dry} appears on the plot. The initial increase in f_{dry} from 0 to 10^{-2} coincides with an increase in the local HTC. The heat flux associated with OBC is the heat flux at which the local maximum in HTC occurs. For all flow conditions investigated, the value of h increases when dryout events first occur, and h reaches a maximum under conditions where cyclic dryout occurs such that $f_{dry} < 0.05$. This behavior is nearly identical to the behavior observed for steady flows Morse et al. (2021).

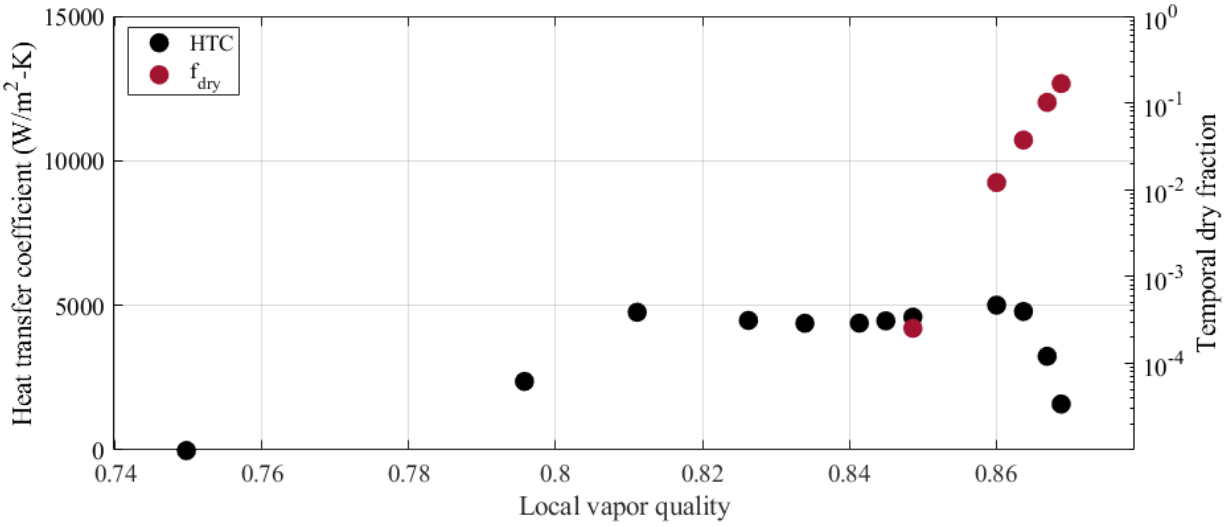

Figure 5.7: Local HTC and f_{dry} as a function of local vapor quality taken under pulsed conditions with a pulse frequency of 0.5 Hz, $G = 148 \pm 8$ kg/m^2-s, and $x_{in} = 0.792$.

The maximum measured time-averaged HTC prior to the occurrence of dryout events, h_{tp}, and the single-phase vapor HTC, h_v, depending on the inlet flow conditions. In general, h_{tp} and h_v increase with increasing G and with significant changes of inlet x. In order to

compare data with different inlet conditions, a normalized HTC, $\mathcal{H}$, is calculated as,

$$\mathcal{H} = \frac{h - h_v}{h_{tp} - h_v} \ , \tag{5.3}$$

where h is the measured time-averaged HTC. The correlation of Dittus and Boelter (1930) is used to estimate h_v. A normalized HTC, $\mathcal{H}_{weighted}$, based on weighting h_v by the dry time and h_{tp} by the wet time is calculated as,

$$\mathcal{H}_{weighted} = 1 - f_{dry} \ . \tag{5.4}$$

Figure 5.8 displays experimental results of $\mathcal{H}$ as a function of f_{dry} for varying flow conditions. Figure 5.8a shows data for flow conditions with pulses of $\pm$ 5% of G. The results for data taken under flow conditions with pulses of $\pm$ 10% of G are shown in Figure 5.8b. For these first two plots, the data points are colored with respect to the pulse frequency, and the black-dotted line represents $\mathcal{H}_{weighted}$. Finally, data taken under steady flow conditions is shown in Figure 5.8c.

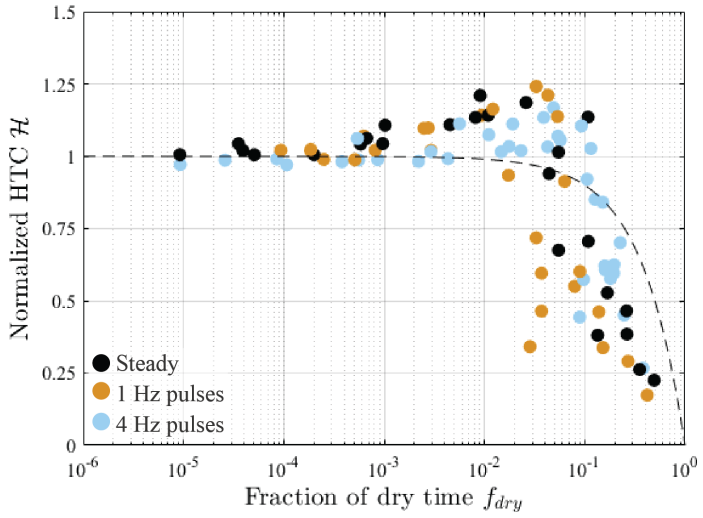

(a) Pulse amplitude of ± 5% of G.

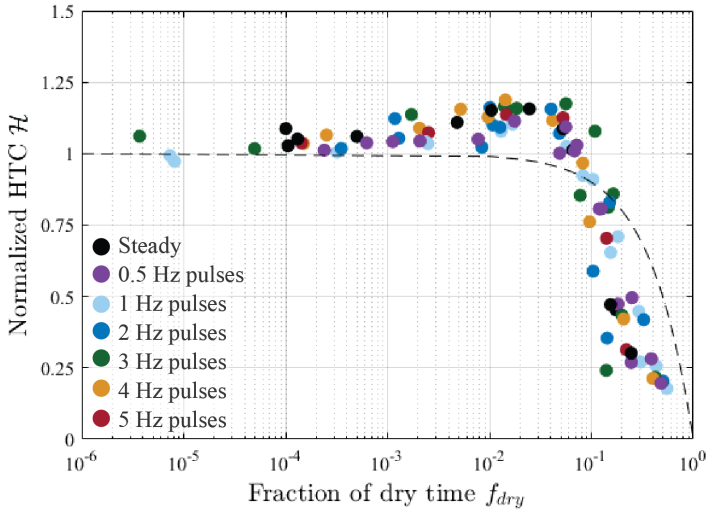

(b) Pulse amplitude of ± 10% of G.

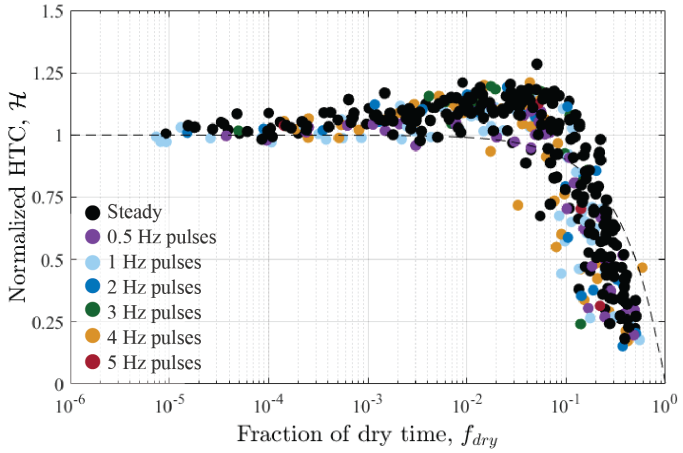

(c) All data used in this work (pulsed and steady) overlay on steady state data from Morse et al. (2021).

Figure 5.8: Normalized HTC, $\mathcal{H}$, as a function of f_{dry}.

For all flow conditions investigated, pulsed at varying frequencies or steady flow conditions, the $\mathcal{H}$ exhibited the same behavior with respect to f_{dry}. When dryout events first occur and f_{dry} is only slightly larger than zero, $h \approx h_{tp}$ and therefore $\mathcal{H} \approx 1$. Between $0 < f_{dry} < 10^{-2}$, increasing f_{dry} results in an increase $\mathcal{H}$ as the HTC at the surface is enhanced relative to h_{tp}. Figure 5.8 shows that each flow configuration experiences a local maximum in $\mathcal{H}$ at $f_{dry} \approx 0.05$. Increasing f_{dry} past 0.05 results in dramatic decrease of $\mathcal{H}$.

5.3.3 Dryout and OBC heat flux

Experimentally measured dryout heat flux and the OBC heat flux are shown as a function of pulse frequency in Figure 5.9 for two different inlet vapor qualities. The top band of data in Figure 5.9 corresponds to inlet flow conditions with relatively low vapor quality and thick liquid film, and therefore require more heat flux to reach dryout conditions. The bottom band of data in Figure 5.9 corresponds to inlet flow conditions with relatively high vapor quality and thin liquid film where a smaller amount of heat flux is necessary to reach dryout conditions. For both inlet conditions, there is a decrease in both DHF and OBC heat flux at low frequencies.

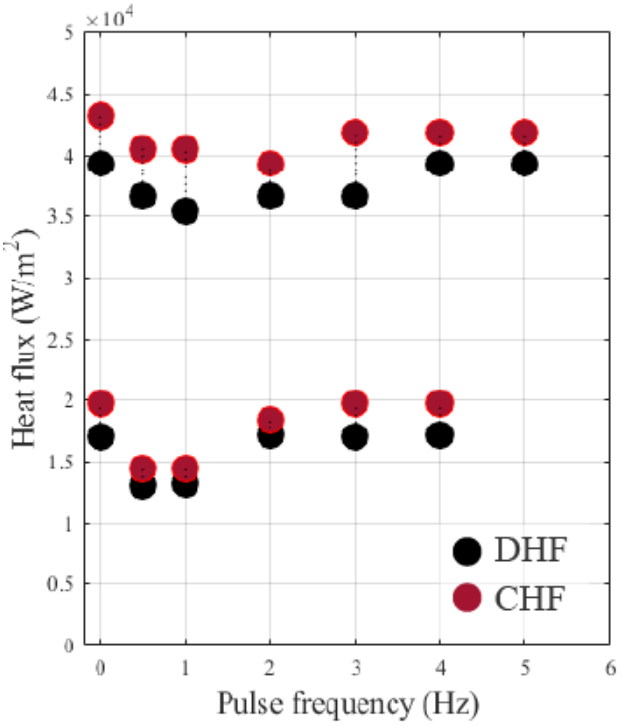

Figure 5.9: Dryout heat flux and OBC heat flux as functions of pulse frequency.

The decrease in heat flux for low-f3quid film, especially between the first dryout event and the OBC, i.e. $0 < f_{dry} < 0.05$. The large amplitude pulses cause the liquid film to dryout at a heat flux smaller than the steady flow as seen in Figure 5.9.

5.3.4 Dryout statistics

Statistics pertaining to dryout duration and time between dryout events for varying f_{dry} are presented in this section. Statistics for flow conditions with pulse amplitudes of $\pm$ 10%, and frequencies of 0.5, 1, 2, and 4 Hz are shown in Figures 5.10, 5.11, 5.12, and 5.13, respectively. The dryout statistics look similar for the pulses at lower frequencies of 0.5 and 1 Hz. At low values of f_{dry}, the time between dryout events is consistently 1 or 2 seconds. Very few dryout events occur other than the events associated with the pulses. However for $f_{dry} > 0.2$, the liquid film consistently dries out after approximately 0.25 seconds; this is consistent with behavior observed for steady flowsMorse et al. (2021). The statistics for

2 Hz pulses in Figure 5.12 highlight this phenomenon. The large peak at 0.5 seconds in the time between dryout statistics corresponds to the pulse frequency of 2 Hz. Under the conditions at which dryout first occurs, dryout events will not necessarily occur every time a wake region passes by the local position. For this reason, under 2 Hz pulsed conditions dryout events occur at 1 second, 1.5 seconds , 2 seconds and so on, in addition to the period of the pulses, 0.5 seconds. The effect of the pulses on the liquid film begins to wane for higher frequencies. The dryout statistics for 4 Hz pulses are displayed in Figure 5.13. Under 4 Hz pulses, the dryout behavior is very similar to that of the steady flow conditionsMorse et al. (2021). The dryout statistics show that dryout events occur at a frequency equal to that of the pulses for low frequencies. For high-frequency pulses, the dryout statistics resemble that taken under steady flow conditions.

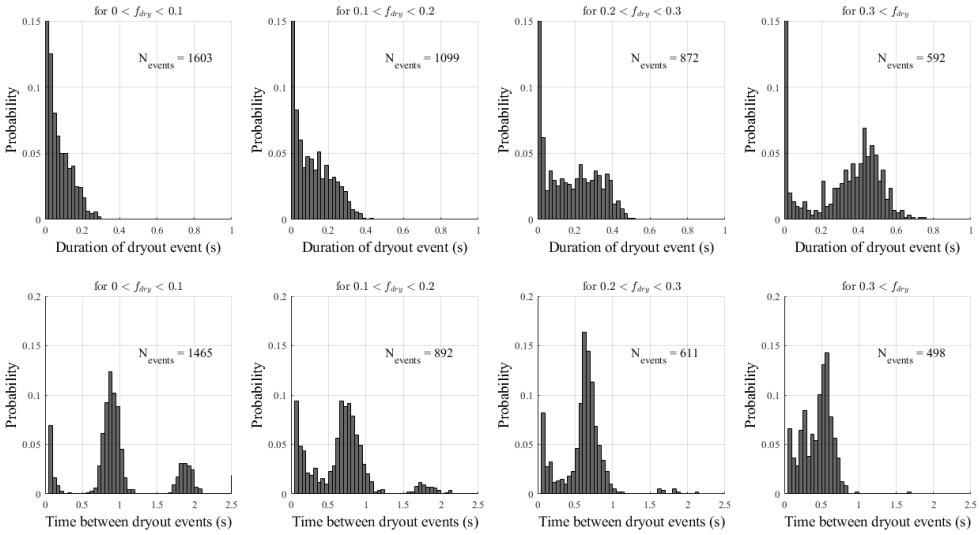

Figure 5.10: Dryout statistics for the duration of dryout events (top) and time between dryout events (bottom) for varying f_{dry} with 0.5 Hz pulses.

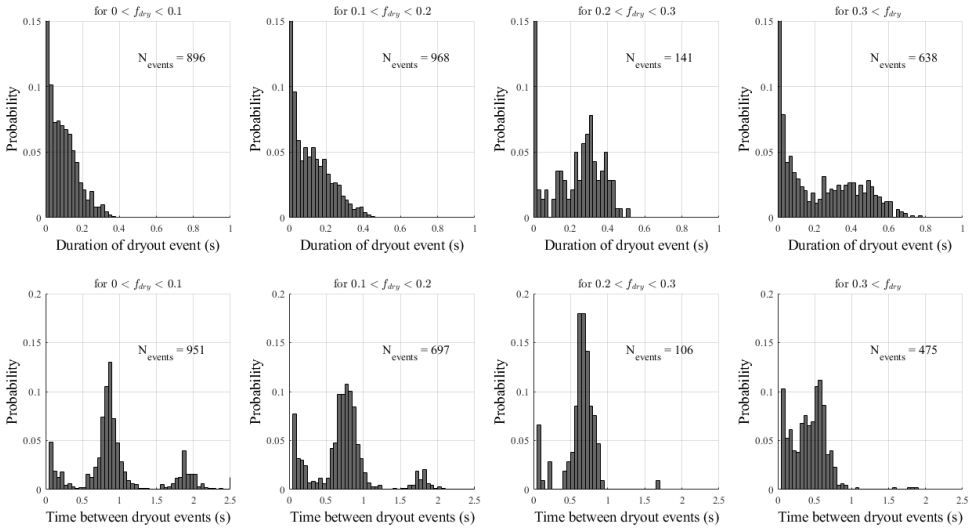

Figure 5.11: Dryout statistics for the duration of dryout events (top) and time between dryout events (bottom) for varying f_{dry} with 1 Hz pulses.

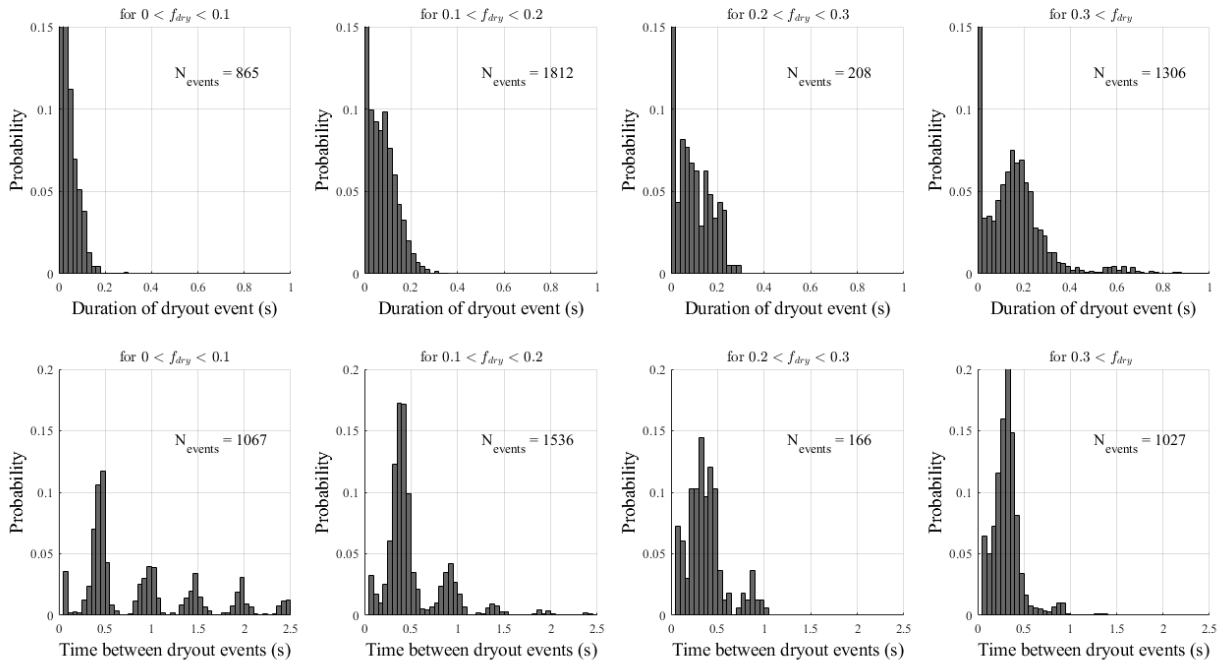

Figure 5.12: Dryout statistics for the duration of dryout events (top) and time between dryout events (bottom) for varying f_{dry} with 2 Hz pulses.

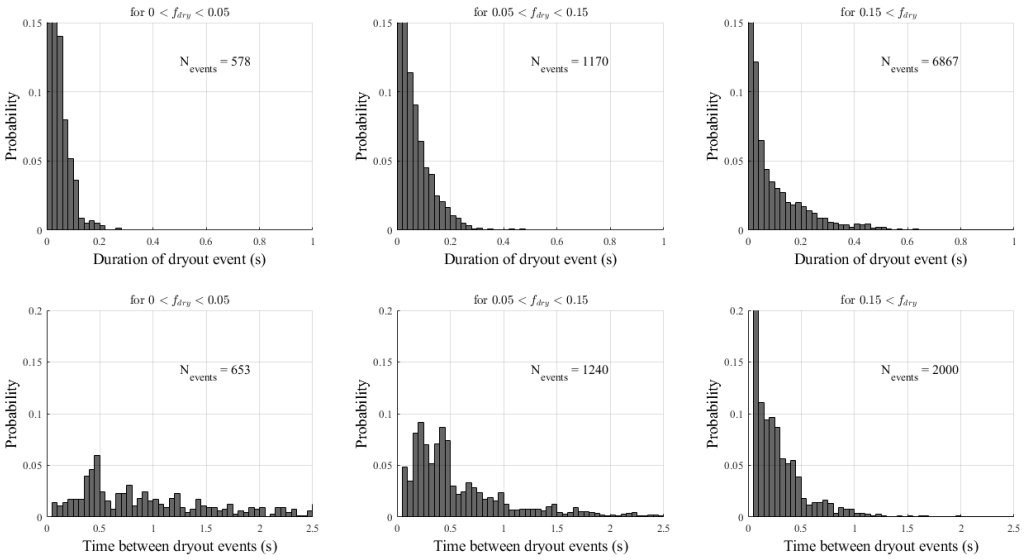

Figure 5.13: Dryout statistics for the duration of dryout events (top) and time between dryout events (bottom) for varying f_{dry} with 4 Hz pulses.

5.3.5 Disturbance wave frequency

Figure 5.14 shows liquid-film thickness measurements made at varying heating power and under steady-state conditions. The steady-state liquid film is composed of multiple wave functions stacked upon one another. The distribution of wave frequencies ranges over a finite range and is centered a sort of 'natural frequency'. For the data set shown in Figure 5.14, the local flow conditions result in a natural frequency of $\approx$ 2.5 Hz. For all steady flow conditions investigated, the disturbance wave frequency in annular flow decreases with increasing heat flux. The frequency of the disturbance waves approaches the natural frequency in the intermittent dryout flow regime.

Figures 5.15, and 5.16 show thickness measurements made at varying heating power for pulse frequencies of 0.5 and 4 Hz, respectively. The disturbance waves are dominated by the low-frequency pulses in 5.15. Just by observation of the signal, it's very obvious that the wave frequency has aligned with the pulse frequency. However, the effect on the disturbance waves begins to diminish at higher frequencies. The liquid-film thickness under 4 Hz pulses can be seen in Figure 5.16. The wave shape and wave frequency under 4 Hz pulses look similar to the steady state data shown in Figure 5.14.

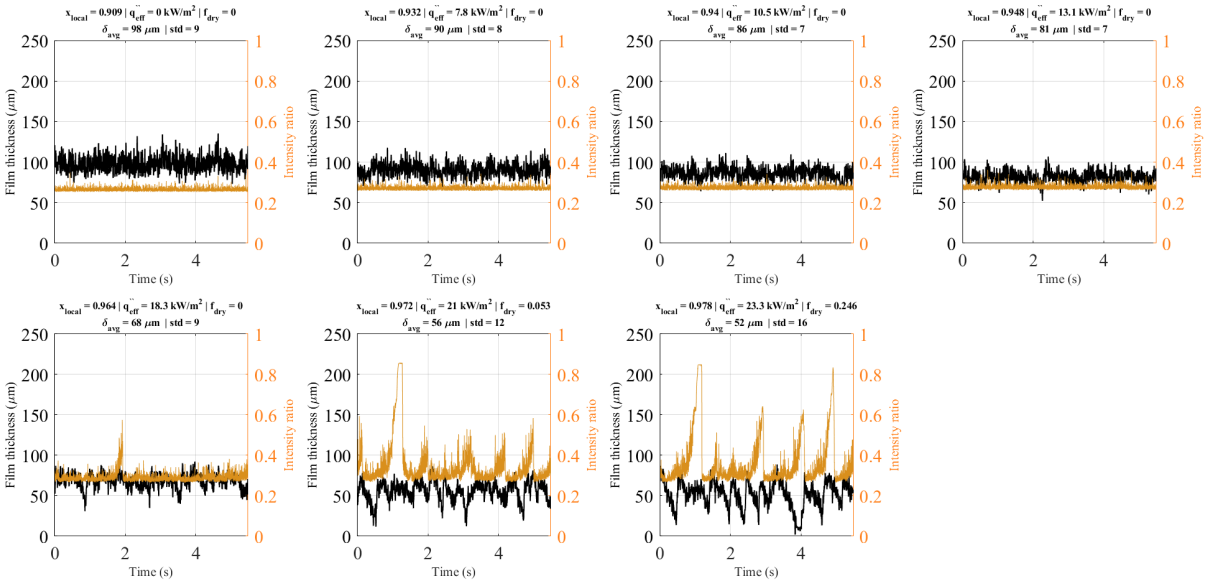

Figure 5.14: Time trace (top) and liquid-film thickness measurements (bottom) for steady flow.

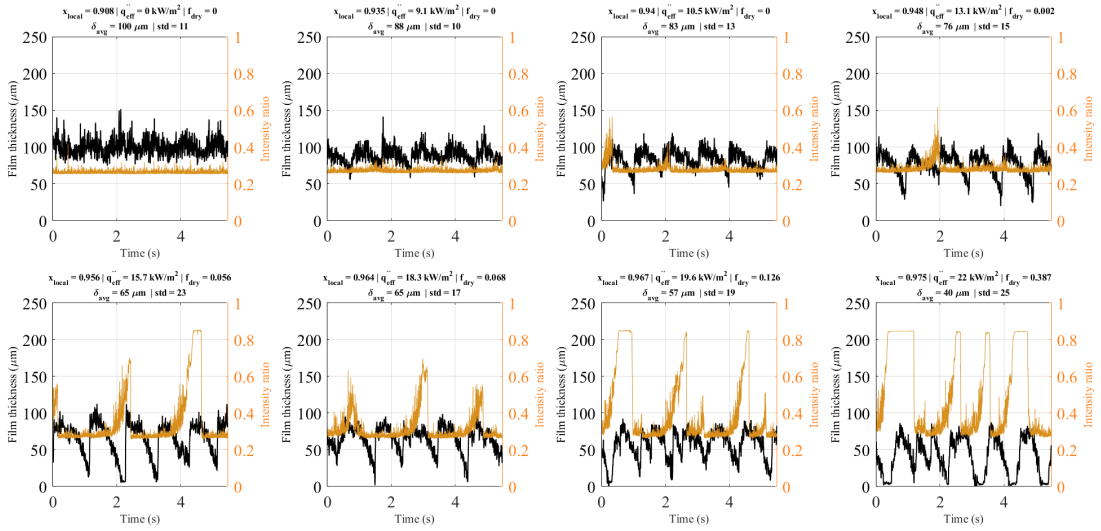

Figure 5.15: Time trace (top) and liquid-film thickness measurements (bottom) for 0.5 Hz pulses.

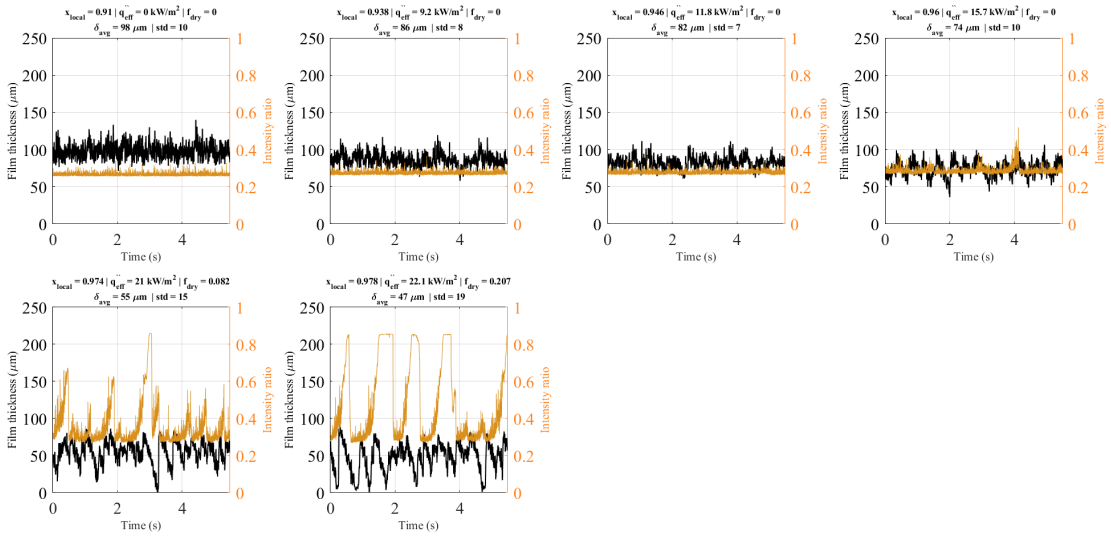

Figure 5.16: Time trace (top) and liquid-film thickness measurements (bottom) for 4 Hz pulses.

5.3.6 Discussion

The relationship between dryout heat flux and wave frequency is in agreement with the dryout mechanism described by Morse et al. (2024). The results of this work confirm that large disturbances (big pulses) can manipulate the disturbance wave characteristics, namely the wave frequency. Control of the wave frequency allows further confirmation of the dryout mechanism: base film in the wake of a disturbance wave is nearly stagnant and vaporizes in between waves; the passage of a disturbance wave is the mechanism of rewetting the heated surface. Direct observation can be made using high-speed video of the flow field. Video captures consecutive dryout events occurring at a frequency equal to the pulse frequency. This video will be submitted as supplemental material: `https://youtu.be/sfs1eXgRdmI?si=3GYcNLbUA31ooOkG`.

5.4 Summary

In this work, experiments were performed to investigate the impact of flow oscillations on liquid-film dryout. The density-vapor oscillations were produced using vapor injections. Measurements under oscillating flows are compared to those measured during steady flow. The following conclusions are made based on the experimental results:

- Pulsed vapor pulses (density-wave oscillations) can alter important characteristics of disturbance waves, most significantly the wave frequency.
- For all flow conditions investigated, both steady-state and pulsed data, the normalized HTC, $\mathcal{H}$, reaches a maximum when $f_{dry} \approx 0.05$. The heat flux at which the maximum in $\mathcal{H}$ occurs is the OBC heat flux.
- For decreases in oscillation amplitude and increases in pulse frequency, the influence of the oscillations is diminished.
- Pulses of low frequency and high amplitude, such as 0.5 and 1 Hz, have the strongest observed impact on the flow field. Under these conditions, the following was observed:
  - For heated conditions approaching the intermittent dryout flow regime, the pulse frequency dominates over any other frequency in the liquid film. The result is a more 'ordered' or predictable flow, meaning the probability of a wave passing any one location at a frequency other than the pulse frequency is near zero.
  - The stream-wise momentum of the liquid film is confined mostly to the disturbance waves making the fluid in the wake region nearly stagnant; the same behavior occurs under steady flows which is why dryout events occur in the wake of disturbance waves (Morse et al. (2021)).

- For local conditions where the heat flux is much less than dryout heat flux, the transient vapor pulses have no significant impact on the liquid-film behavior.
- High-speed video shows cyclic dryout occurring exactly at the pulse frequency. Confirming the interpretation of the liquid-film thickness results.
- Controlling the disturbance wave frequency allows for some control of the dryout heat flux and the conditions that lead to CBT. For this reason, for wave frequencies of 0.5 Hz and 1 Hz, there is a decrease in the values dryout heat flux and OBC heat flux when compared to steady flow conditions.

Data sets

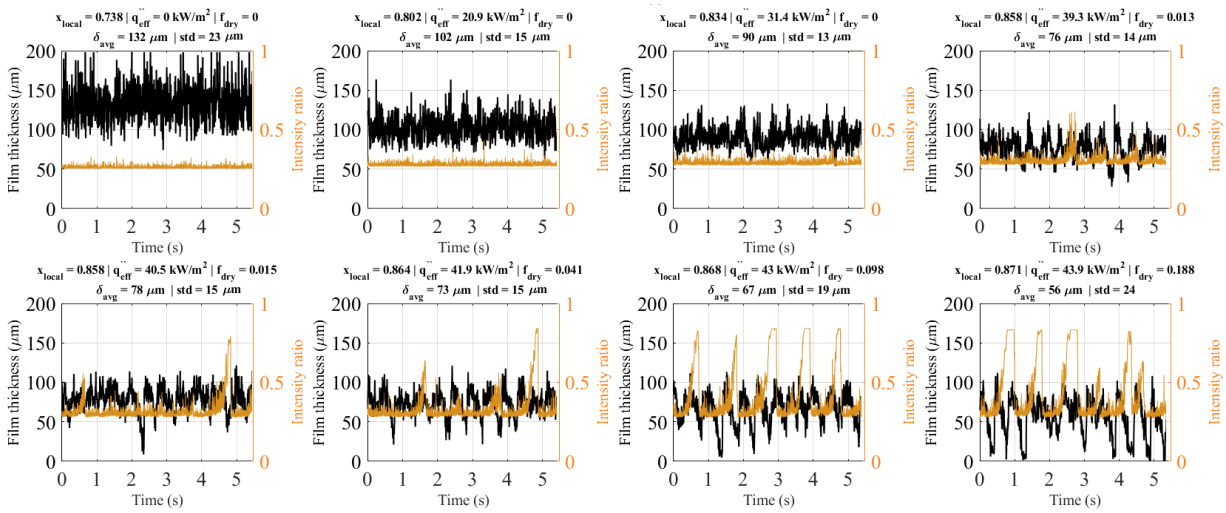

Figure 5.17: Time trace (top) and liquid-film thickness measurements (bottom) for 1 Hz pulses.

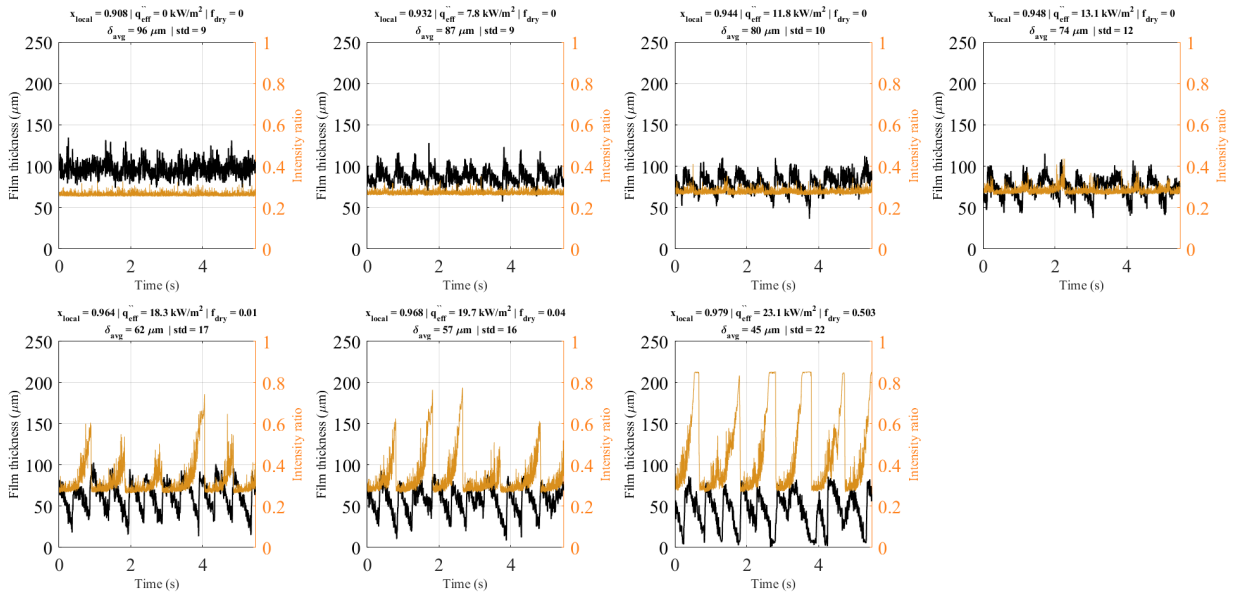

Figure 5.18: Time trace (top) and liquid-film thickness measurements (bottom) for 2 Hz pulses.

Chapter 6

Mechanistic modeling

This section describes a simple framework for future models to predict local time-averaged values for HTC and heat flux related to dryout using the measured liquid-film characteristics. The model framework is applicable for saturated annular flow under heated conditions within the annular and intermittent dryout flow regime.

6.1 Local HTC

The liquid-film thickness measurement in Figure 4.3c is used as a sample data set to demonstrate the model. The measured liquid-film thickness from Figure 4.3c is shown as a time trace in Figure 6.1. The raw measured data is shown in orange, and in black is a filtered version of the signal using a moving median filter with a window size five of data points. The dotted line represents the value of minimum possible film thickness, δ_{min}, under which the amount of liquid present at the local position is no longer able to provide a stable film and the film breaks into rivulets; a correlation is needed to estimate δ_{min}. It is worth highlighting that the amount of time it takes for a disturbance waves to rewet a local dry position is very fast (approximately 10 ms), compared to the time it takes for the base film to vaporize in the wake of a disturbance wave (100's of ms). This can be seen in Figure 6.1 as a sudden increase in liquid-film thickness at the end of a dryout event that corresponds to

the arrival of a disturbance wave. In this flow condition, the estimated base-film thickness is approximately 45 microns. The waves pass a local position quickly and leave the base film in the wake. This makes the stream-wise length of the base-film zone significant when compared to that of the waves.

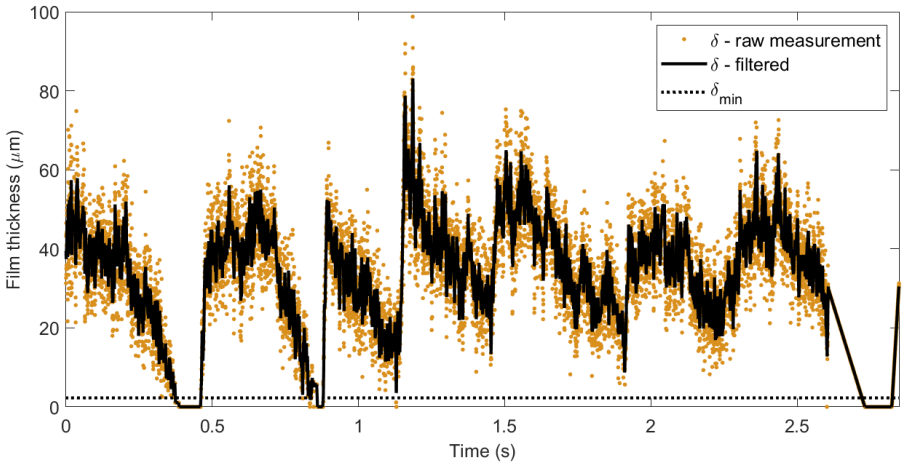

Figure 6.1: Time trace of liquid-film thickness during cyclic dryout within the intermittent flow regime. The corresponding flow conditions are the following: $G = 167$ kg/m^{2}s, $\dot{q}''_{eff} = 33.6$ kW/m^2, $x_{local} = 0.866$, $f_{dry} = 0.073$

6.1.1 Framework

A simplified schematic illustrating liquid-film dryout under conditions within the intermittent dryout regime is shown in Figure 6.2. At a given position, a disturbance wave will pass and rewet a local region that has experienced a dryout event. The disturbance wave leaves a new base-film layer in the wake of the wave. The base film vaporizes, decreasing the film thickness and reducing the thermal resistance. Eventually, the liquid-film thickness reaches a critical value, breaks up and another dryout event occurs. The local position will then remain dry until the passage of another wave.

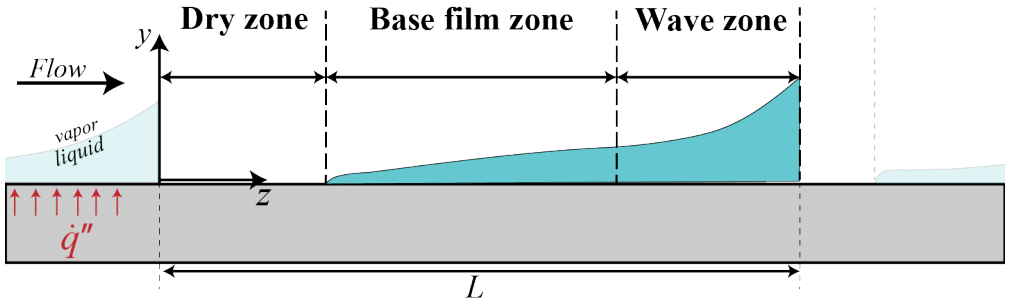

Figure 6.2: Schematic showing the behavior of the liquid film during intermittent dryout-rewet.

6.1.2 Assumptions

The following assumptions are made in the development of this model:

- Heat is transferred from the wall to the fluid in the direction perpendicular to the flow.
- The temperature difference associated with the heat transfer process is the difference between the heated surface temperature T_{wall} and the saturation temperature T_{sat}.
- The liquid properties are unchanging and evaluated at the saturation conditions.
- Vaporization is the only mode of phase change; nucleate boiling is suppressed in this region.
- The impact on local HTC from liquid droplets depositing on the heated surface during dryout events is neglected; this assumption is not proper for all flow conditions.
- The liquid film has velocity only in the streamwise direction. The waves travel relatively fast but the base film has a small velocity that approaches zero.
- The heated surface is able to reach a quasi-steady temperature that can be time-averaged; runaway temperature conditions are not considered.

Model outline

The framework presented here models the liquid film as a combination of two layers (in the wall-normal direction) separated in three zones (in the axial direction parallel to the flow). The two layers of the liquid film are a superposition of waves on top of a base film. The three zones are depicted in Figure 6.2. The three zones are the dry zone, the base-film zone, and the wave zone. The hypothesis in this work is that conduction, through an effective length associated with the base film, is the primary mode of heat transfer in this type of flow configuration. The thermal resistance associated with conduction through the effective length is much greater than the other thermal resistances associated with turbulent or well-mixed regions of the liquid film.

The dry zone occurs when the heated surface is locally dry, which is when $\delta < \delta_{min}$. The minimum liquid-film thickness that can provide a stable film, δ_{min}, is estimated using a correlation from Chun et al. (2003). For dry conditions, the local HTC can be assumed to be equal to the convection coefficient of a single-phase fluid. The correlation of Dittus and Boelter (1930) has been shown to provide accurate estimates for local HTC under single-phase conditions. The vapor mass flux, G_v, is obtained by

$$G_v = Gx \tag{6.1}$$

where G is the total mass flux of the fluid, and x is the local vapor quality. The vapor-only Reynolds number is defined by,

$$\mathrm{Re}_v \triangleq \frac{G_v D_h}{\mu_v} \tag{6.2}$$

where D_h is the hydraulic diameter and μ_v is the viscosity of the vapor phase. The single-phase vapor HTC, h_v, is obtained using the Dittus and Boelter (1930) correlation,

$$h_v = \frac{k_v}{D_h}\, 0.023 \mathrm{Re}_v^{0.8} \mathrm{Pr}_v^{0.4} \tag{6.3}$$

where k_v is the vapor thermal conductivity, and Pr_v is the Prandtl number of the vapor phase.

The other two zones occur when the local position is wet. In the liquid phase, it is assumed that energy is transferred from the heated surface (the inner wall) to the liquid film by conduction through an effective conduction length. Under conditions in which a relatively thick film exists, referred to as the wave zone in this current work, the effective conduction length is taken as the thermal boundary layer near the wall. When the liquid film is smaller than the thermal boundary layer, the model takes the liquid film thickness as the effective conduction length. This zone is referred to as the vaporizing base-film zone (or simply the base zone).

For any position along the heated length the local liquid mass flow rate, $\dot{m}_l$, is

$$\dot{m}_l = G\,(1-x)\,A_c \tag{6.4}$$

where A_c is the cross-sectional area of the flow channel. The total value of $\dot{m}_l$ can be described as the sum of the film and droplet components:

$$\dot{m}_l \triangleq \dot{m}_f + \dot{m}_d \tag{6.5}$$

where $\dot{m}_f$ is the mass-flow rate of the liquid film and $\dot{m}_d$ is that of the droplets. The liquid-film mass flow rate, $\dot{m}_f$, is defined in this current work as,

$$\dot{m}_f = \rho_l u_f \Pi \bar{\delta} \tag{6.6}$$

where Π is the wetted perimeter of the flow channel, and $\bar{\delta}$ is the time-averaged liquid-film thickness. The droplet mass flow rate is,

$$\dot{m}_d = e_d \dot{m}_l \tag{6.7}$$

where e_d is the fraction of liquid entrained as droplets and therefore ranges from 0 to 1. In this current work, the correlation of Cioncolini and Thome (2012) is used to estimate the value of e_d. This specific correlation is utilized because it was built using a large database with many different fluids over a wide range of operating conditions. In addition, the correlation of Cioncolini and Thome (2012) has shown to provide accurate estimates for entrainment in previous studies performed within the same experimental facility as the current work Rodarte (2015). Equations 6.4, 6.6, and 6.7 are substituted into Equation 6.5, and the equation is rearranged to solve for the film velocity:

$$u_f = \frac{GA_c\left(1-x\right)\left(1-e_d\right)}{\rho_l \Pi \bar{\delta}} \ . \tag{6.8}$$

A steady-state momentum balance on the entire liquid film provides,

$$\tau_w = \tau_{int} - \frac{dP}{dz}\bar{\delta} - \rho_l g \bar{\delta} \tag{6.9}$$

where τ_w is the wall shear, τ_{int} is the interfacial shear between the vapor and liquid film, $\frac{\mathrm{d}P}{\mathrm{d}z}$, is the frictional streamwise pressure gradient, and g is the gravitational acceleration constant. The interfacial shear, τ_{int}, is estimated using a modified Wallis-type friction factor:

$$f_{int} = 0.005\left(1 + 300\frac{\sigma_\delta}{D_h}\right) \ , \tag{6.10}$$

where σ_δ is a term associated with the roughness of the film. In Moreira et al. (2020), it was shown that using σ_δ to be the standard deviation of the measured liquid-film thickness provided the best results for estimating pressure drop. For the data shown in Figure 4.3, the value of σ_δ is noted on top of each liquid-film thickness measurement. For the sample liquid-film thickness time trace considered throughout this work, from Figure 4.3c, this value is $\sigma_\delta = 15$ μm.

The interfacial shear between the vapor and liquid film is calculated as,

$$\tau_{int} = \frac{1}{2}\rho_v \left(u_v - u_f\right)^2 f_{int} \ . \tag{6.11}$$

Substituting in the τ_{int} from Equation 6.11 into the momentum balance in Equation 6.9, a value for τ_w is obtained. The normalizing value in the wall-bounded equations is the friction velocity, u^*, which is defined as:

$$u^* \triangleq \sqrt{\frac{\tau_w}{\rho_l}} \ . \tag{6.12}$$

Using the friction velocity, the distance from the wall in the direction perpendicular to the flow can be expressed in a dimensionless form as y^+:

$$y^+ \triangleq \frac{yu^*}{\nu_l} \tag{6.13}$$

where y is a physical distance from the heated surface within the flow field and in the wall-normal direction, and $\nu_l = \mu_l/\rho_l$. In the same fashion, a dimensionless liquid film thickness, δ^+, is expressed as:

$$\delta^+ \triangleq \frac{\delta u^*}{\nu_l} \ . \tag{6.14}$$

An analogy is made between the base film and viscous sublayer that exists for wall-bounded turbulent boundary layers in single-phase flows. Therefore, the value $y^+_{vs} = 5$ in wall units is used to determine the size of the momentum boundary layer,

$$\delta_m = \frac{y^+_{vs}\nu_l}{u^*} \ . \tag{6.15}$$

Regarding the thermal boundary layer, Polhausen (1921) found that the thickness of the boundary layer was dependent on the molecular Prandtl number, Pr_l, of the fluid. Using experimental data, Polhausen (1921) found that the thermal boundary layer thickness δ_t can be calculated as,

$$\delta_t = \frac{\delta_m}{\mathrm{Pr}_l^{1/3}}. \tag{6.16}$$

6.1.3 Model summary

The 2-layer 3-zone HTC model framework can then be summarized as:

$$h = \begin{cases} \frac{k_l}{\delta_t}, & \text{if } \delta_t < \delta \quad \textbf{Wave zone} \\ \frac{k_l}{\delta}, & \text{if } \delta_{min} < \delta < \delta_t \quad \textbf{Base-film vaporization zone} \\ h_v, & \text{if } \delta < \delta_{min} \quad \textbf{Dry zone} \end{cases} \tag{6.17}$$

The inputs for the model are the geometry of the flow channel (A_c, Π), the process flow conditions $(G, P, \dot{q}''_{eff})$, and local liquid-film thickness (δ). The output of the model is an estimated value for the local HTC between a heated wall and saturated working fluid.

6.1.4 Two-phase HTC instantaneous prediction

Figure 6.3 shows the same liquid-film thickness as in Figure 6.1 together with the predicted local time-resolved HTC made by the current model framework. When the film is thick it is in the wave zone, and the local HTC value is assumed constant. In the base zone, the local HTC can be seen to increase as film thickness becomes very small. The large increase in HTC prior to dryout causes the wall temperature to drop just before dryout events. Once the position becomes dry, the local HTC decreases to the vapor-only value. When dryout occurs, the wall temperature increases, and when the liquid film rewets the surface there is a quenching effect.

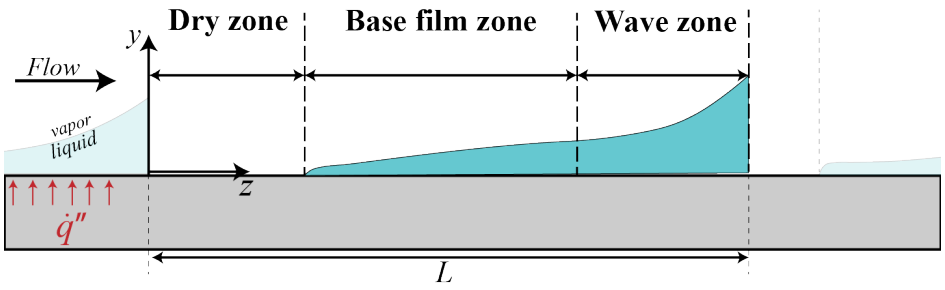

Figure 6.3: Time trace of liquid-film thickness during cyclic dryout (black), and predicted HTC (red).

A 1-D transient heat conduction model of the internal wall is developed to include the quenching effect related to energy storage in the channel wall. The governing partial differential equation is,

$$\alpha \frac{\partial^2 T}{\partial y^2} = \frac{\partial T}{\partial t} \tag{6.18}$$

where α is thermal diffusivity of the heater material, T is the temperature within the heater wall, and t is time.

The local HTC predicted using experimentally measured liquid-film thickness with Equation 6.17 is enforced as a boundary condition at the heated surface, that is,

$$\dot{q}^{"}_{applied} - k_{wall} \frac{\partial T}{\partial y}\bigg|_{y=0} = h\left(T_{wall} - T_{sat}\right) \tag{6.19}$$

where $\dot{q}^{"}_{applied}$ is the applied heat flux, k_{wall} is the conductivity of the wall material (glass in this experiment), and h is the predicted two-phase heat transfer coefficient. Losses through the test section are accounted for using a convective boundary condition:

$$k_{wall} \frac{\partial T}{\partial y}\bigg|_{y=-th} = h_{nat-conv}\left(T_{ext} - T_{amb}\right) \tag{6.20}$$

where th is the thickness of the heater wall, $h_{nat-conv}$ is the HTC associated with natural convection on the external surface of the test section, T_{ext} is the temperature on the exterior surface, and T_{amb} is the ambient temperature. The thickness of the wall in this experiment

is 3.0 mm, the external and ambient temperatures are both measured, and the natural convection HTC is estimated to be 10 W/m^2-K.

Each liquid-film thickness data set is repeated at least 20 times making a simulated dataset of one minute in duration, enough time for the 1-D transient simulation to reach a quasi-steady state. For flow conditions in which f_{dry} <0.10, the local HTC predicted is nearly unchanged when including the transient storage. However, the heated wall in this experimental apparatus is relatively small compared to heating elements in industrial applications. For flow conditions in which f_{dry} is large, there is a difference between 10-20% in the HTC prediction when accounting for the transient storage of energy in the wall.

6.1.5 Predictions compared to experimentally measured HTC

The predicted HTC from the present model is shown as a function of the experimentally measured HTC in Figure 6.4. For all mass flux values investigated, the current model predicts the two-phase HTC prior to the occurrence of dryout within 20% error bands.

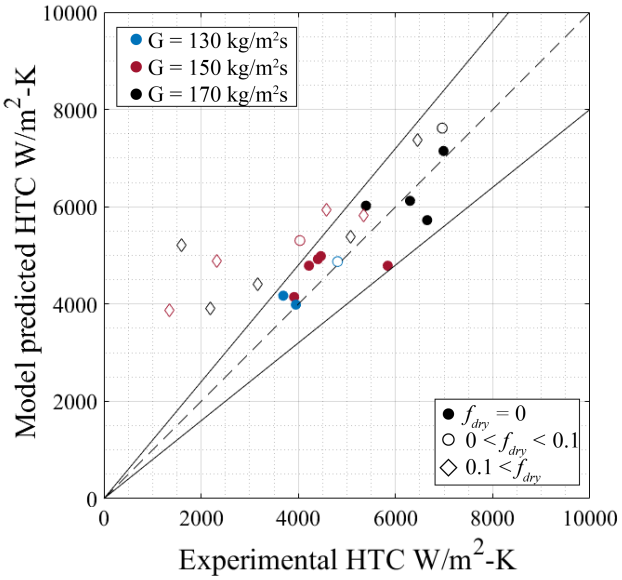

Figure 6.4: Predicted HTC as a function of experimentally measured HTC.

6.1.6 Normalized HTC and dry time fraction

Morse et al. (2021) showed that the heat flux for which the HTC reaches a maximum, defined in this work as the OBC heat flux, consistently occurs at f_{dry}= 0.05. For conditions in which 0.05 > f_{dry}, the HTC decreases significantly. The model accurately predicts this behavior, as shown in Figure 6.5.

Predictions of $\mathcal{H}$ using this framework are shown against a set of experimental data in Figure 6.5. The proposed model predicts the initial increase in the local HTC that occurs under flow conditions in which dryout events first occur but the time-averaged value of f_{dry} is small. The maximum value of $\mathcal{H}$ occurs at dry fractions of $f_{dry} \approx 0.05$ for both the experimental and model predicted values.

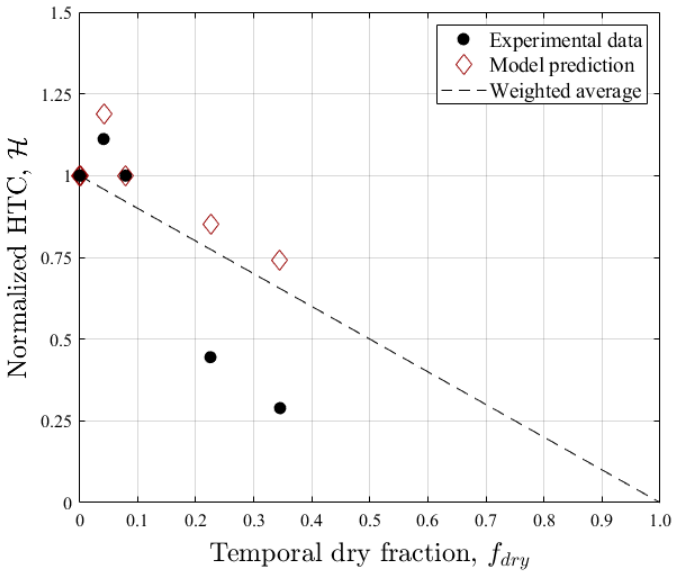

Figure 6.5: Normalized HTC, $\mathcal{H}$, as a function of the time-averaged dry fraction, f_{dry}.

Figure 6.5 shows the model over-predicts the HTC at large values of f_{dry} (f_{dry} >0.1). Under these conditions, the dry regions that occur during a single dryout event may not be uniform at the local position along the heated surfaceMorse et al. (2021). Because the measurement of the dry fraction is local, it is possible that we are underestimating the dry fraction over the entire heated surface and therefore over predicting the HTC. Analysis of

high-speed video shows that the center of the channel is the most likely radial position to rewet and the edges are most likely to remain dry at flow conditions with heat flux higher than that associated with the CBT.

6.2 Dryout and OBC heat flux

Analysis of the high-speed videos shows that the bulk of the liquid transport is provided by the waves and that the rewetting process occurs on time scales that are much smaller than the drying process. It has also been observed that the velocity of the base film in the wake of a disturbance wave is small relative to that of the disturbance wave itself. The measured base-film thickness in the intermittent dryout flow regime was observed to be on the order of 30 to 50 μm. In this flow regime, mass is removed from the base film in the wake of waves predominately by vaporization. Between two successive disturbance waves, the base film must be completely vaporized in order for a local dryout event to occur. The thickness of the base film and the disturbance wave frequency dictate the heat flux that will cause dryout events. Performing an energy balance on the base film, the energy per unit area needed to vaporize the base film can be written as,

$$\dot{q}^{"} t_{vap} = \rho_l i_{fg} \delta_b \tag{6.21}$$

where t_{vap} is the time it takes to vaporize the base film, ρ_l is the liquid density, i_{fg} is the enthalpy of vaporization, and f_{wave} is disturbance wave frequency. The time it takes to vaporize is related to f_{dry} by,

$$f_{dry} = \frac{t_{wave} - t_{vap}}{t_{wave}} \tag{6.22}$$

where t_{wave} is,

$$t_{wave} = \frac{1}{f_{wave}}. \tag{6.23}$$

Equation 6.23 is substituted into Equation 6.22 to get an expression for the vaporization time,

$$t_{vap} = \frac{1 - f_{dry}}{f_{wave}}. \tag{6.24}$$

The vaporization time in Equation 6.24 is substituted into Equation 6.21, and the equation is rearranged. Finally, the local heat flux required to reach a given f_{dry} can be written as follows:

$$\dot{q}^{"} = \rho_l i_{fg} f_{wave} \delta_b \left(\frac{1}{1 - f_{dry}} \right). \tag{6.25}$$

A local prediction for heat flux that corresponds to the OBC where maximum HTC occurs can be made using $f_{dry} = 0.05$. Predictions for the heat flux corresponding to OBC for flow conditions in Morse et al. (2021) are made. Figure 6.6 shows that the prediction made using Equation 6.25 agrees very well with the measured value, hence confirming the postulated mechanism.

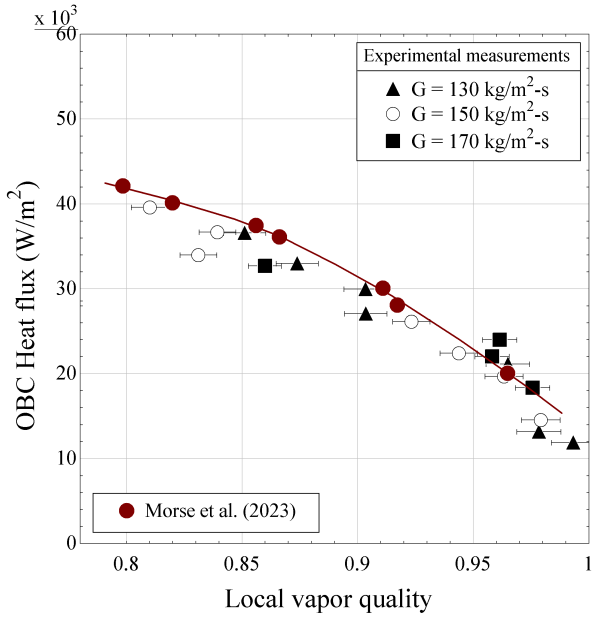

Figure 6.6: The OBC heat flux as a function of local vapor quality (experimental data from Morse et al. (2021)).

For flow conditions in which a significant amount of liquid mass is provided to the base film by way of droplet deposition and/or transport from the waves, terms can be added to

the right-hand side of Equation 6.25 to account for mass transport into the base film. For constant f_{dry}, additional mass transport to the base film will require an increase in local heat flux in order to vaporize the liquid in the base film prior to the arrival of a disturbance wave. Equation 6.25 can also be used to predict the heat flux at CBT given the value of f_{dry} corresponding to the transition to significantly lower HTC. However, further work is required to characterize f_{dry} dry at the CBT.

Chapter 7

Summary

The liquid film in annular two-phase flow has been characterized within a newly defined transitional flow regime between annular flow and mist flow: the intermittent dryout flow regime. Relevant terminologies have been defined or clarified. Mechanistic approaches for predicting heat transfer and the dryout are presented. The heat transfer and dryout models are applicable for two-phase flows in the annular and intermittent dryout flow regimes that occur in conventional-sized channels. Because the model is based on the local characteristics of the liquid film, it can apply generally to a wide variety of configurations. Based on the experimental results, the following conclusions are made, applicable to all mass fluxes investigated in this study:

- The behavior of the liquid film in the intermittent dryout flow regime is characterized by dryout events between disturbance waves and dry time fraction ranging from 0 to 1.
- The dryout event between disturbance waves is observed. The base film is vaporized to a point where it ruptures.
- The rewetting mechanism is also observed. The passage of a disturbance wave will rewet a local dry region.
- The dryout and rewetting mechanisms are observed to occur at different time scales.

- For all mass fluxes investigated in this study, the local HTC reaches a peak when the time-averaged dry fraction is $f_{dry} \approx 0.05$. This point is defined in this work as the optimum boiling conditions (OBC).
- The critical boiling transition (CBT), corresponding to a significant decrease of HTC, can occur for a temporal dry fraction as low as $f_{dry} = 0.1$, far from complete film dryout.
- Using local flow quantities, mechanistic models are formulated for local HTC and dryout heat flux. Predictions for local HTC and OBC are made and agree with experimental results.

This work shows the importance of capturing the liquid-film dynamics for describing two-phase annular flows. There is currently a lack of local, time-resolved liquid film data in the literature, mainly because these measurements are difficult to make in situ. Hopefully, this work will encourage researchers to develop better methods for characterizing the liquid film with high time resolution and associated prediction models.

Bibliography

Abernethy, R. and Thompson, J. (1973). Handbook of uncertainty in gas turbine measurements. *Nat. Tech. Inform. Serv.*

Ahn, H., Lee, C., Kim, H., Jo, H., Kang, S., Kim, J., Shin, J., and Kim, M. H. (2010). Pool boiling CHF enhancement by micro/nanoscale modifications of zircaloy-4 surface. *Nuclear Engineering and Design*, 240(10):3350–3360.

Blasius, P. R. H. (1913). Das aehnlichkeitsgesetz bei reibungsvorgangen in flussigkeiten. *Forschungsheft*, 131:1–141.

Borhani, N., Agostini, B., and Thome, J. R. (2010). A novel time strip flow visualisation technique for investigation of intermittent dewetting and dryout in elongated bubble flow in a microchannel evaporator. *International Journal of Heat and Mass Transfer*, 53:4809–4818.

Borhani, N. and Thome, J. R. (2014). Intermittent dewetting and dryout of annular flows. *International Journal of Multiphase Flow*, 67:144–152.

Chan, J. (2020). Thermoreflectance for the Instantaneous Measurement of Temperature at a Wall-Vapor Interface. Master's thesis, University of Wisconsin - Madison.

Chen, J. (1966). Correlation for boiling heat transfer to saturated fluids in convective flow. *Ind. Eng. Chem. Process Des. Dev.*, 5(3):322–329.

Cherdantsev, A. V., Isaenkov, S. V., Cherdantsev, M. V., and Markovich, D. M. (2021). The

effect of high-frequency oscillations on the disturbance waves in annular flow. *International Journal of Multiphase Flow*, 43(103754).

Chun, J., Lee, W., and Lee, U. (2003). Development of the critical film thickness correlation for an advanced annular film mechanistic dryout model applicable to mars code. *Nuclear Engineering Design*, 223(3):315–328.

Cioncolini, A. and Thome, J. (2012). Entrained liquid fraction prediction in adiabatic and evaporating annular two-phase flow. *Nuclear Engineering and Design*, 243:200–213.

Colebrook, C. (1939). Turbulent flow in pipes, with particular reference to the transition between the smooth and rough pipe laws. *Journal of the Institution of Civil Engineers*, 11(4):133–156.

Collier, J. and Thome, J. R. (1994). *Convective boiling and condensation*. 3rd ed. Oxford: Clarendo Press.

Commission, U. S. N. R. (2016). *Credibility Assessment Framework for Critical Boiling Transition Models*. Number NUREG/KM-0013.

Del Col, D. and Bortolin, S. (2012). Investigation of dryout during flow boiling in a single microchannel under non-uniform axial heat flux. *International Journal of Thermal Sciences*, 57:12–36.

Diani, A., Mancin, S., Balcon, M., Savio, E., and Rossetto, L. (2018). R1234yf flow boiling heat transfer in a rectangular channel heated from the bottom. *Heat Transfer Engineering*, 39(3):198–207.

Dittus, F. and Boelter, L. (1930). Heat transfer in automobile radiators of the tubular type. *Publications in Engineering*, 2:443–461.

Dobran, F. (1983). Hydrodynamic and heat transfer analysis of two-phase annular flow with

a new liquid film model of turbulence. *International Journal of Heat and Mass Transfer*, 26:1159–1171.

Fehring, B., Morse, R., Chan, J., Dressler, K., Hurlburt, E., Nellis, G., and Berson, A. (2020). Instantaneous optical measurement of the temperature at the interface between a wall and a thin liquid film. *Journal of Heat Transfer*, 142(121701).

Galloway, J. and Mudawar, I. (1993). Chf mechanism in flow boiling from a short heated wall - I: Examination of near-wall conditions with the aid of photomicrography and high-speed video imaging. *International Journal of Heat and Mass Transfer*, 36(10):2511–2526.

Gnielinski, V. (1975). *Forsch Ing-Wes*, 41.

Hewitt, G. (1969). Disturbance wave development in annular two-phase flow. *Proc Insn Mech Engrs*, 184c:142–150.

Hurlburt, E. and Newell, T. (1996). Optical measurement of liquid film thickness and wave velocity in liquid film flows. *Experiments in Fluids*, 21:357–362.

Kanizawa, F. T., Tibiriçá, C. B., and Ribatski, G. (2016). Heat transfer during convective boiling inside microchannels. *International Journal of Heat and Mass Transfer*, 93:566–583.

Kim, S. and Mudawar, I. (2013). Universal approach to predicting saturated flow boiling heat transfer in mini/micro-channels (Part I) dryout incipience quality. *International Journal of Heat and Mass Transfer*, 64:1226–1238.

Klein, S. (2019). Engineering equation solver (EES). Academic.

Le Corre, J. (2022). Phenomenological model of disturbance waves in annular two-phase flow. *International Journal of Multiphase Flow*, 151(104057).

Lillo, G., Mastrullo, R., Mauro, A., and Viscito, L. (2019). Flow boiling of R1233zd(e) in a horizontal tube: Experiments, assessment and correlation for asymmetric annular flow. *International Journal of Heat and Mass Transfer*, 129:547–561.

Marathe, S. and Webb, R. L. (2008). Prediction of dryout vapor quality for annular two-phase flow in tubes. *Applied Thermal Engineering*, 28:691–698.

March-Leuba, J. (1992). Density wave instabilities in boiling water reactors. *Oak Ridge National Laboratory. Prepared for the U.S. Nuclear Regulatory Commission.*

Moreira, T. A., Morse, R. W., Dressler, K. M., Ribatski, G., and Berson, A. (2020). Liquid-film thickness and disturbance-wave characterization in a vertical, upward, two-phase annular flow of saturated R245fa inside a rectangular channel. *International Journal of Multiphase Flow*, 132(103412).

Morse, R. W., Chan, J., Dressler, K. M., Hurlburt, E. T., Berson, A., Nellis, G. F., and Le Corre, J. (2023). A new paradigm for the role of disturbance waves on film dryout in annular two-phase flow. *Topical Meeting on Nuclear Reactor Thermal Hydraulics (NURETH-20).*

Morse, R. W., Chan, J., Hurlburt, E. T., Le Corre, J., Berson, A., Nellis, G. F., and Dressler, K. M. (2024). A new paradigm for the role of disturbance waves on film dryout and heat transfer in annular two-phase flow. *International Journal of Heat and Mass Transfer*, 219(124812).

Morse, R. W., Chan, J., Valois, J. J., Moreira, T. A., Dressler, K. M., Hurlburt, E. T., Nellis, G. F., and Berson, A. (2023 (Submitted for publication)). Critical heat flux, liquid-film dryout and disturbance waves in two-phase annular flow with vapor pulse injections. *Experimental Thermal and Fluid Science.*

Morse, R. W., Moreira, T. A., Chan, J., Dressler, K. M., Ribatski, G., Hurlburt, E. T., McCarrol, L. L., Nellis, G. F., and Berson, A. (2021). Critical heat flux and the dryout of

liquid film in two-phase annular flow. *International Journal of Heat and Mass Transfer*, 177(121487).

Nascimento, F. J., Moreira, T. A., and Ribatski, G. (2019). Flow boiling critical heat flux of DI-water and nanofluids inside smooth and nanoporous round microchannels. *International Journal of Heat and Mass Transfer*, 139:240–253.

National Instruments (2019). Software. LabView.

Nellis, G. and Klein, S. (2009). *Heat Transfer*. Cambridge University Press.

Ong, C. and Thome, J. (2011a). Macro-to-microchannel transition in two-phase flow: Part 1 two-phase flow patterns and film thickness measurements. *Experimental Thermal and Fluid Science*, 35:37–47.

Ong, C. and Thome, J. (2011b). Macro-to-microchannel transition in two-phase flow: Part 2 flow boiling heat transfer and critical heat flux. *Experimental Thermal and Fluid Science*, 35:873–886.

Ozawa, M., Umekawa, H., Yoshioka, Y., and Tomiyama, A. (1993). Dryout under oscillatory flow condition in vertical and horizontal tubes - experiments at low velocity and pressure conditions. *International Journal of Heat and Mass Transfer*, 36(16):4076–4078.

Petukhov, B. (1970). Heat transfer and friction in turbulent pipe flow with variable physical properties. *Advances in heat transfer*, 6c:503–564.

Polhausen, E. (1921). Der Wärmeaustausch zwischen festen Körpern und Flüssigkeiten mit kleiner reibung und kleiner Wormeleitung. *Zeitschrift für Angewandte Mathematik und Mechanik*, 1(2):115–121.

Pope, S. B. (2000). *Turbulent flows*. Cambridge University Press.

Revellin, R., Haberschill, P., Bonjour, J., and Thome, J. R. (2008). Conditions of liquid film dryout during saturated flow boiling in microchannels. *Chemical Engineering Science*, 63:5795–5801.

Richenderfer, A., Kossolapov, A., Seong, J. H., Saccone, G., Demarly, E., Kommajosyula, R., Baglietto, E., Buongiorno, J., and Bucci, M. (2018). Investigation of subcooled flow boiling and chf using high-resolution diagnostics. *Experimental Thermal and Fluid Science*, 99:35–58.

Rodarte, M. A. (2015). *Liquid Film and Droplet Behavior in Adiabatic and Diabatic Vertical Annular Flow*. PhD thesis, University of Wisconsin - Madison.

Schubring, D., Shedd, T., and Hurlburt, E. (2010). Studying disturbance waves in vertical annular flow with high-speed video. *International Journal of Multiphase Flow*, 36:385–396.

Shah, M. M. (1987). Improved general correlation for critical heat flux during upflow in uniformly heated vertical tubes. *International Journal of Heat and Fluid Flow*, 8(4):326–335.

Shedd, T. and Newell, T. (1998). Automated optical liquid film thickness measurement method. *The American Institute of Physics - Review of Scientific Instruments*, 69.

Su, G., Moreira, T., Lee, D., Jena, A., Wang, G., Byers, A., Phillips, B., Karoutas, Z., Anderson, M., and Bucci, M. (2022). Wettability and chf limits of accident-tolerant nuclear fuel cladding materials in light water reactor conditions. *Applied Thermal Engineering*, 119018:685–698.

Taylor, B. and Kuyatt, C. (1994). Guidelines for evaluating and expressing the uncertainty of NIST measurement results. *NIST Technical note 1927: Edinton, Gaithersburg, 1994*.

Tibiriçá, C. B., Ribatski, G., and Thome, J. R. (2012). Saturated flow boiling heat transfer and critical heat flux in small horizontal flattened tubes. *International Journal of Heat and Mass Transfer*, 55(25-26):7873–7883.

Wojtan, L., Revellin, R., and Thome, J. R. (2006). Investigation of saturated critical heat flux in a single uniformly heated microchannel. *Experimental Thermal and Fluid Science*, 20:765–774.

Wojtan, L., Ursenbacher, T., and Thome, J. R. (2005). Investigation of flow boiling in horizontal tubes: Part 1 a new diabatic two-phase flow pattern map. *International Journal of Heat and Mass Transfer*, 48:2955–2969.

Yadigaroglu, G. and Bergles, A. E. (1972). Fundamental and higher-mode density-wave oscillations in two-phase flow. *Journal of Heat Transfer*, pages 189 – 195.

Zhang, B., Kim, K., and Yoon, H. (2012). Enhanced heat transfer performance of alumina sponge-like nano-porous structures through surface wettability control in nucleate pool boiling. *International Journal of Heat and Mass Transfer*, 55(25-26):7487–7498.

Zhao, T., Markides, C. N., Matar, O. K., and Hewitt, G. (2013). Disturbance wave development in two-phase gas-liquid upwards vertical annular flow. *International Journal of Multiphase Flow*, 55:111–129.

Time series of flow conditions

.1 Mass flux $G = 130$ kg/m^2-s

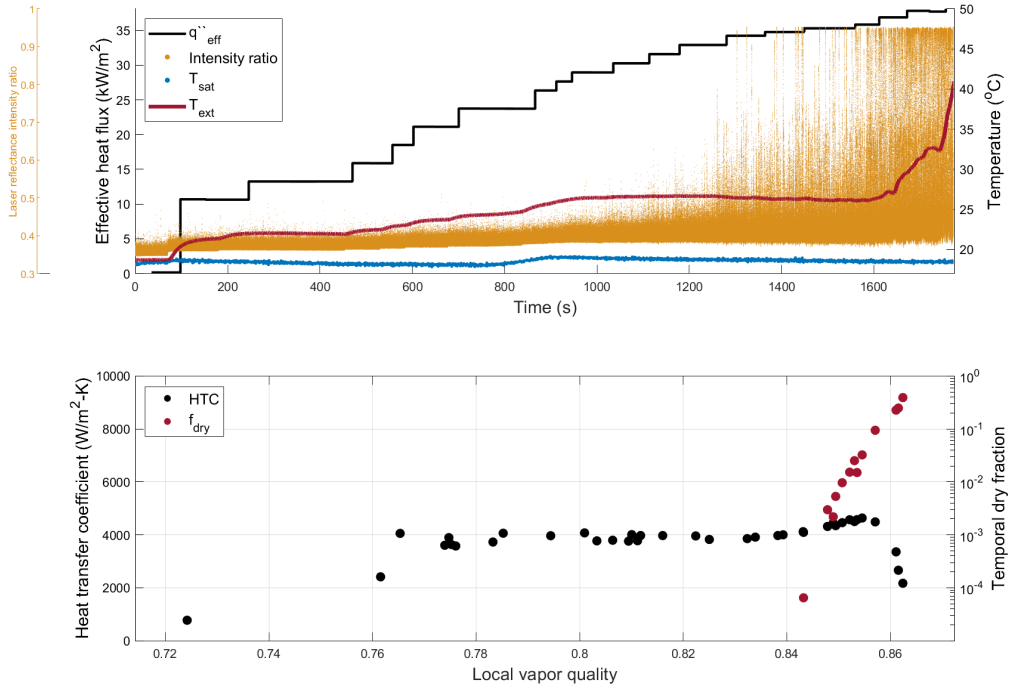

Figure 1: $G = 128$ kg-m^2-s , $x_{in} = 0.72$

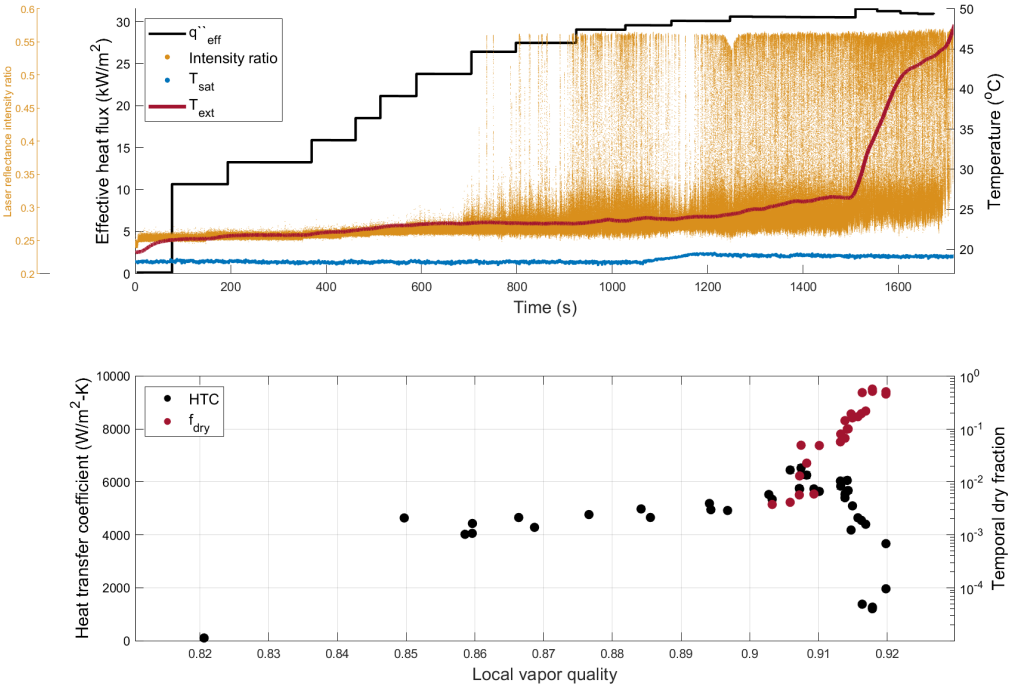

Figure 2: $G = 128$ kg-m^2-s , $x_{in} = 0.81$

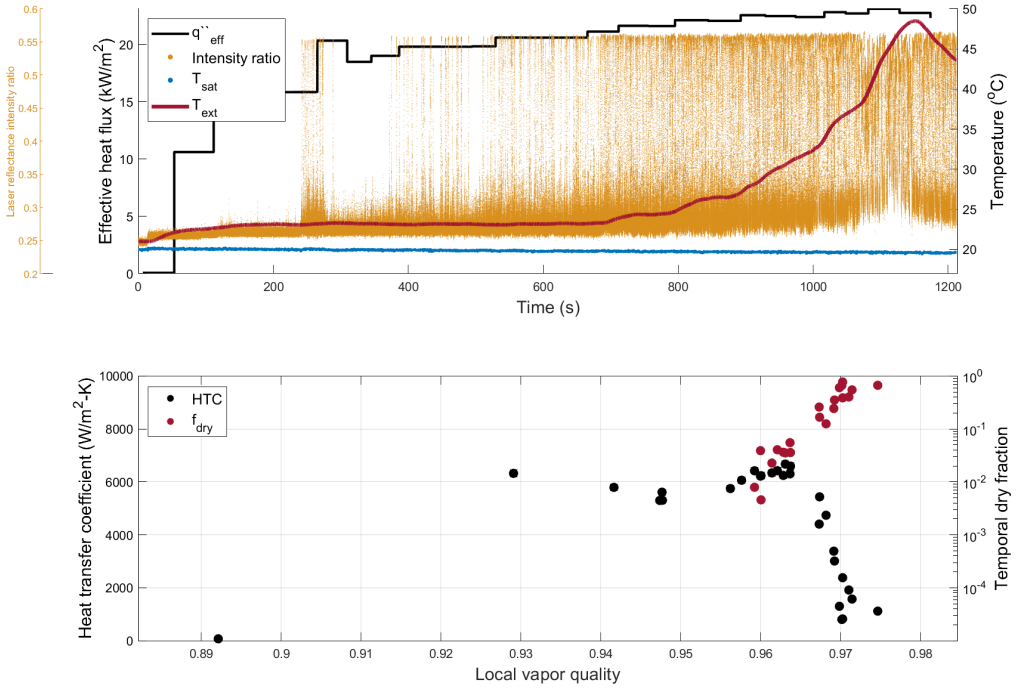

Figure 3: $G = 128$ kg-m^2-s , $x_{in} = 0.89$

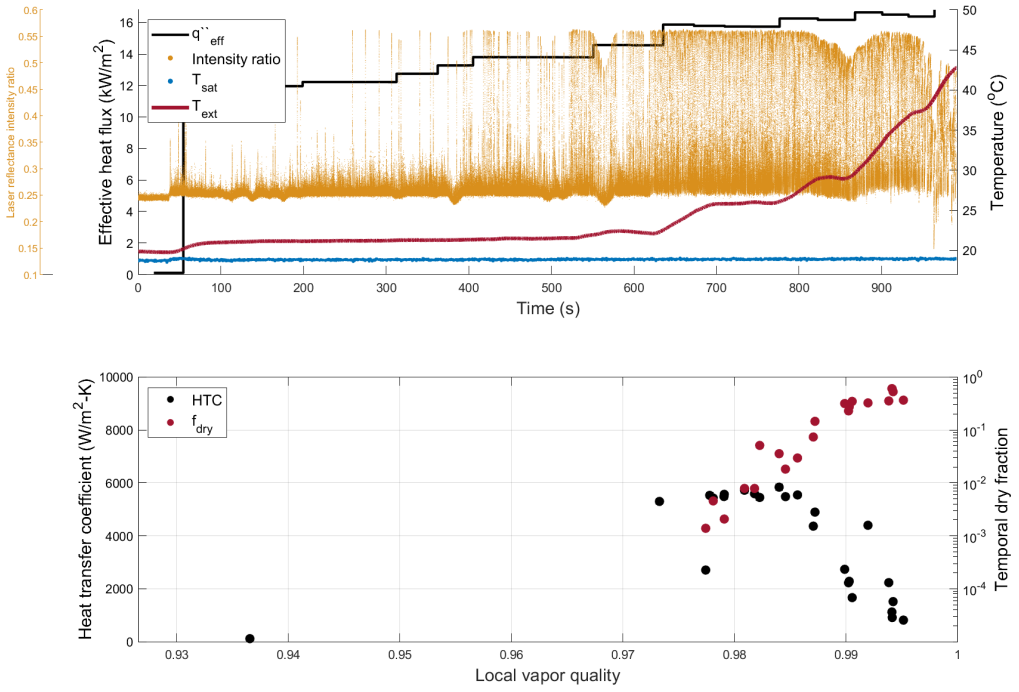

Figure 4: $G = 128$ kg-m^2-s , $x_{in} = 0.93$

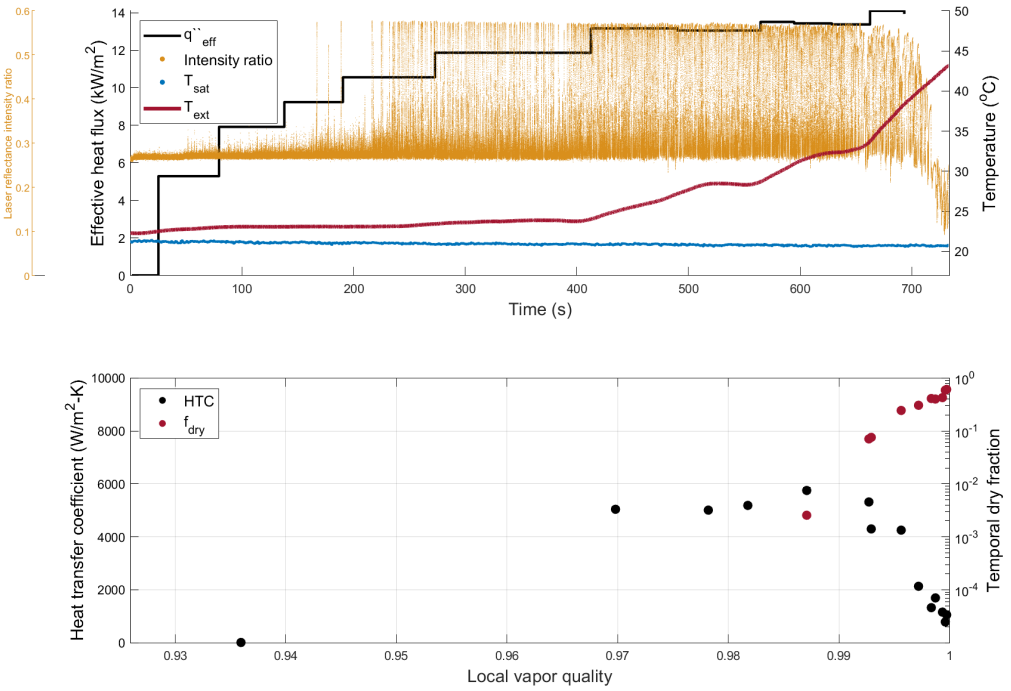

Figure 5: $G = 130$ kg-m^2-s , $x_{in} = 0.95$

.2 Mass flux $G = 140$ kg/m^2-s

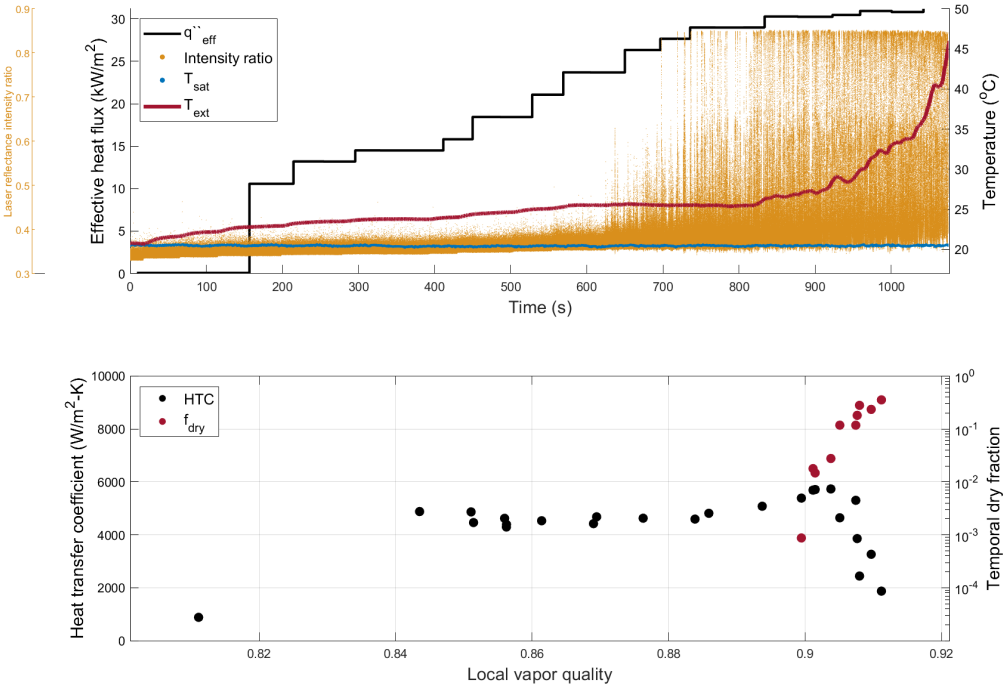

Figure 6: $G = 140$ kg-m^2-s , $x_{in} = 0.81$

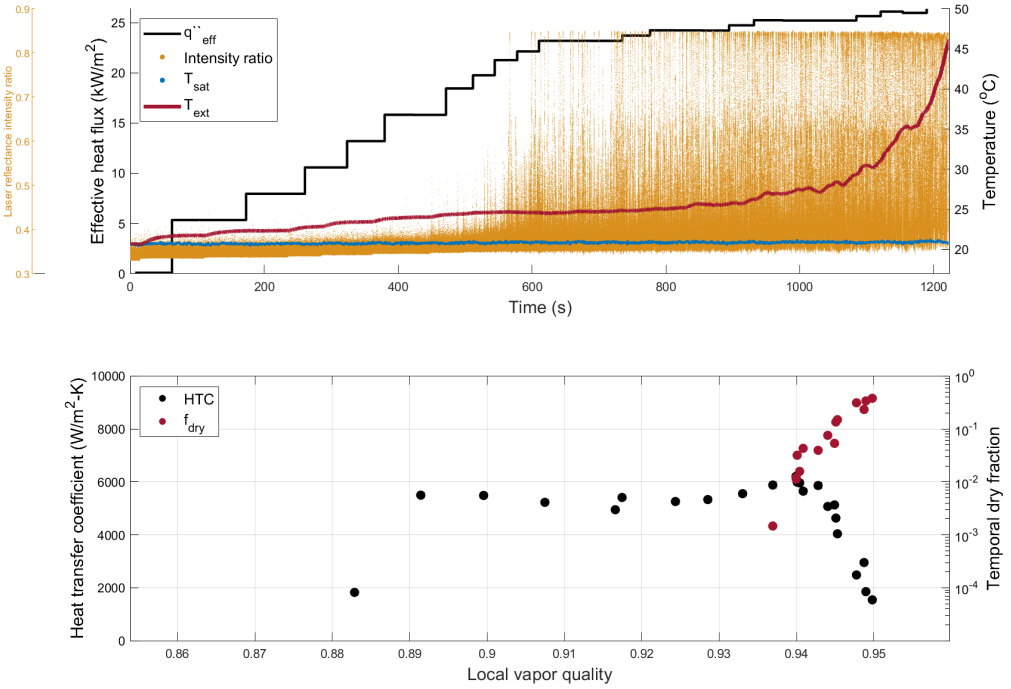

Figure 7: $G = 140$ kg-m^2-s , $x_{in} = 0.86$

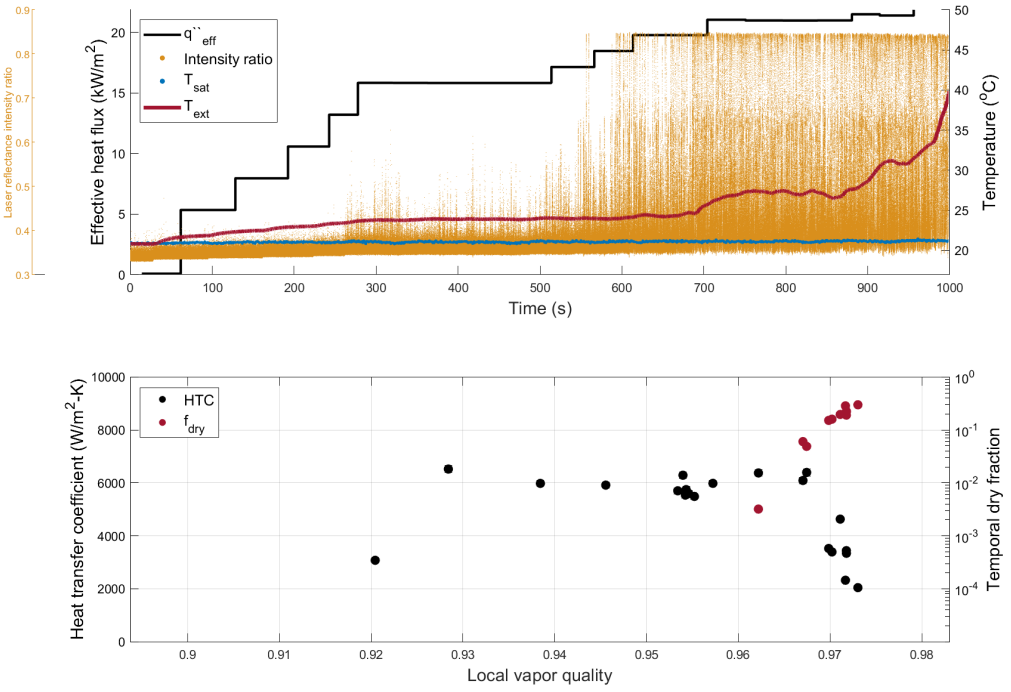

Figure 8: $G = 140$ kg-m^2-s , $x_{in} = 0.90$

.3 Mass flux $G = 150$ kg/m^2-s

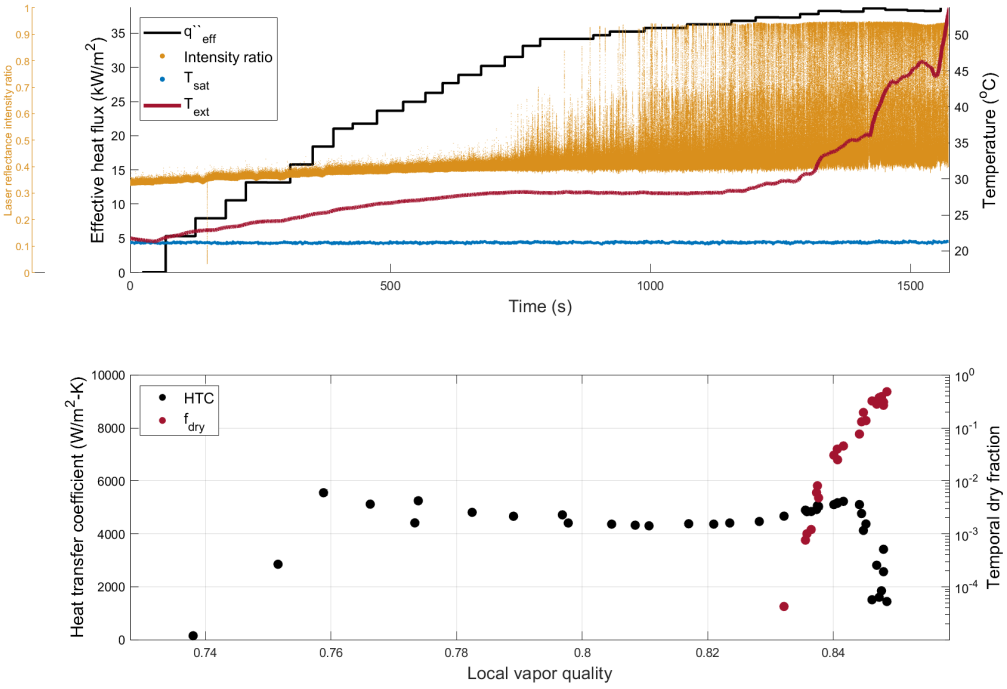

Figure 9: $G = 149$ kg-m^2-s , $x_{in} = 0.73$

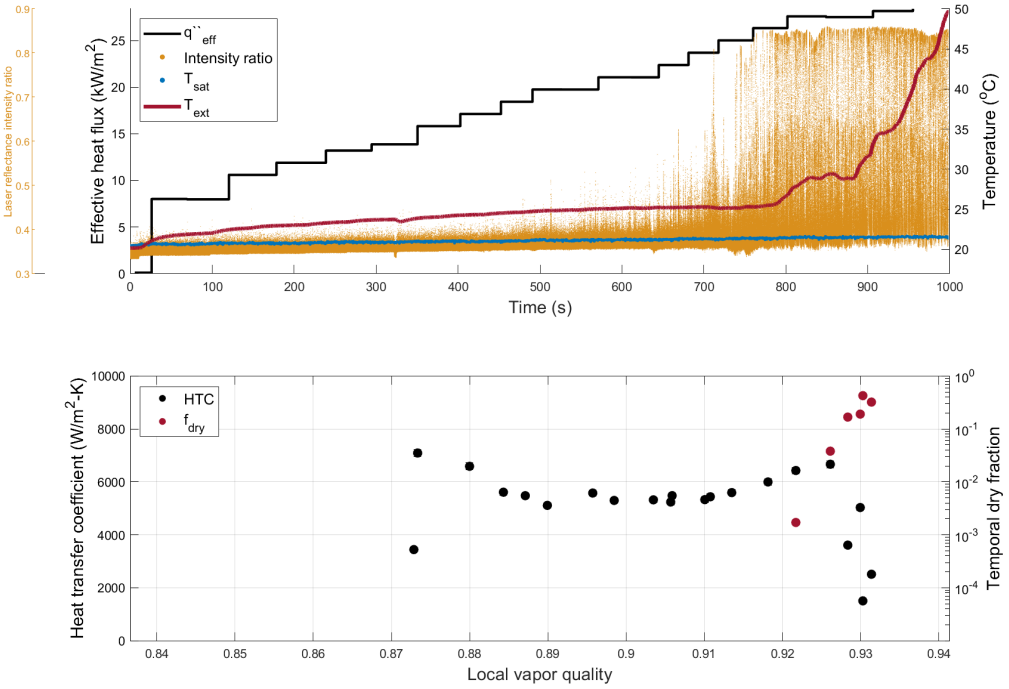

Figure 10: $G = 149$ kg-m^2-s , $x_{in} = 0.84$

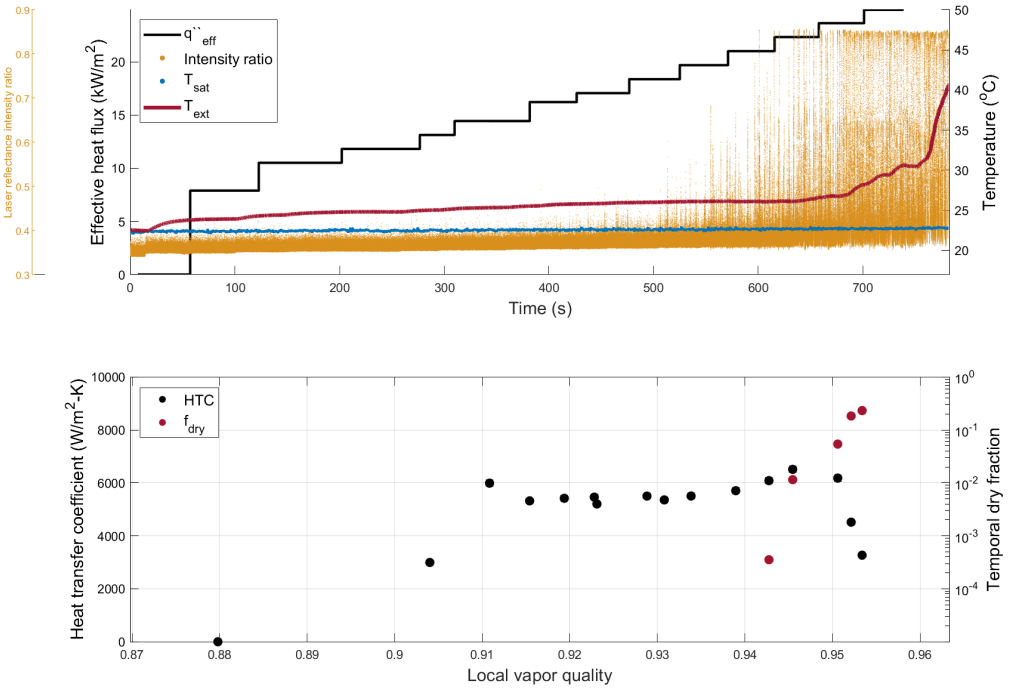

Figure 11: $G = 149$ kg-m^2-s , $x_{in} = 0.88$

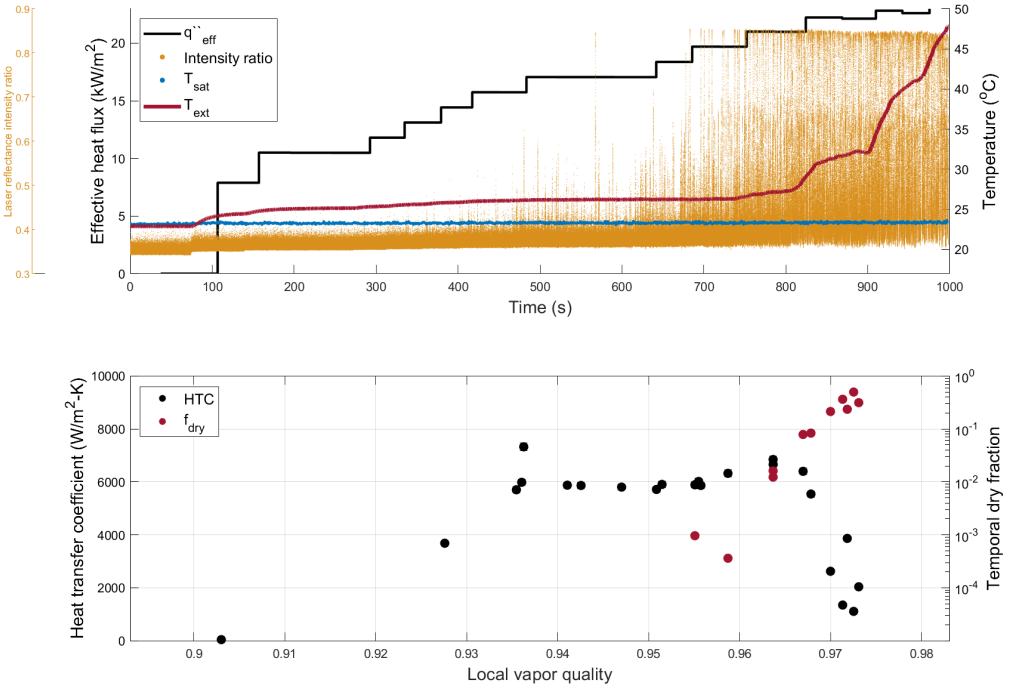

Figure 12: $G = 149$ kg-m^2-s , $x_{in} = 0.90$

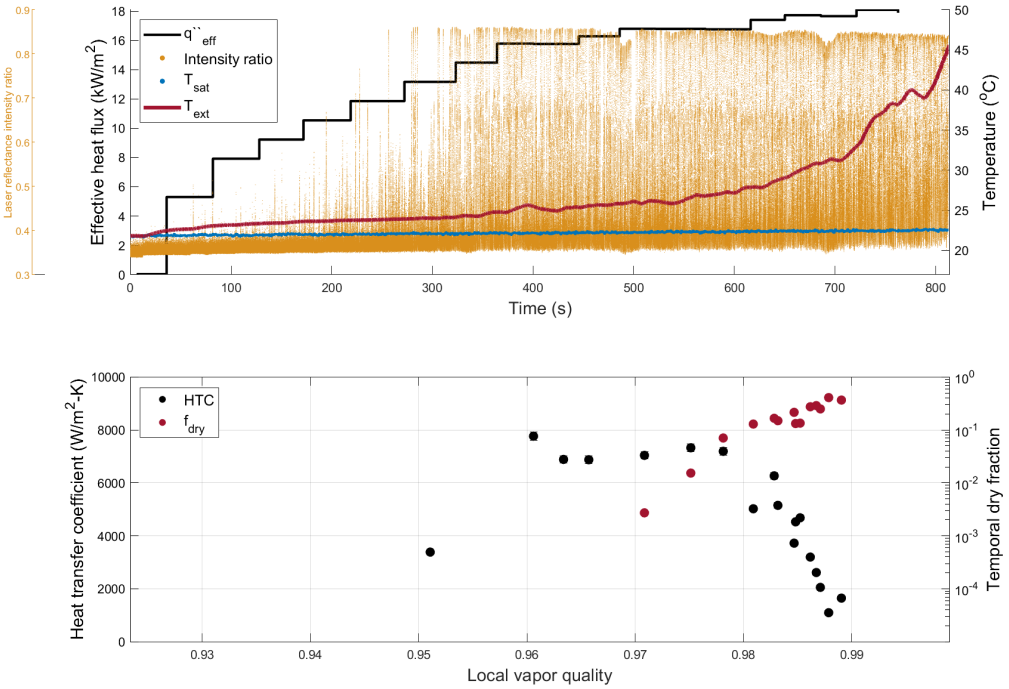

Figure 13: $G = 149$ kg-m^2-s , $x_{in} = 0.93$

.4 Mass flux $G = 167$ kg/m^2-s

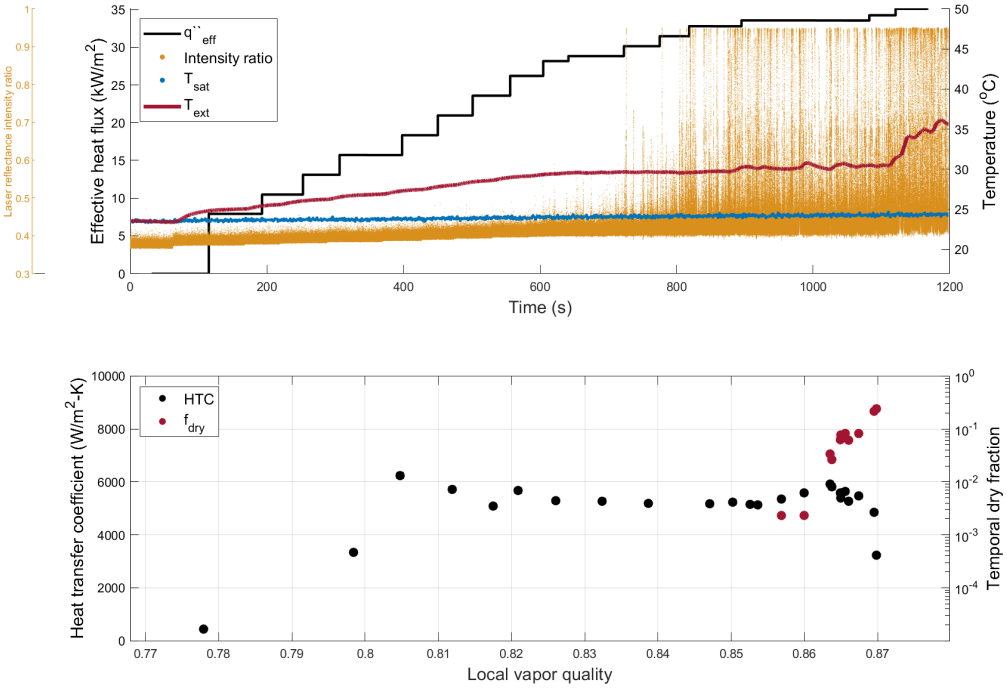

Figure 14: $G = 167$ kg-m^2-s , $x_{in} = 0.77$

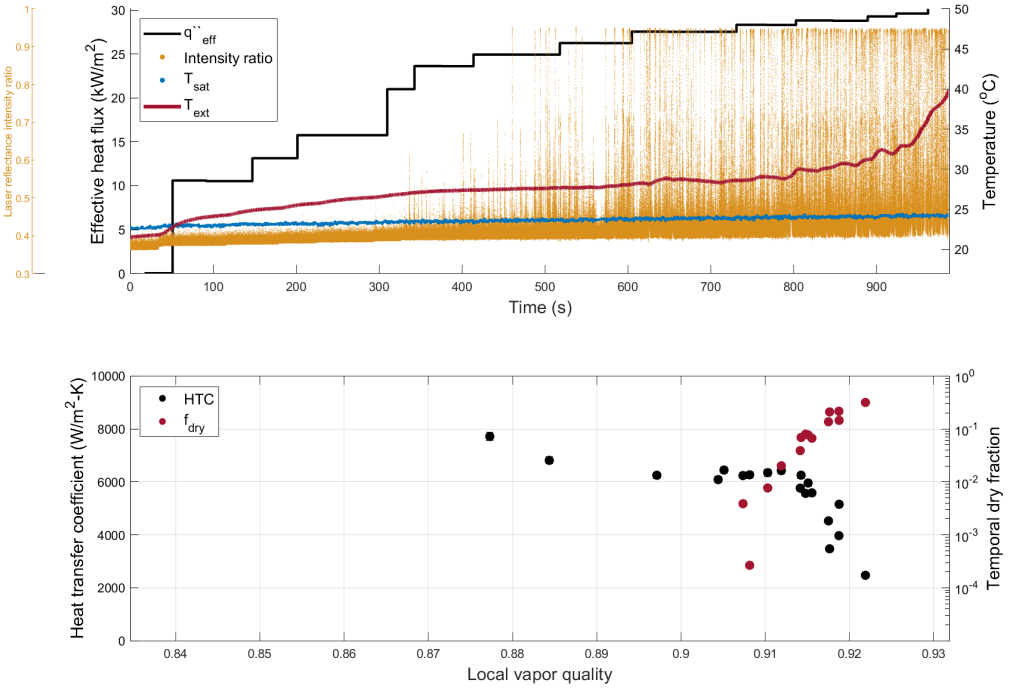

Figure 15: $G = 167$ kg-m^2-s , $x_{in} = 0.84$

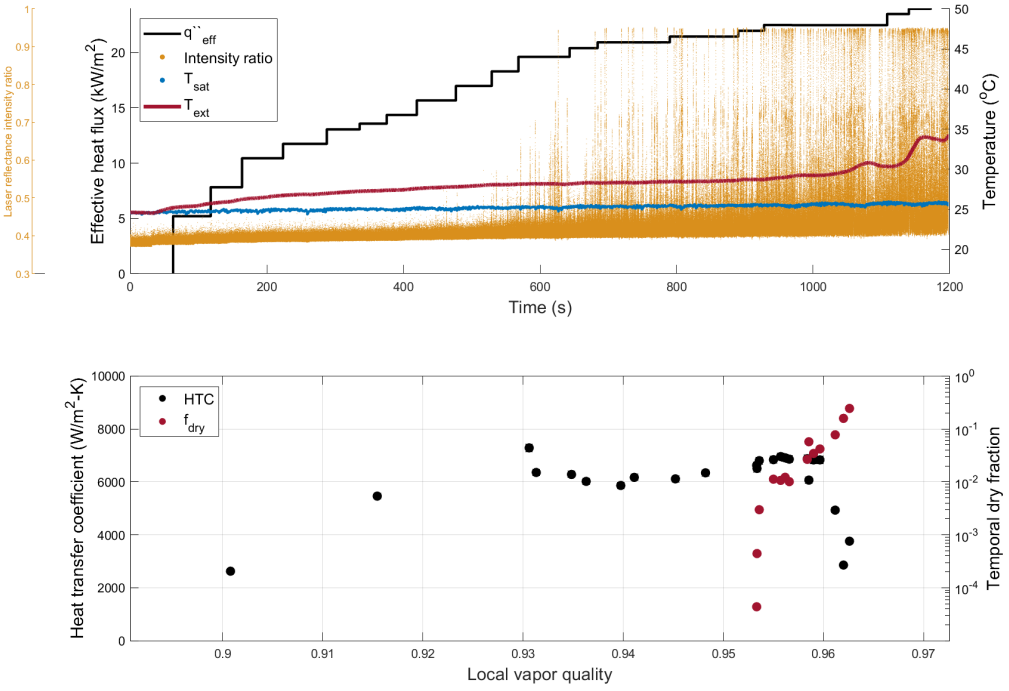

Figure 16: $G = 167$ kg-m^2-s , $x_{in} = 0.90$

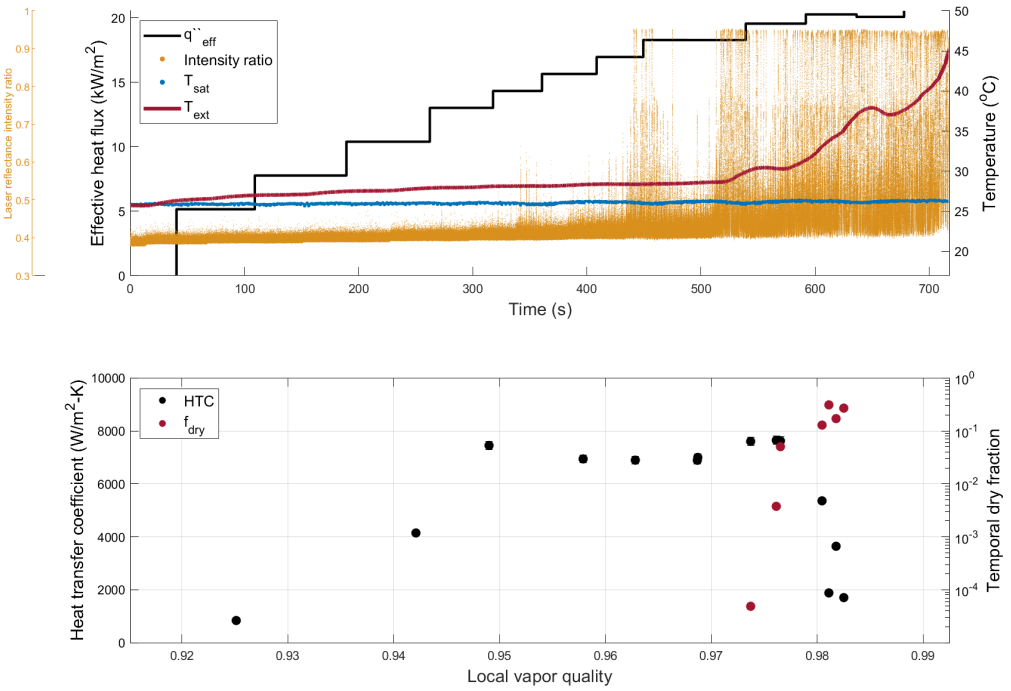

Figure 17: $G = 167$ kg-m^2-s , $x_{in} = 0.92$

Film thickness steady flow

.5 Mass flux $G = 130$ kg/m^2-s

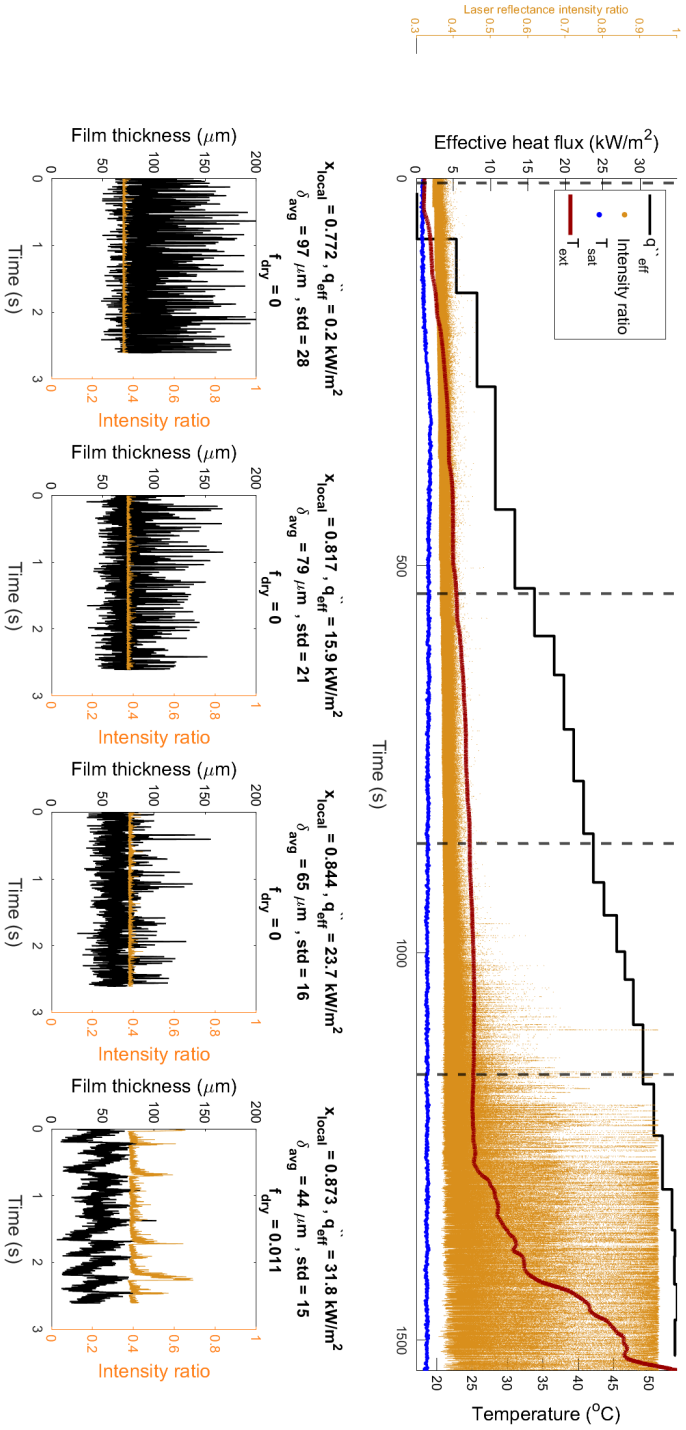

Figure 18: $G = 129$ kg-m^2-s , $x_{in} = 0.772$

.6 Mass flux $G = 150$ kg/m^2-s

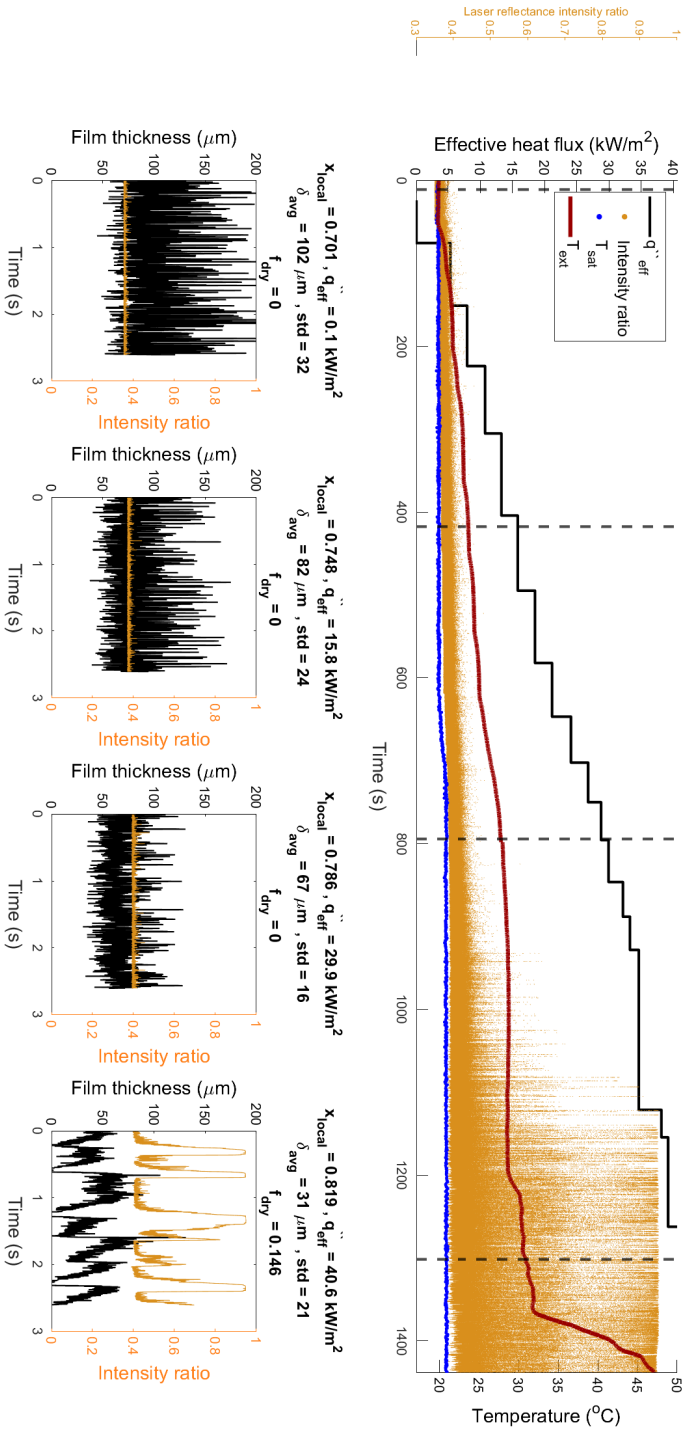

Figure 19: $G = 149$ kg-m^2-s , $x_{in} = 0.694$

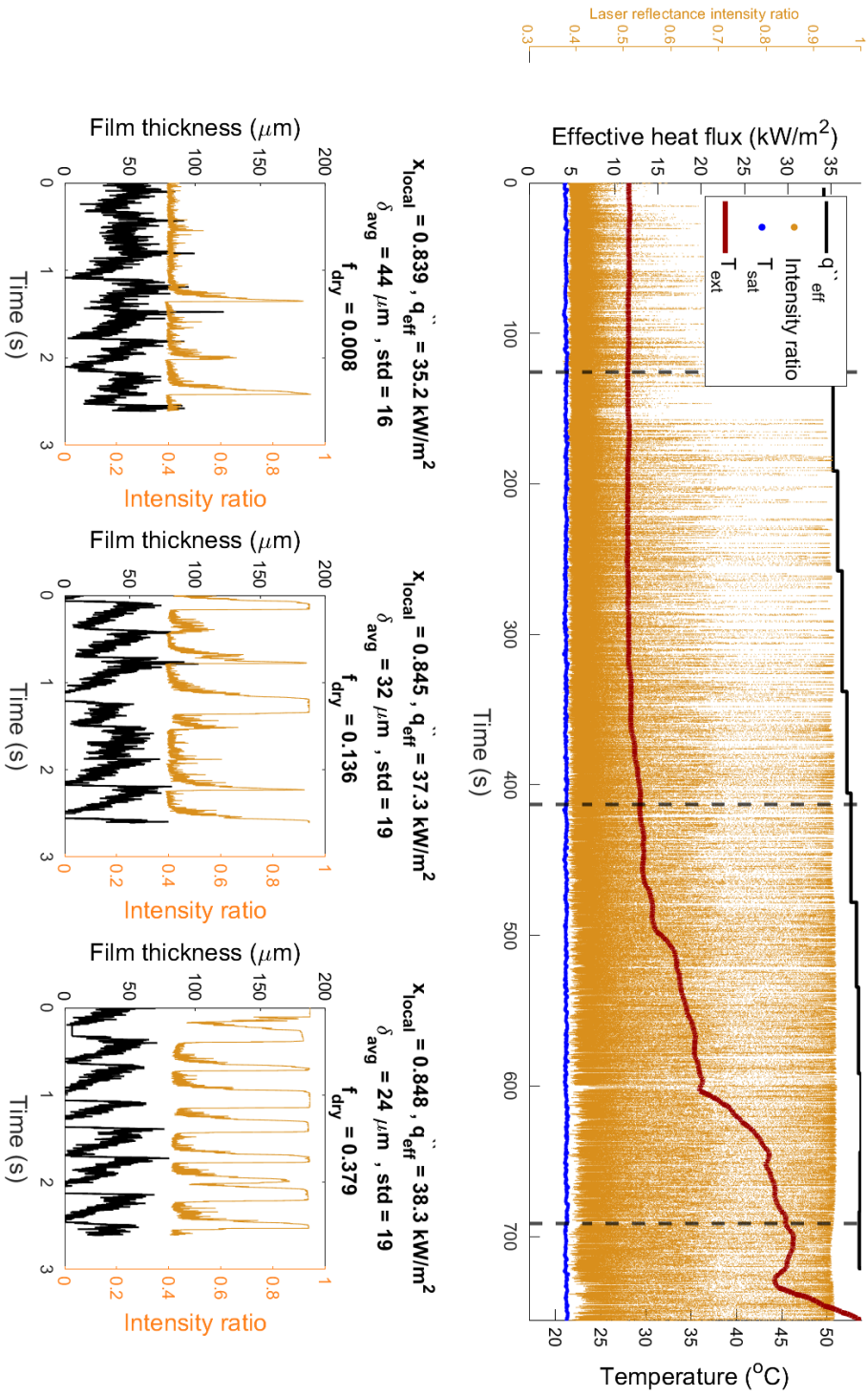

Figure 20: $G = 149$ kg-m^2-s , $x_{in} = 0.728$

.7 Mass flux $G = 167$ kg/m^2-s

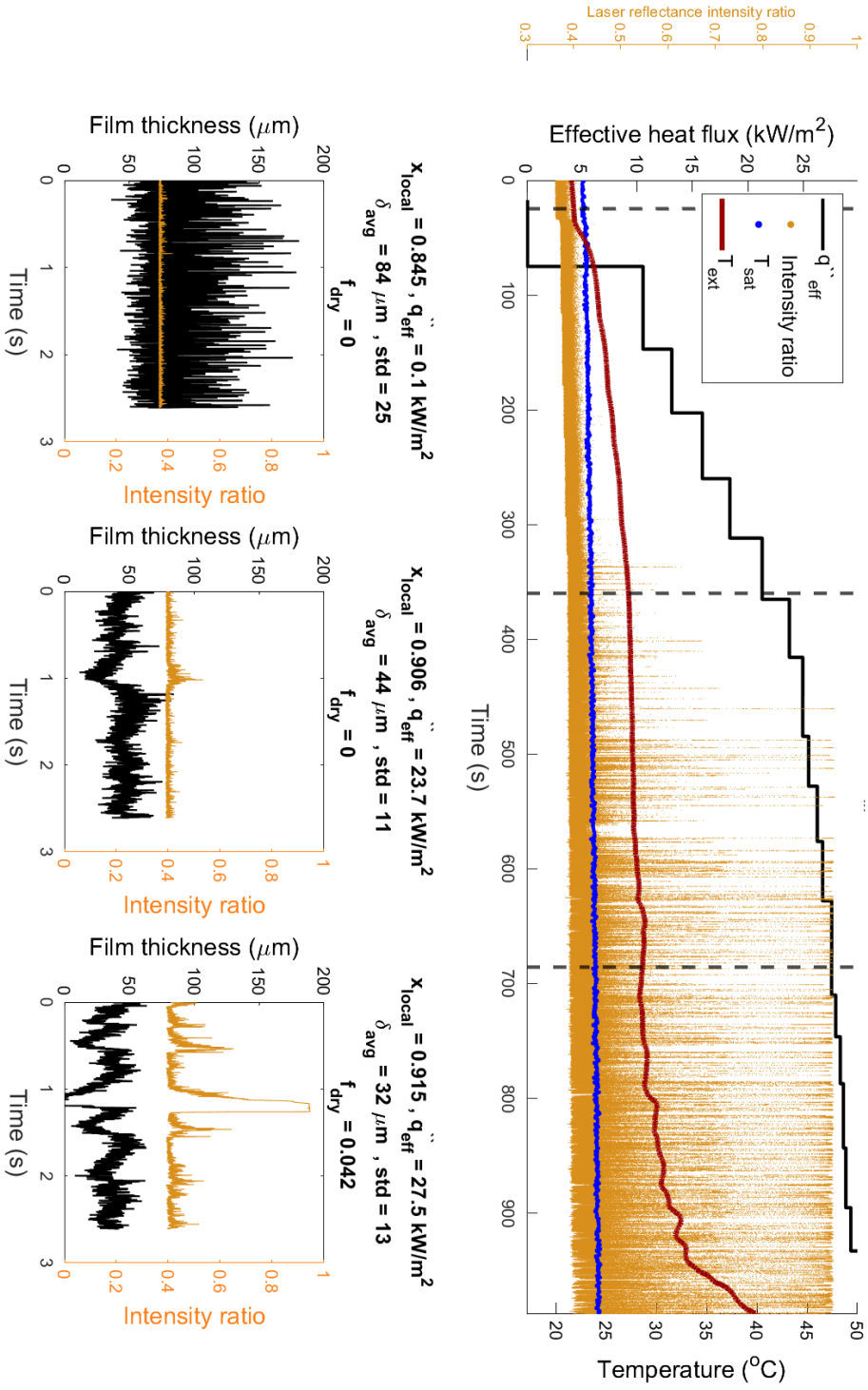

Figure 21: $G = 167$ kg-m^2-s , $x_{in} = 0.84$

Individual data sets

.8 0.5 Hz pulses

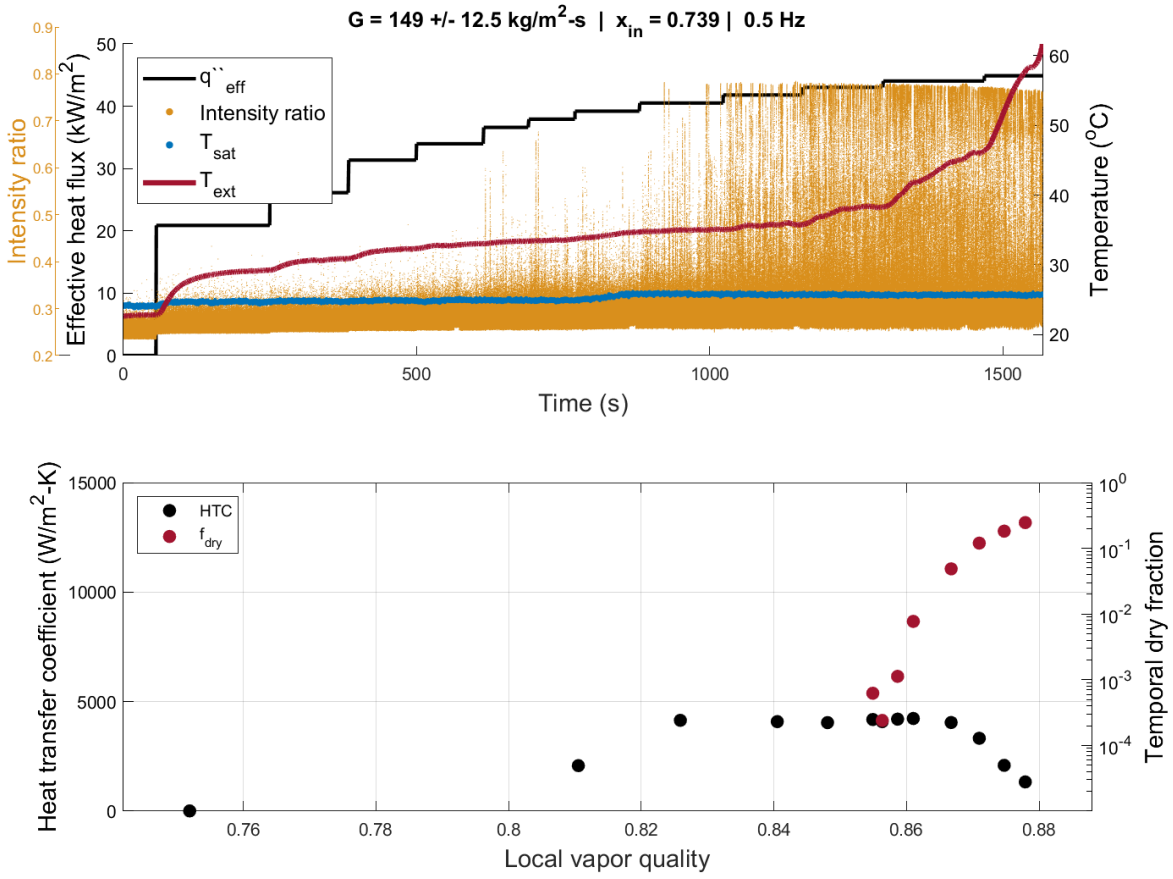

Figure 22: Time trace (top), and time-averaged HTC and f_{dry} as a function of x.

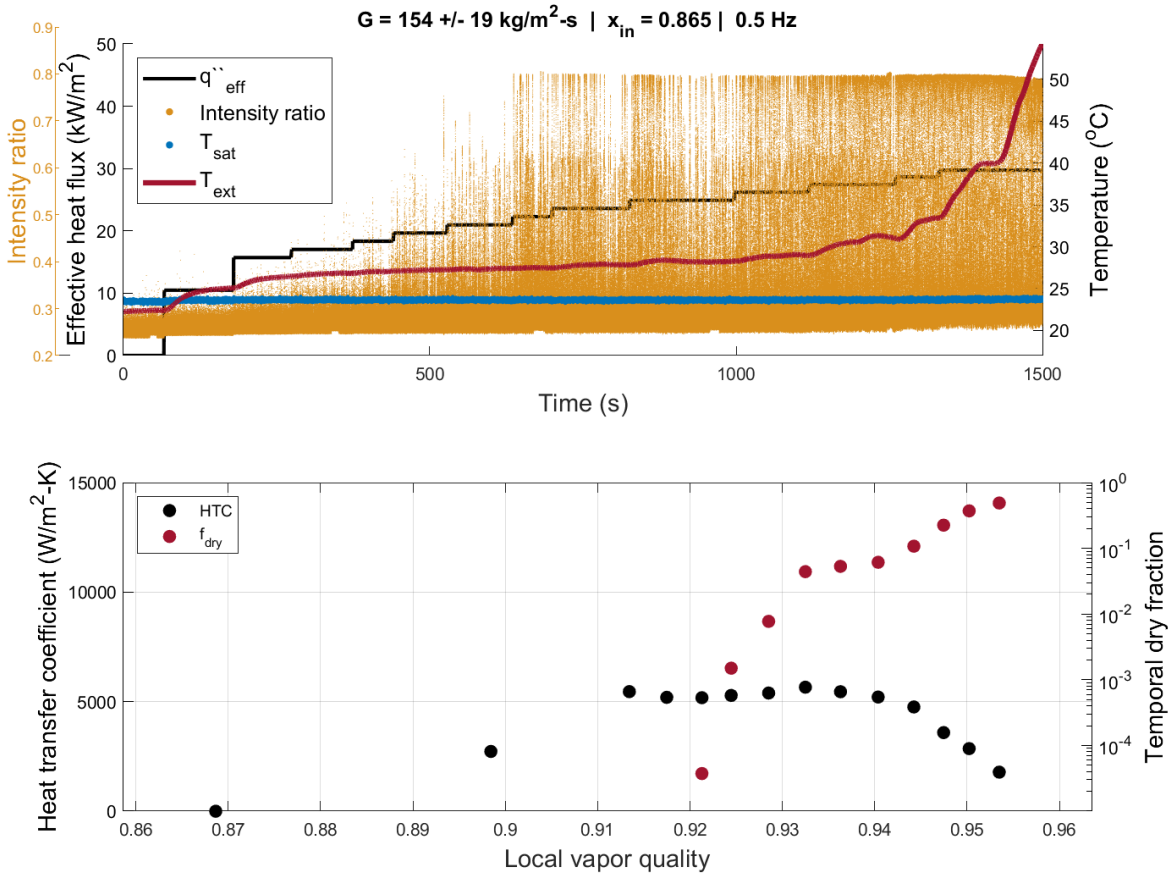

Figure 23: Time trace (top), and time-averaged HTC and f_{dry} as a function of x.

.9 1 Hz pulses

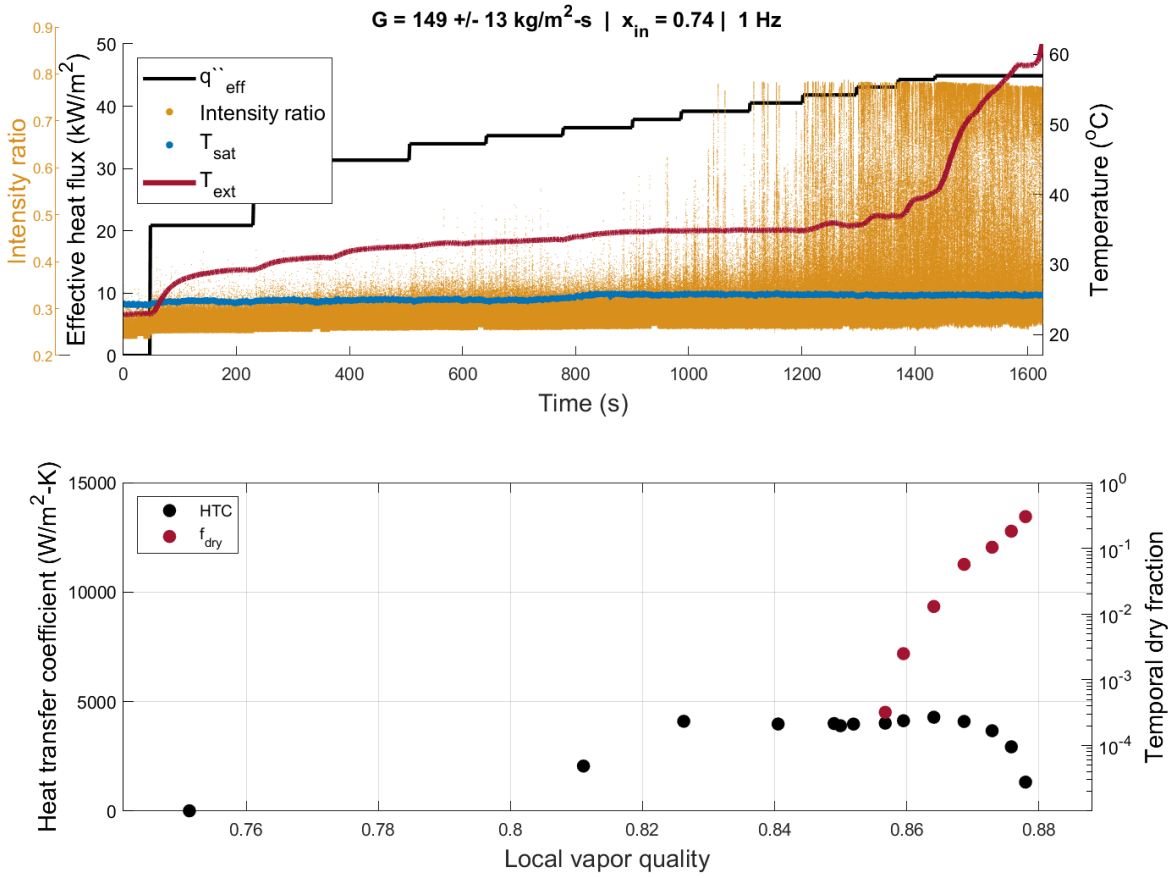

Figure 24: Time trace (top), and time-averaged HTC and f_{dry} as a function of x.

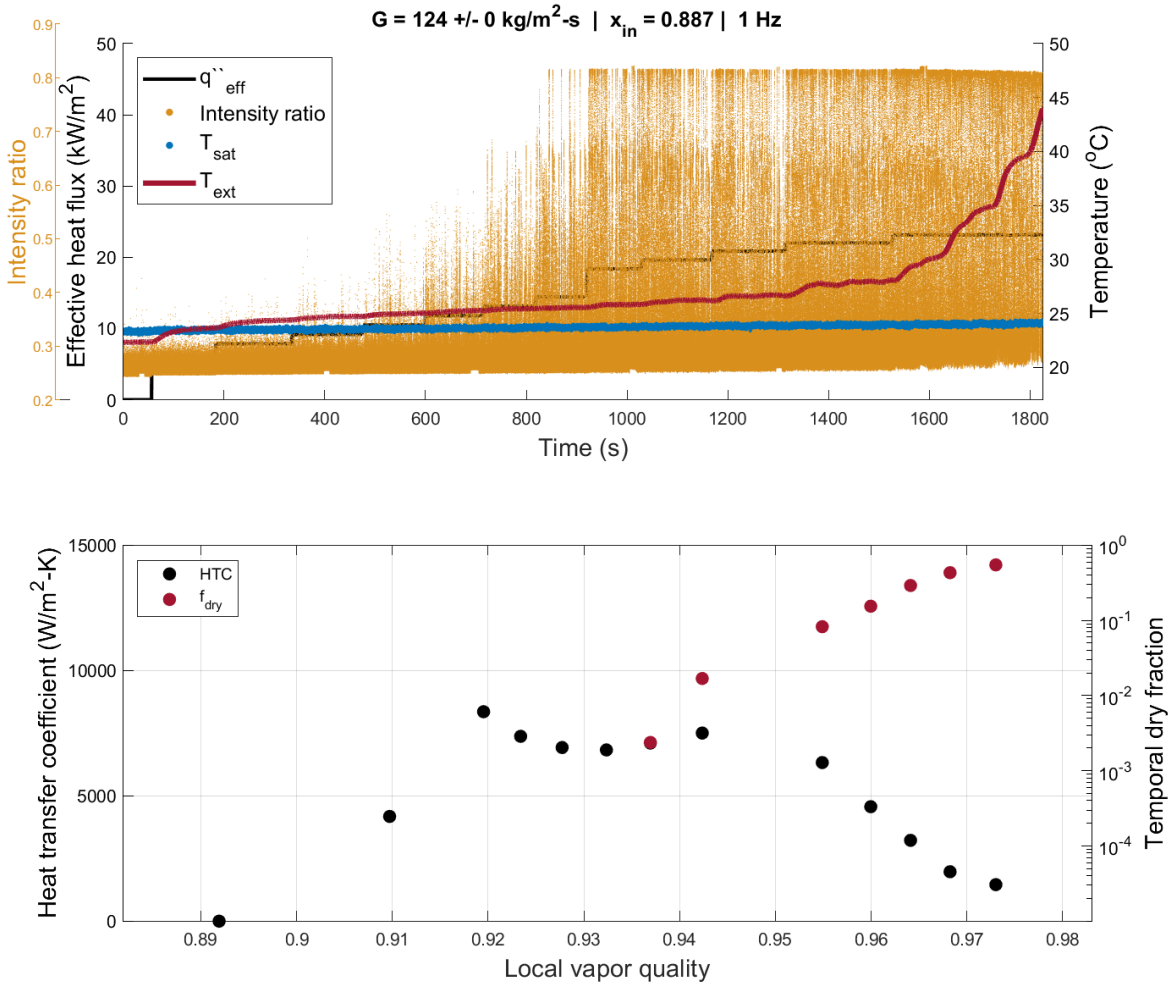

Figure 25: Time trace (top), and time-averaged HTC and f_{dry} as a function of x.

.10 2 Hz pulses

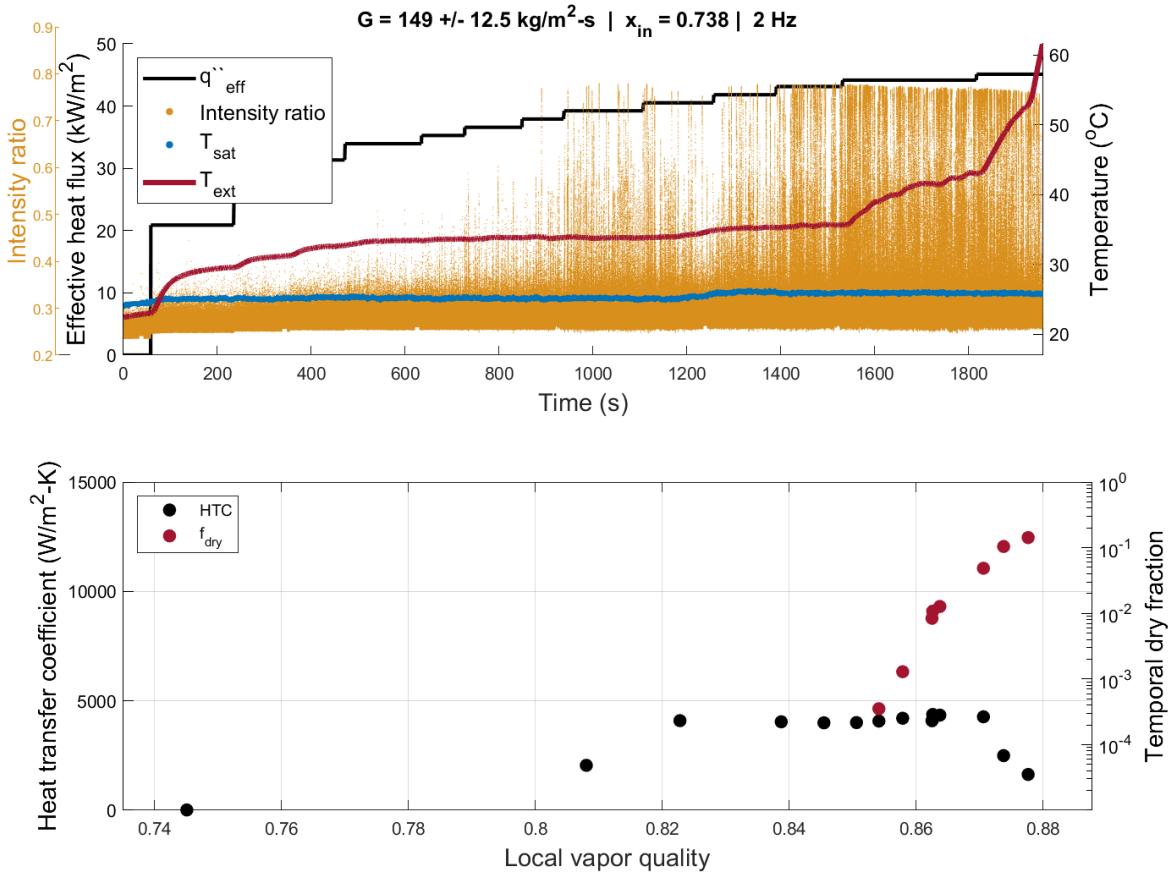

Figure 26: Time trace (top), and time-averaged HTC and f_{dry} as a function of x.

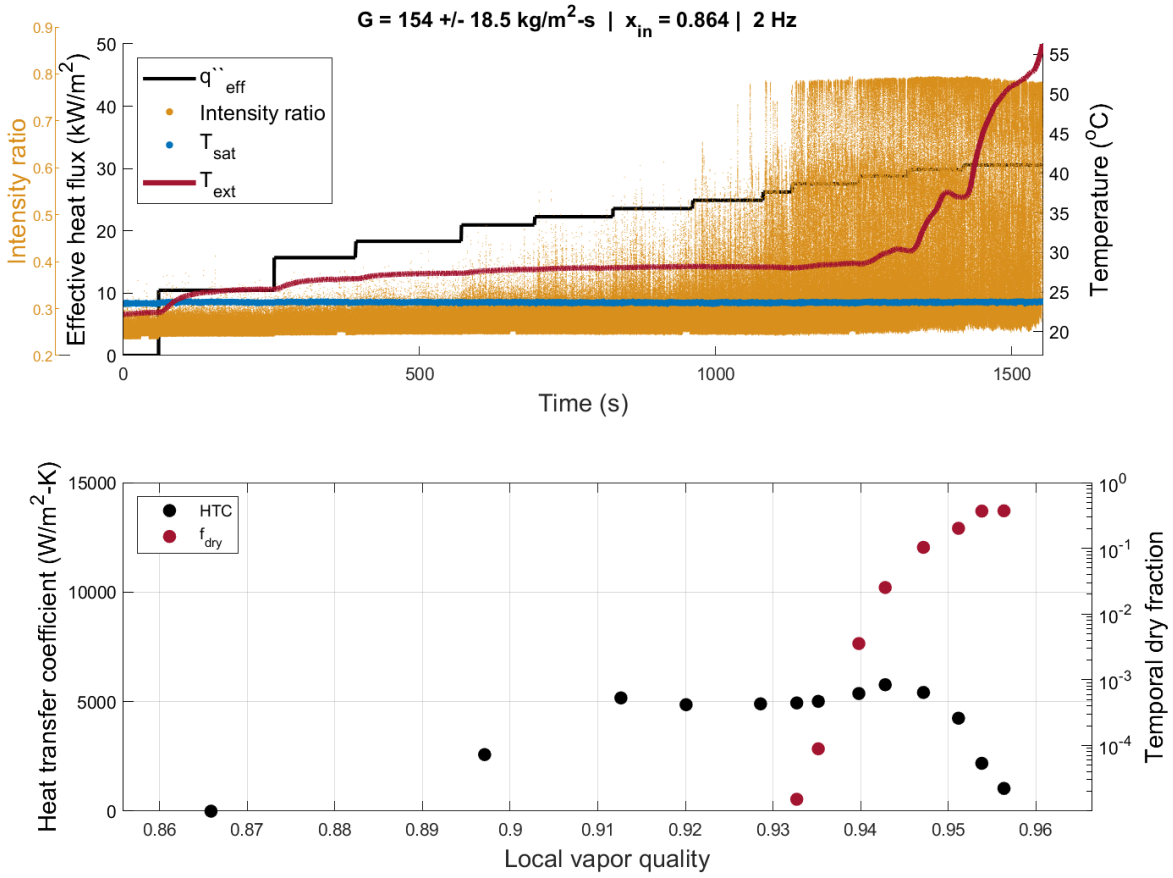

Figure 27: Time trace (top), and time-averaged HTC and f_{dry} as a function of x.

.11 3 Hz pulses

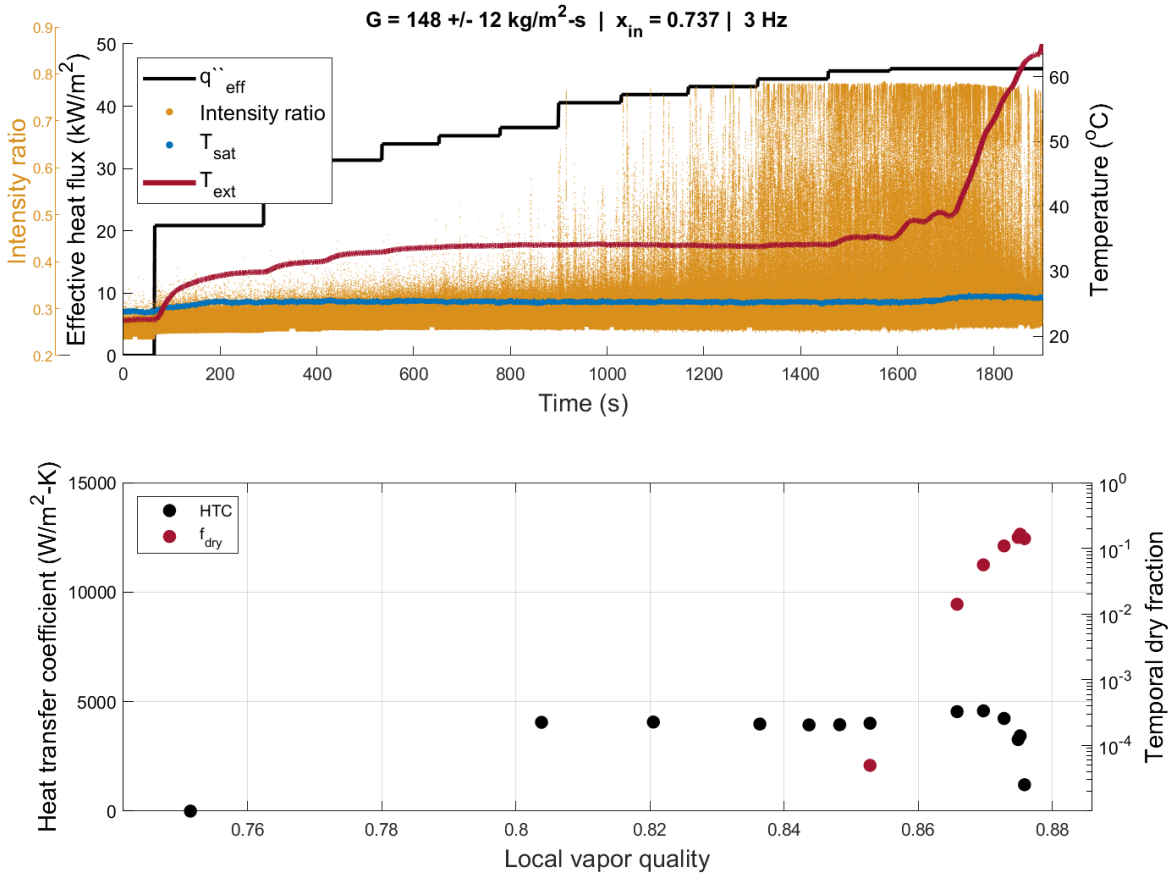

Figure 28: Time trace (top), and time-averaged HTC and f_{dry} as a function of x.

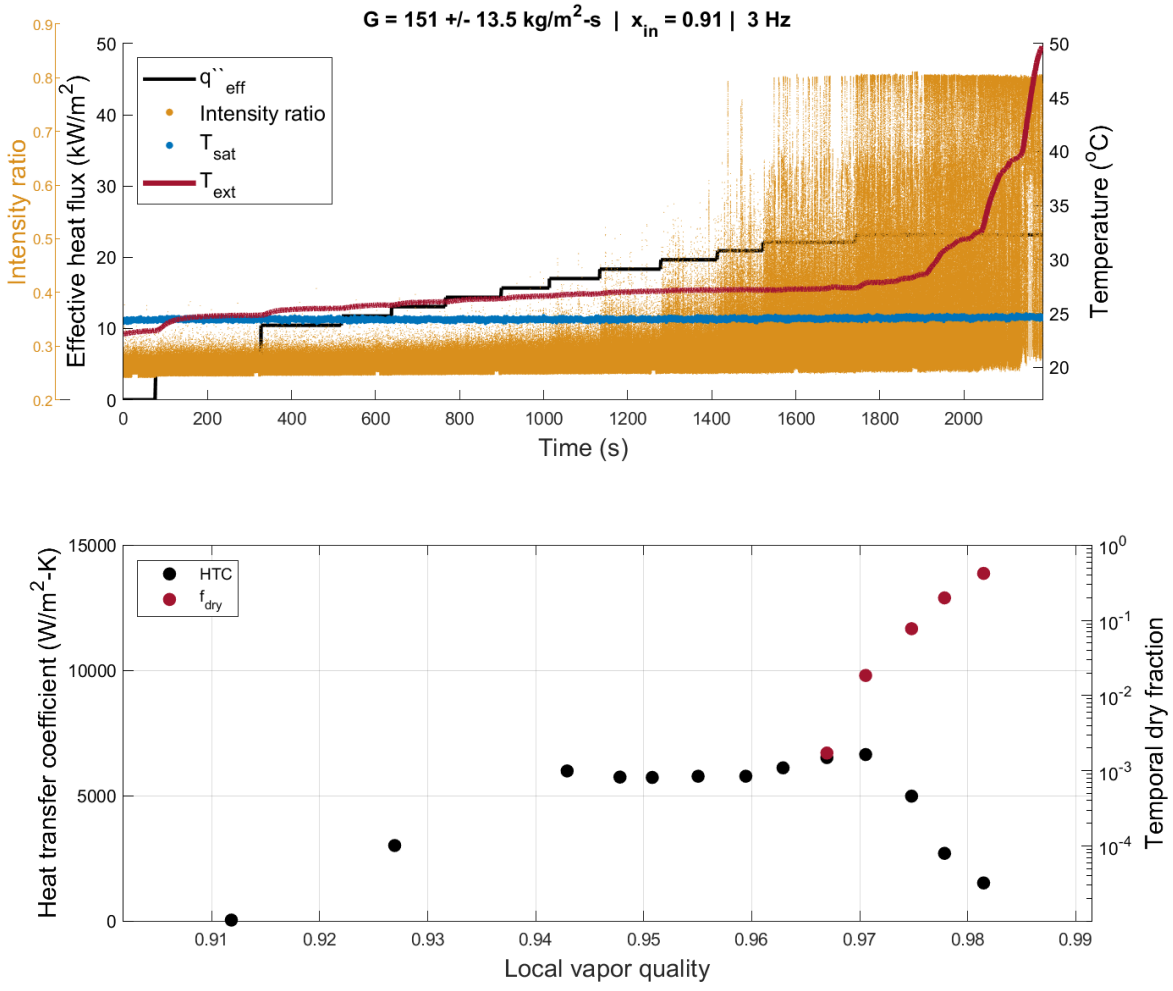

Figure 29: Time trace (top), and time-averaged HTC and f_{dry} as a function of x.

.12 4 Hz pulses

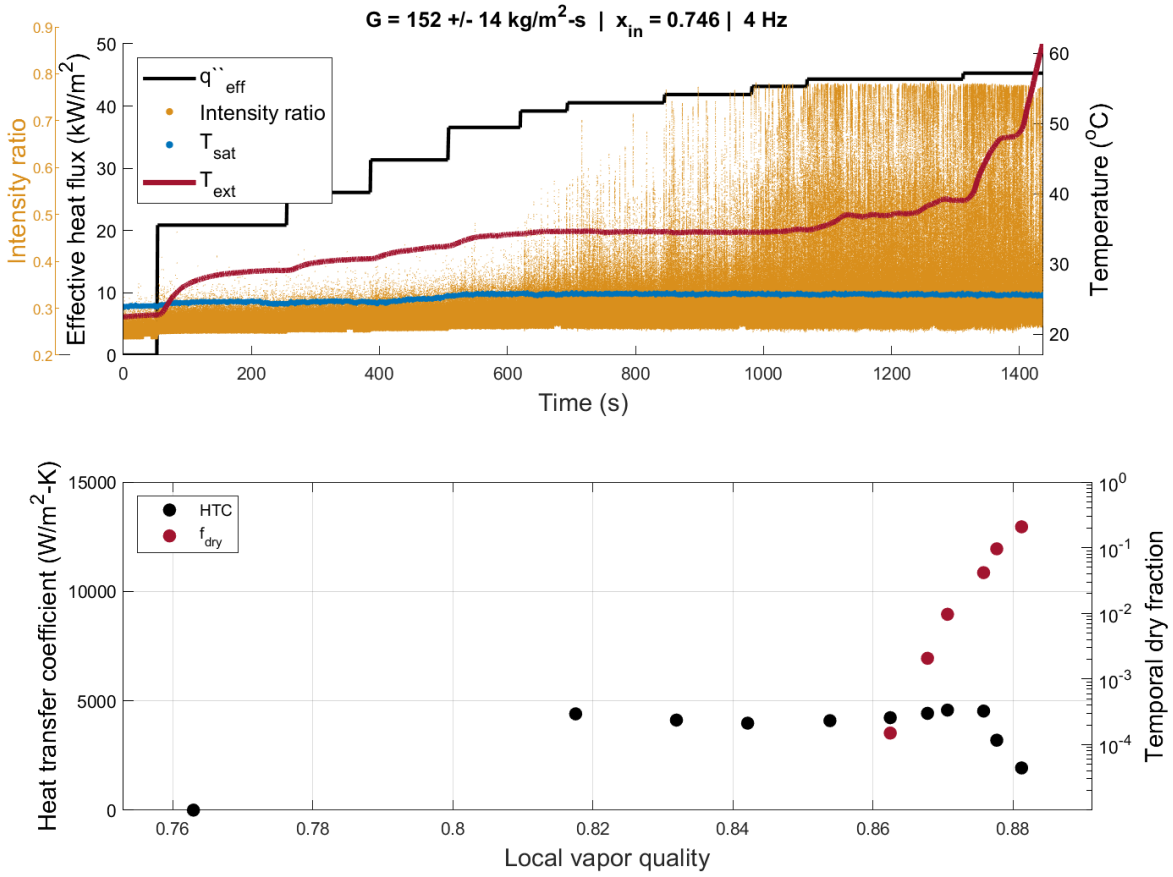

Figure 30: Time trace (top), and time-averaged HTC and f_{dry} as a function of x.

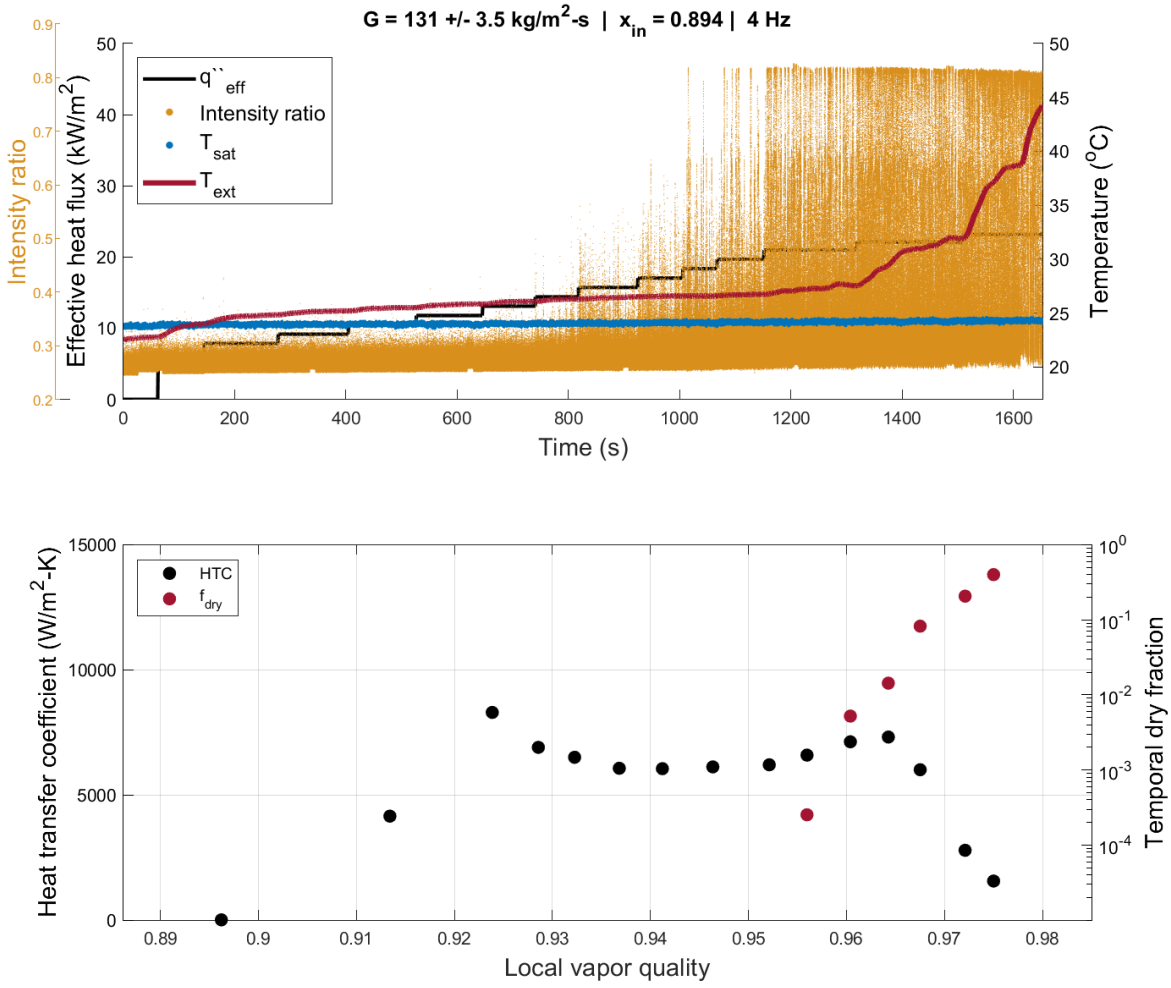

Figure 31: Time trace (top), and time-averaged HTC and f_{dry} as a function of x.

.13 Steady (i.e. no pulses)

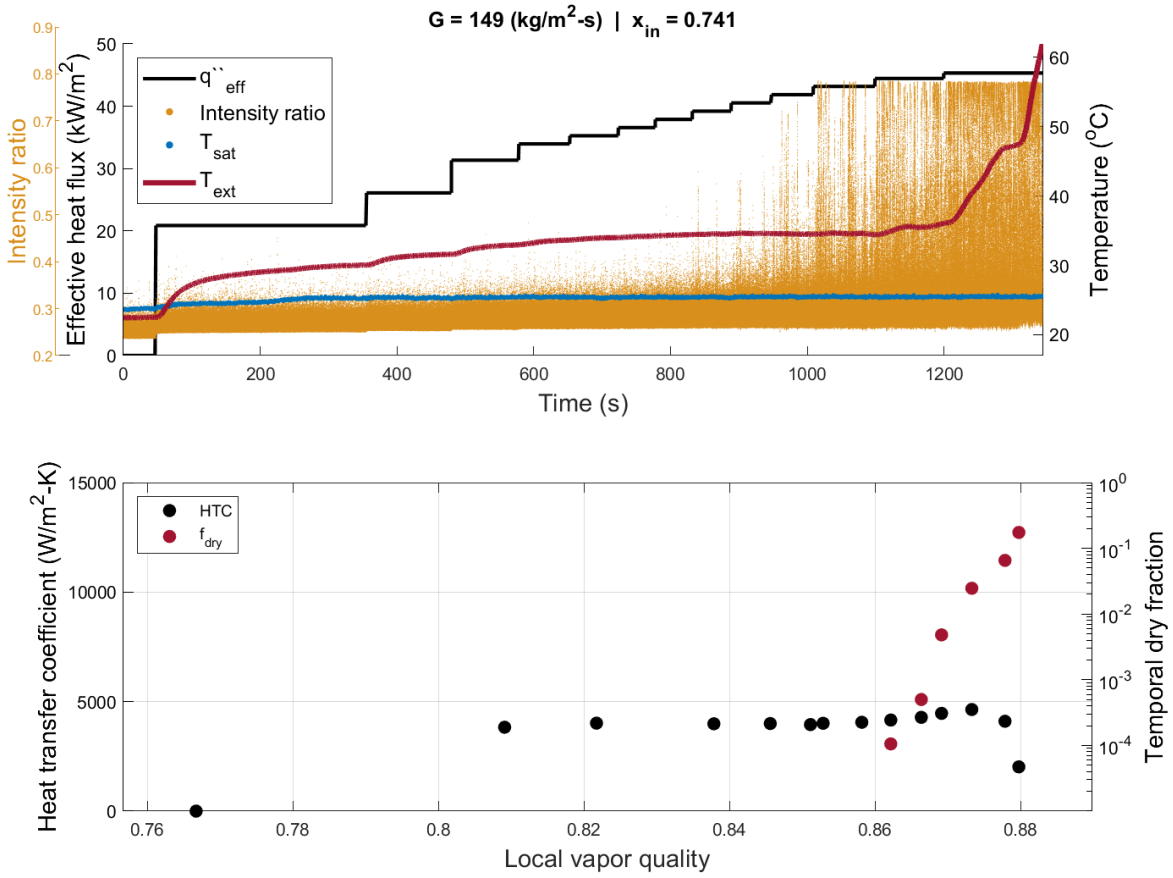

Figure 32: Time trace (top), and time-averaged HTC and f_{dry} as a function of x.

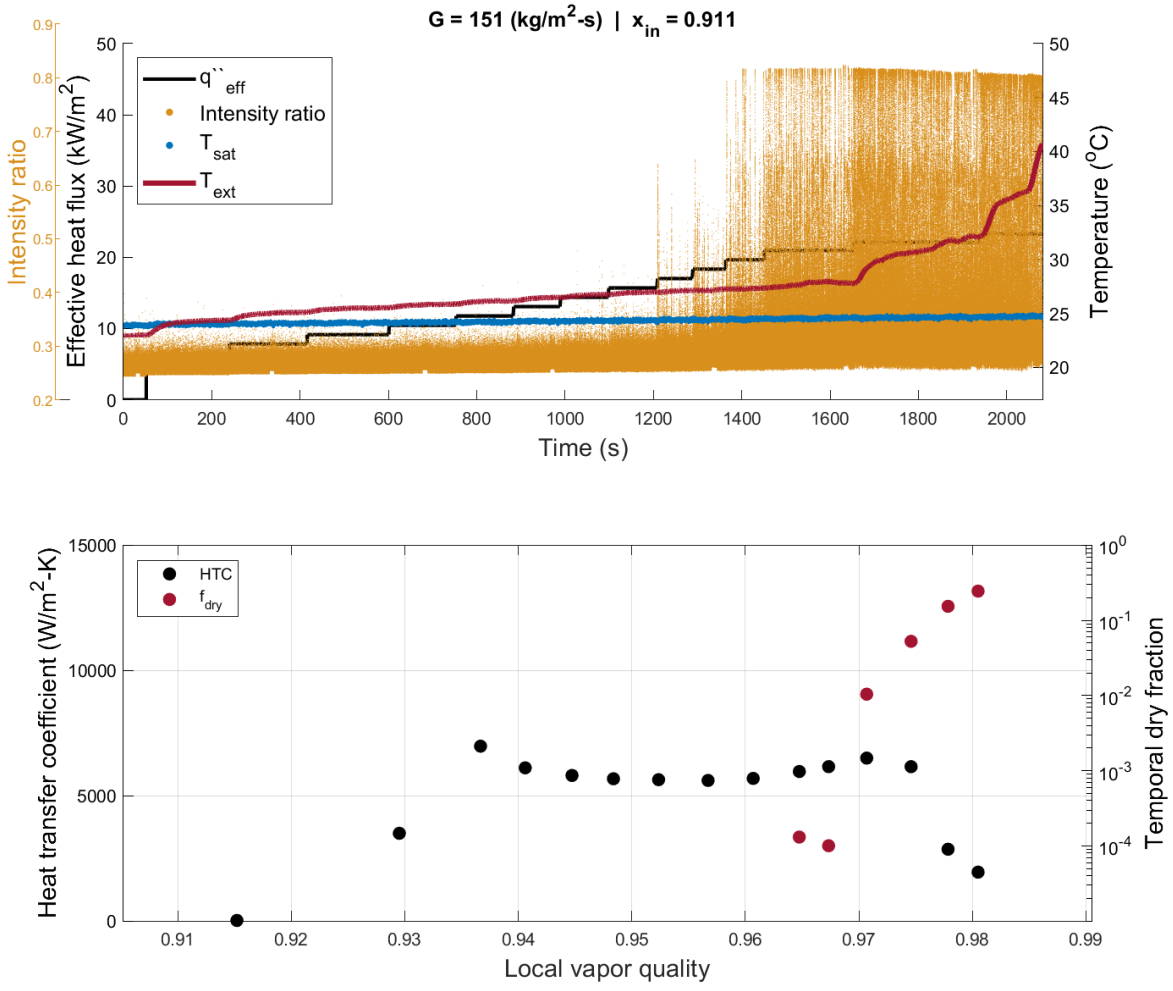

Figure 33: Time trace (top), and time-averaged HTC and f_{dry} as a function of x.

Film thickness steady flow

.14 0.5 Hz pulses

.14.1 Pulses of ± 10% of G - condition 1

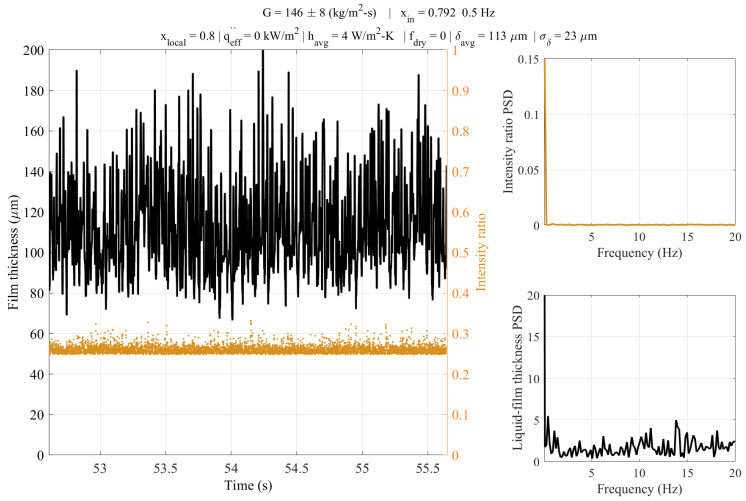

Figure 34: Time trace of liquid-film thickness and laser reflectance measurements for 0.5 Hz pulses. — 1 of 10

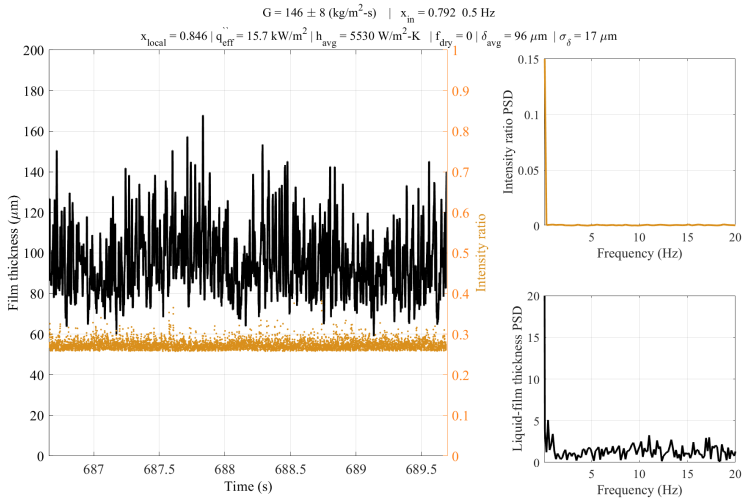

Figure 35: Time trace of liquid-film thickness and laser reflectance measurements for 0.5 Hz pulses. — 3 of 10

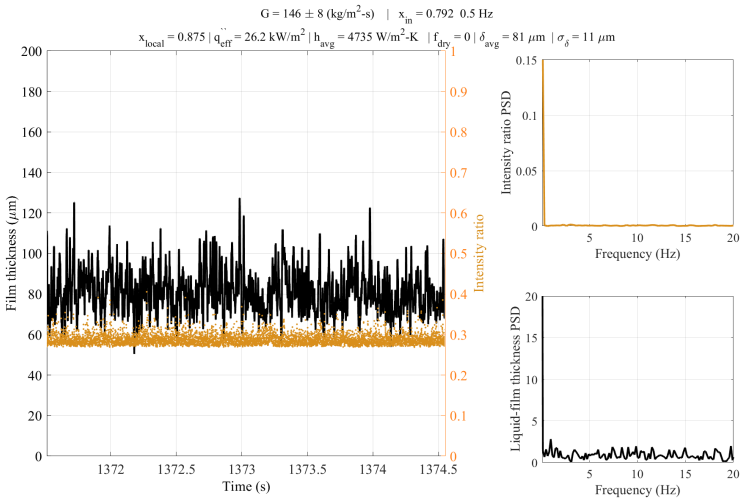

Figure 36: Time trace of liquid-film thickness and laser reflectance measurements for 0.5 Hz pulses. — 5 of 10

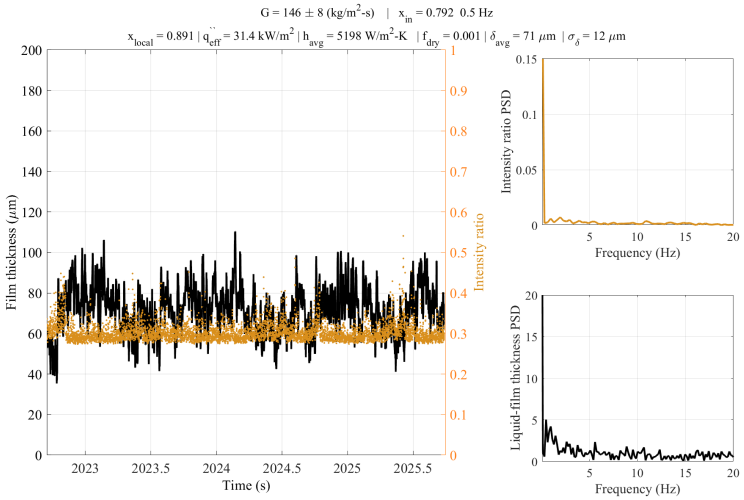

Figure 37: Time trace of liquid-film thickness and laser reflectance measurements for 0.5 Hz pulses. — 7 of 10

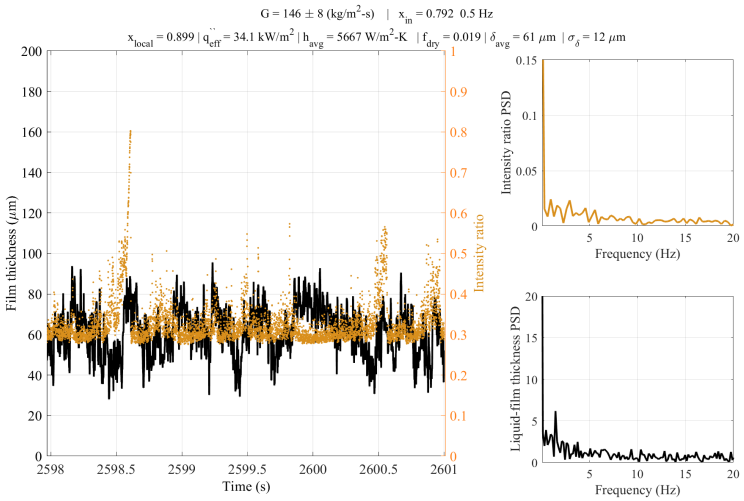

Figure 38: Time trace of liquid-film thickness and laser reflectance measurements for 0.5 Hz pulses. — 9 of 10

.14.2 Pulses of ± 15% of G - condition 1

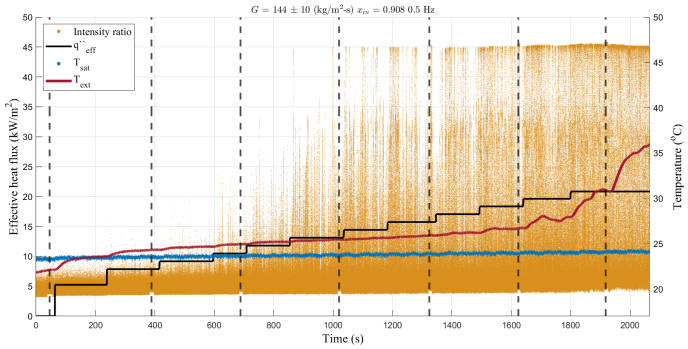

(a) Time trace for 0.5 Hz pulses.

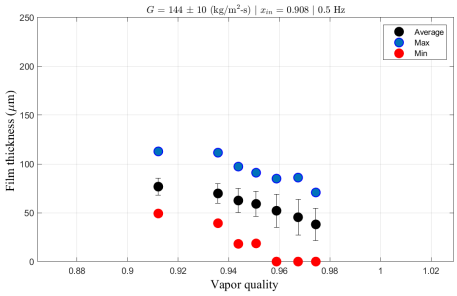

(b) Liquid-film thickness as a function of vapor quality for 0.5 Hz pulses

Figure 39: Data for 0.5 Hz pulses

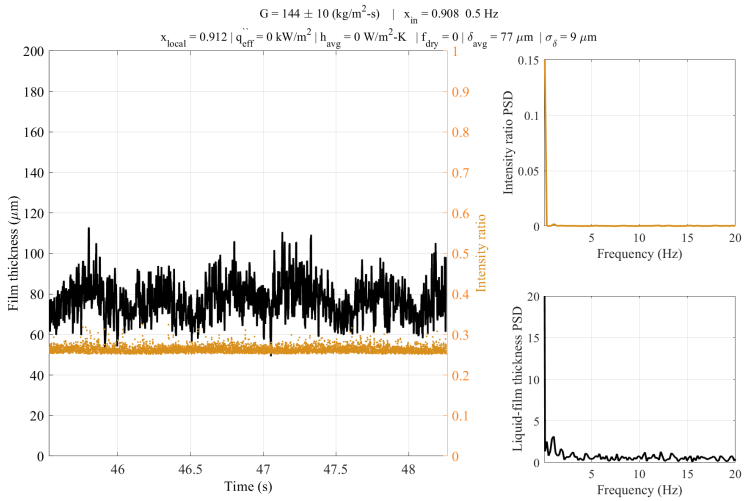

Figure 40: Time trace of liquid-film thickness and laser reflectance measurements for 0.5 Hz pulses. — 1 of 7

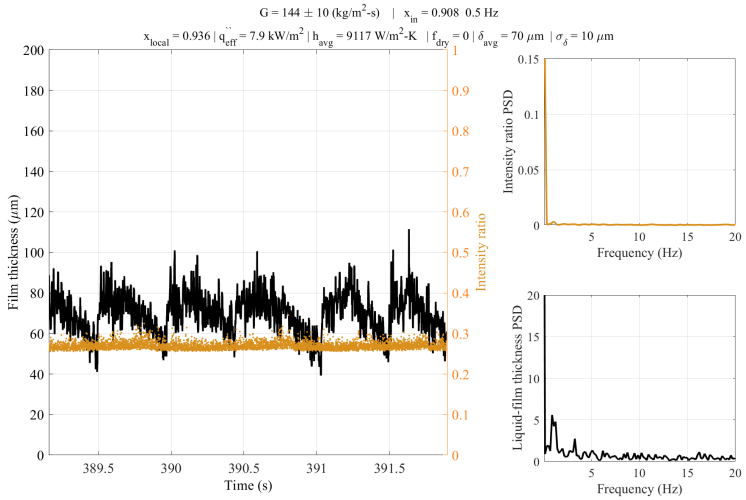

Figure 41: Time trace of liquid-film thickness and laser reflectance measurements for 0.5 Hz pulses. — 2 of 7

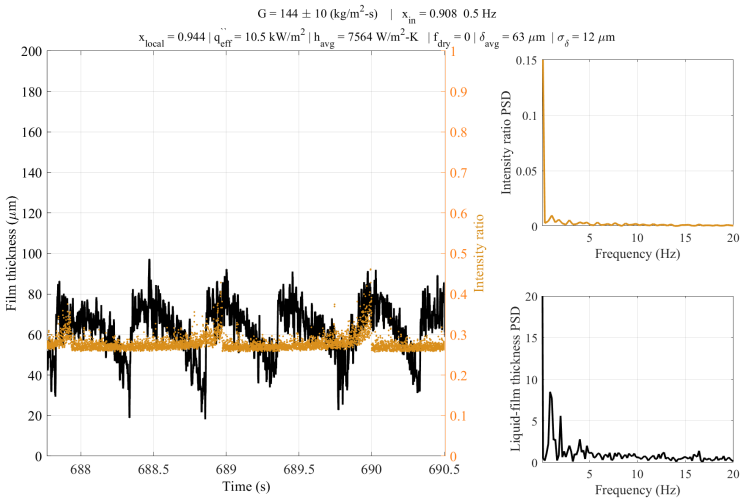

Figure 42: Time trace of liquid-film thickness and laser reflectance measurements for 0.5 Hz pulses. — 3 of 7

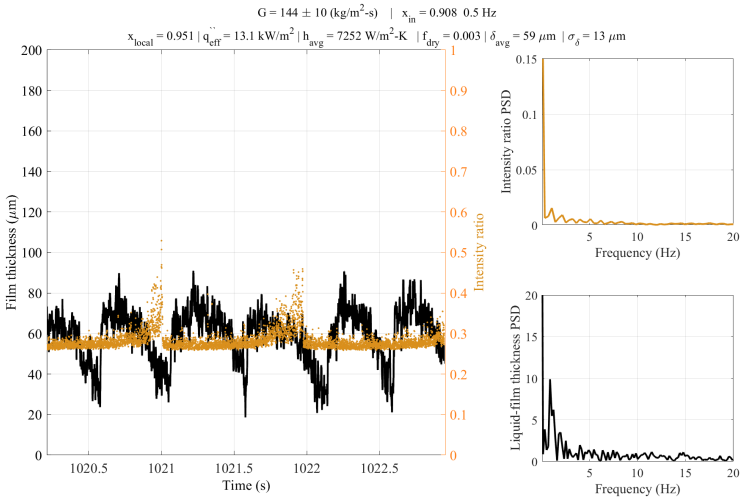

Figure 43: Time trace of liquid-film thickness and laser reflectance measurements for 0.5 Hz pulses. — 4 of 7

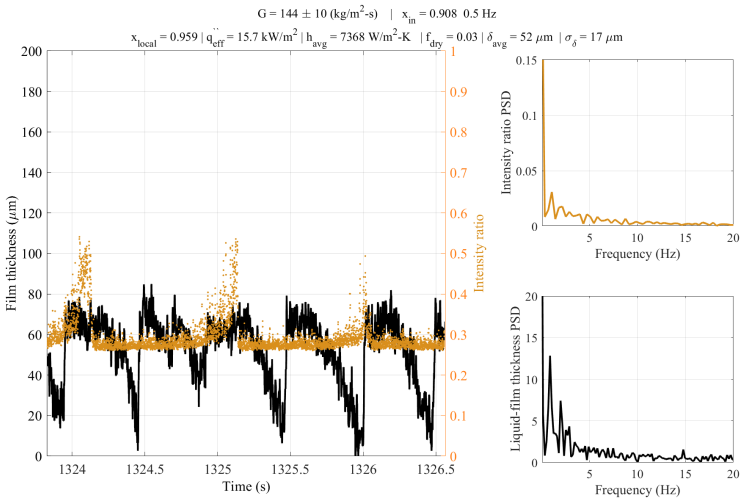

Figure 44: Time trace of liquid-film thickness and laser reflectance measurements for 0.5 Hz pulses. — 5 of 7

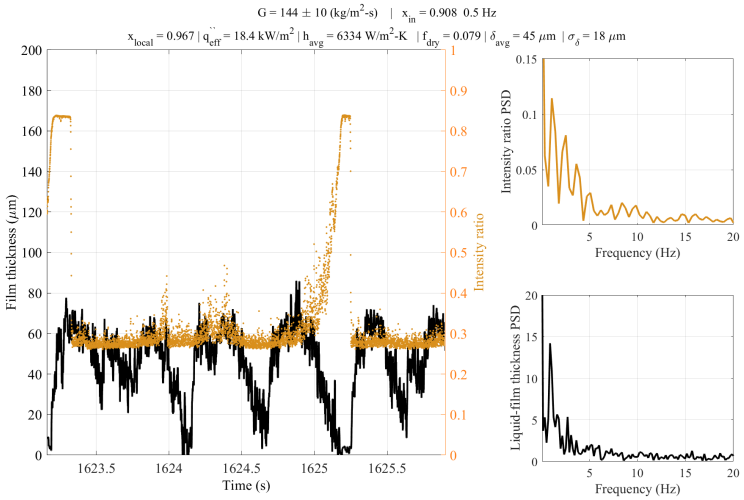

Figure 45: Time trace of liquid-film thickness and laser reflectance measurements for 0.5 Hz pulses. — 6 of 7

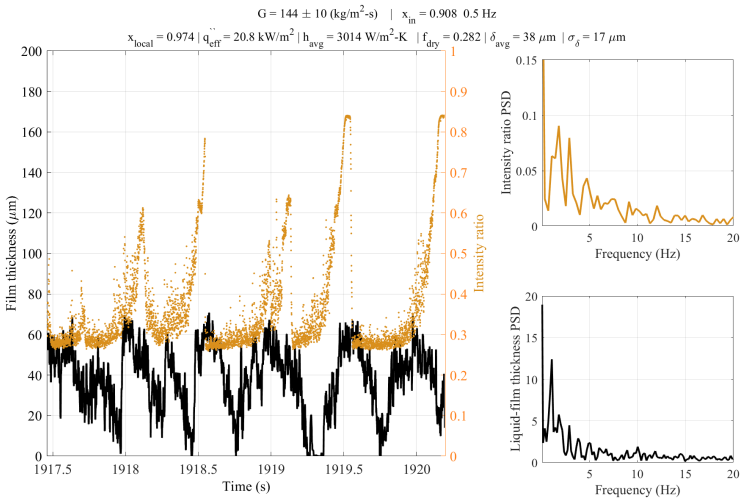

Figure 46: Time trace of liquid-film thickness and laser reflectance measurements for 0.5 Hz pulses. — 7 of 7

.15 1 Hz pulses

.15.1 Pulses of ± 10% of G - condition 1

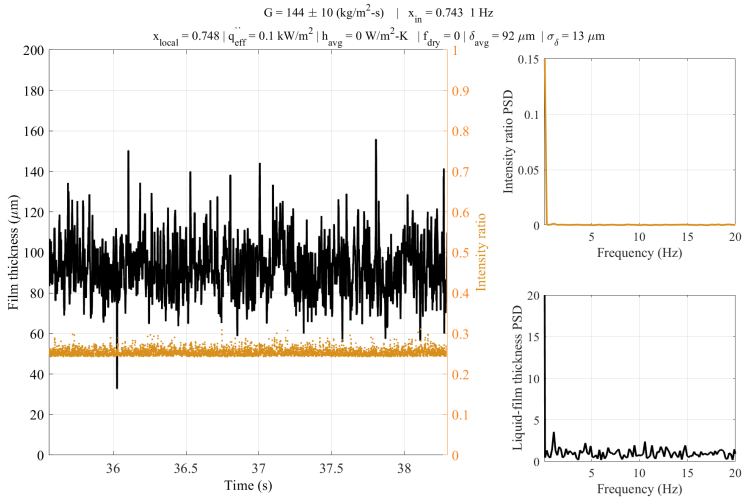

Figure 47: Time trace of liquid-film thickness and laser reflectance measurements for 1 Hz pulses. — 1 of 8

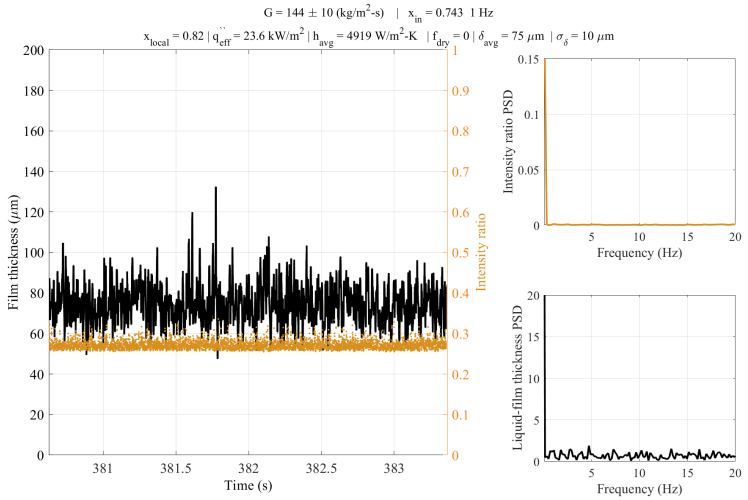

Figure 48: Time trace of liquid-film thickness and laser reflectance measurements for 1 Hz pulses. — 2 of 8

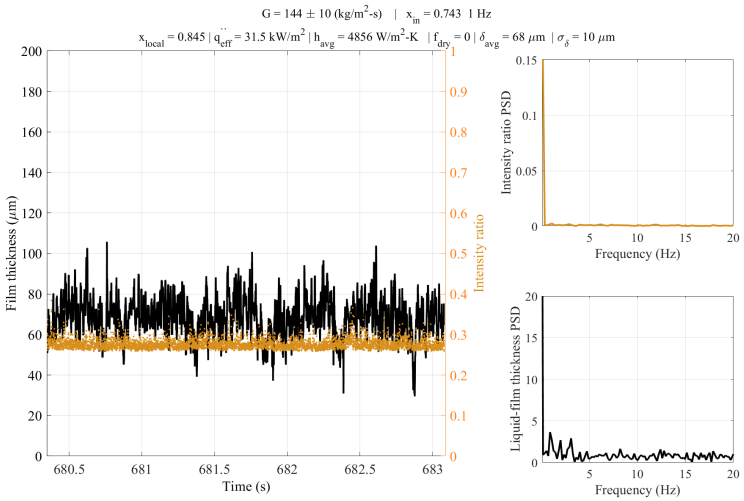

Figure 49: Time trace of liquid-film thickness and laser reflectance measurements for 1 Hz pulses. — 3 of 8

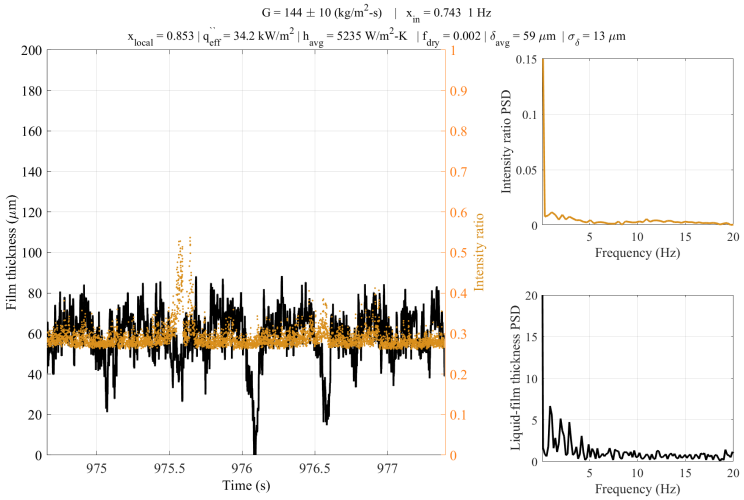

Figure 50: Time trace of liquid-film thickness and laser reflectance measurements for 1 Hz pulses. — 4 of 8

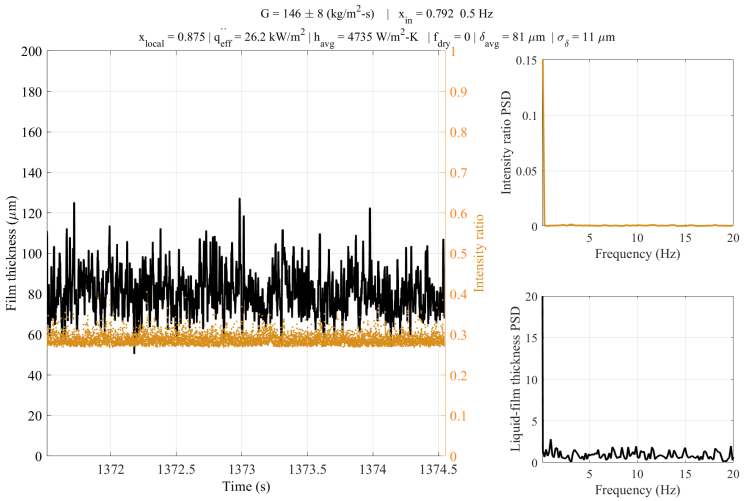

Figure 51: Time trace of liquid-film thickness and laser reflectance measurements for 1 Hz pulses. — 5 of 8

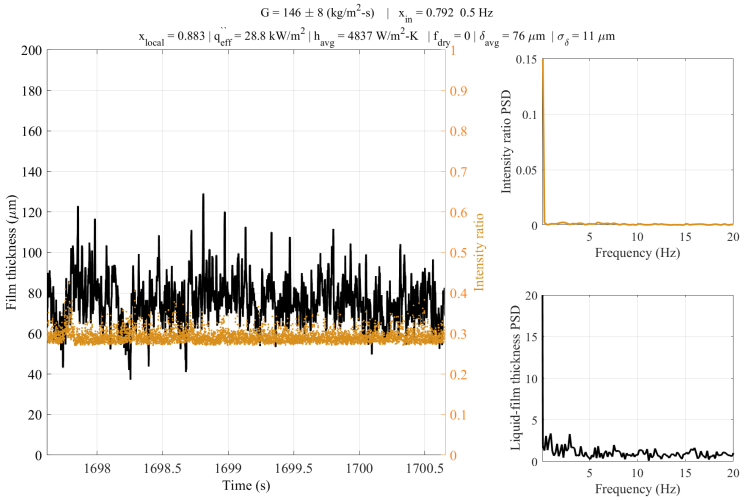

Figure 52: Time trace of liquid-film thickness and laser reflectance measurements for 1 Hz pulses. — 6 of 8

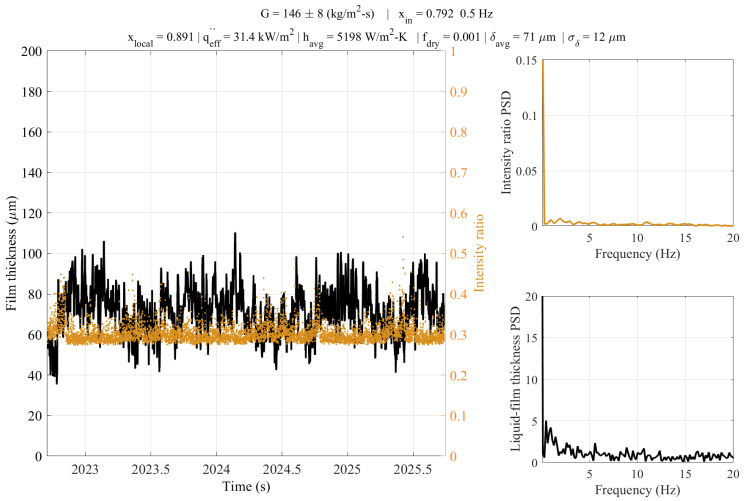

Figure 53: Time trace of liquid-film thickness and laser reflectance measurements for 1 Hz pulses. — 7 of 8

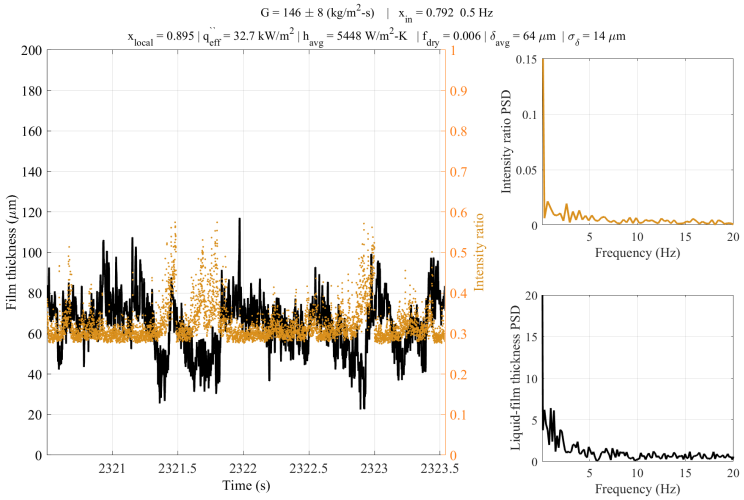

Figure 54: Time trace of liquid-film thickness and laser reflectance measurements for 1 Hz pulses. — 8 of 8

.16 2 Hz pulses

.16.1 Pulses of ± 10% of G - condition 1

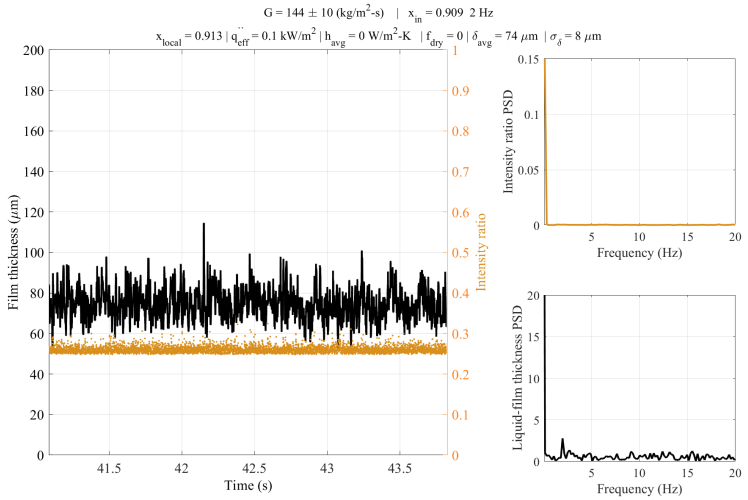

Figure 55: Time trace of liquid-film thickness and laser reflectance measurements for 2 Hz pulses. — 1 of 7

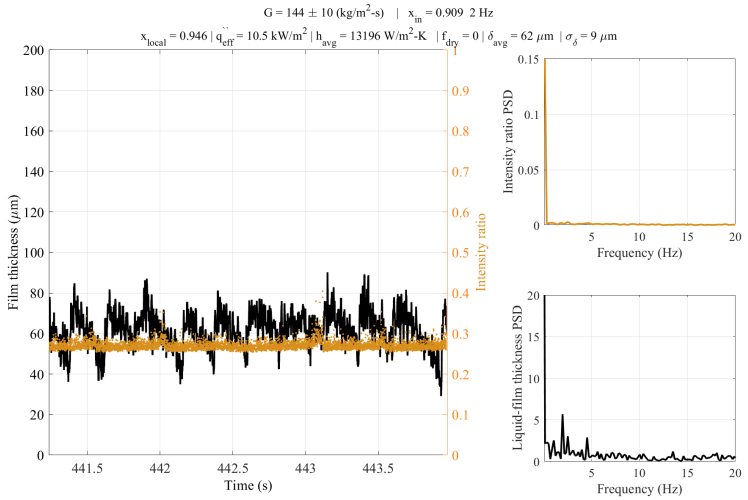

Figure 56: Time trace of liquid-film thickness and laser reflectance measurements for 2 Hz pulses. — 2 of 7

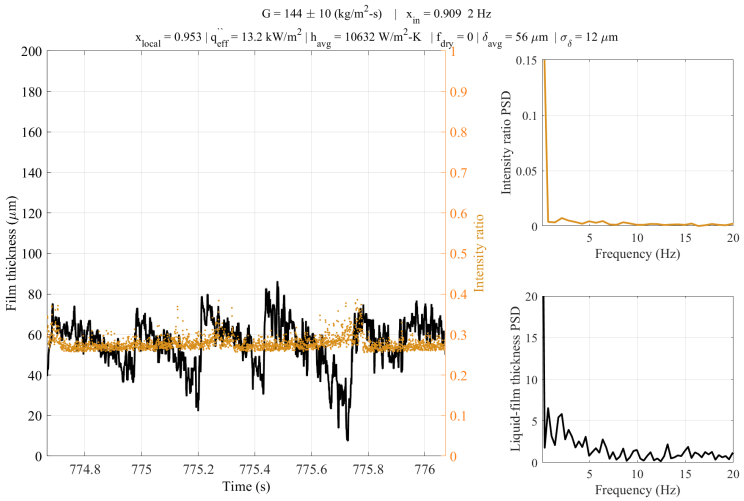

Figure 57: Time trace of liquid-film thickness and laser reflectance measurements for 2 Hz pulses. — 3 of 7

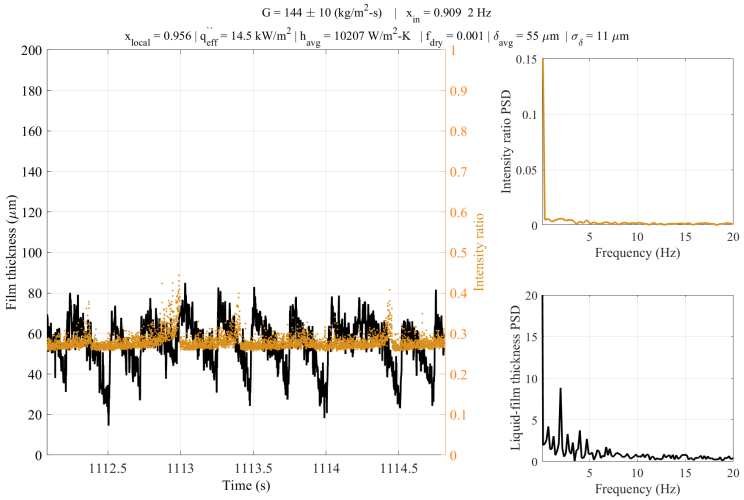

Figure 58: Time trace of liquid-film thickness and laser reflectance measurements for 2 Hz pulses. — 4 of 7

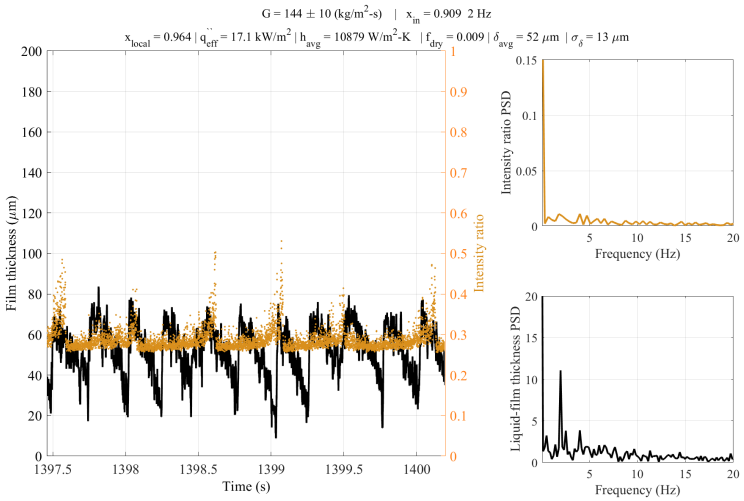

Figure 59: Time trace of liquid-film thickness and laser reflectance measurements for 2 Hz pulses. — 5 of 7

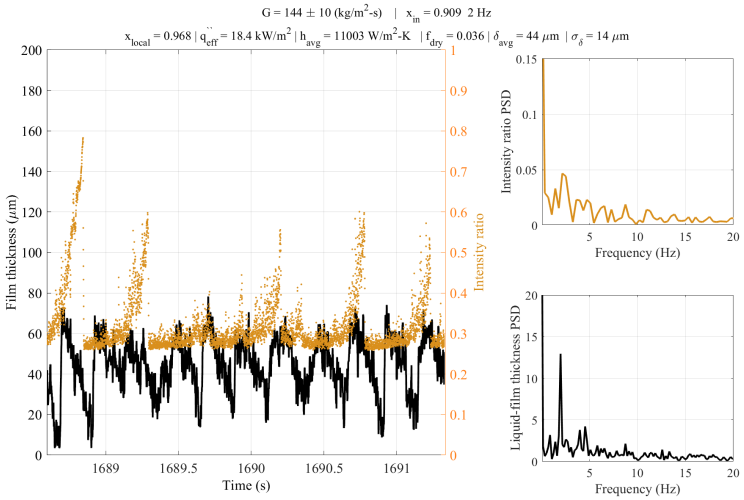

Figure 60: Time trace of liquid-film thickness and laser reflectance measurements for 2 Hz pulses. — 6 of 7

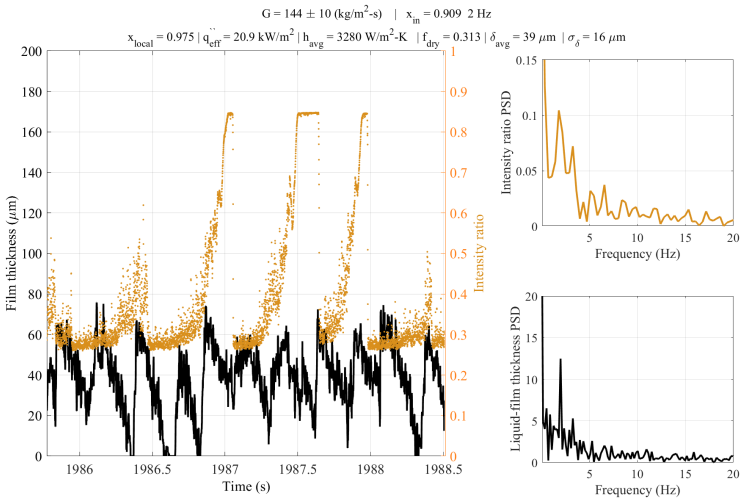

Figure 61: Time trace of liquid-film thickness and laser reflectance measurements for 2 Hz pulses. — 7 of 7

.17 4 Hz pulses

.17.1 Pulses of ± 15% of G - condition 2

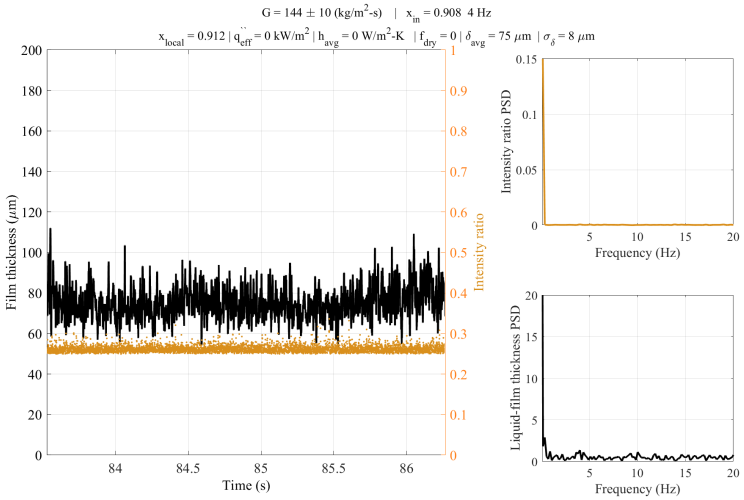

Figure 62: Time trace of liquid-film thickness and laser reflectance measurements for 4 Hz pulses. — 1 of 7

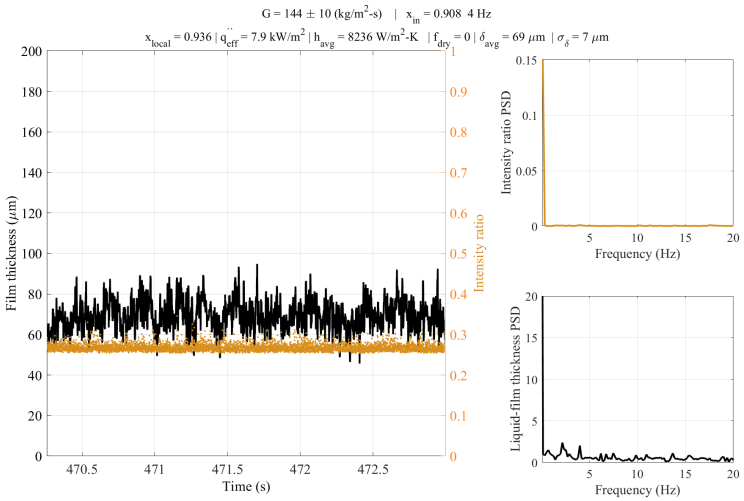

Figure 63: Time trace of liquid-film thickness and laser reflectance measurements for 4 Hz pulses. — 2 of 7

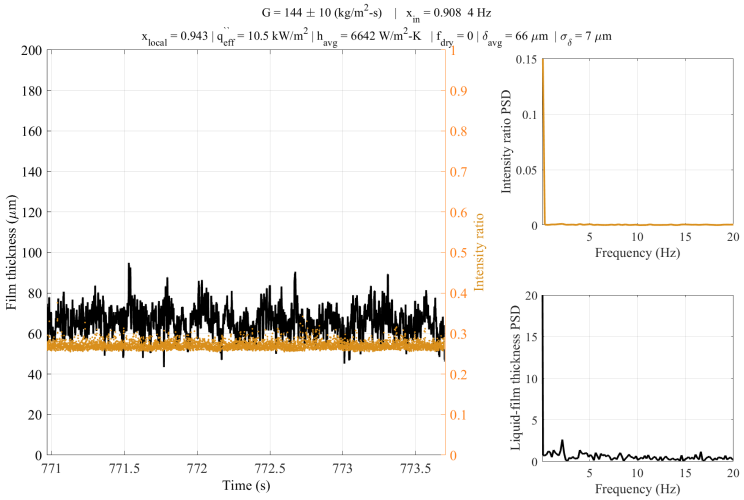

Figure 64: Time trace of liquid-film thickness and laser reflectance measurements for 4 Hz pulses. — 3 of 7

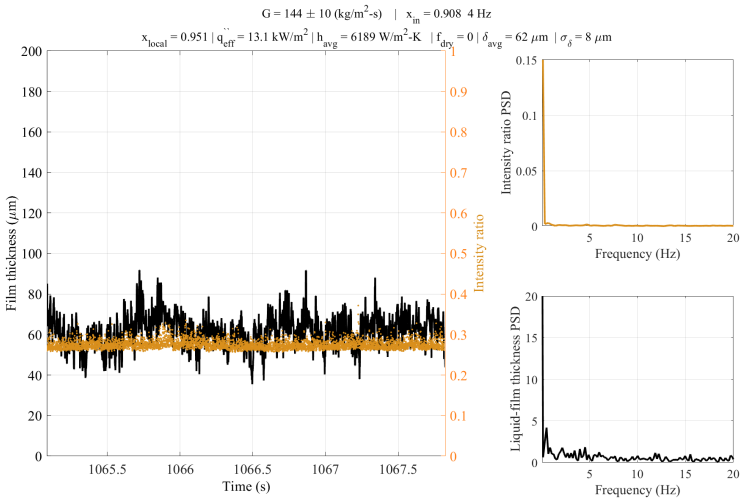

Figure 65: Time trace of liquid-film thickness and laser reflectance measurements for 4 Hz pulses. — 4 of 7

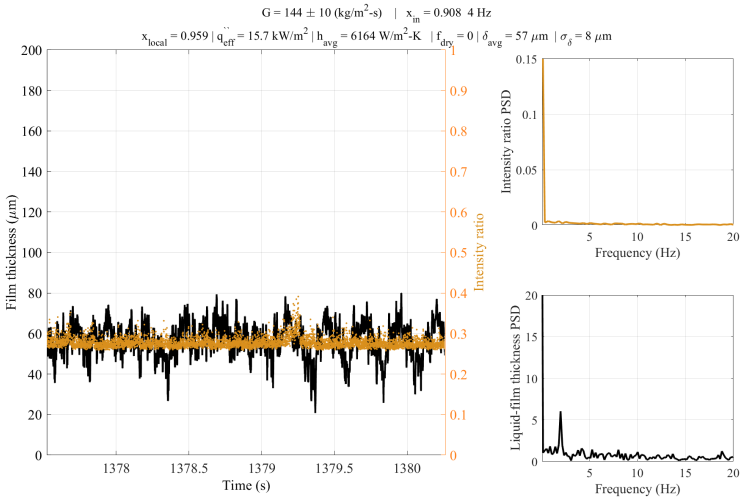

Figure 66: Time trace of liquid-film thickness and laser reflectance measurements for 4 Hz pulses. — 5 of 7

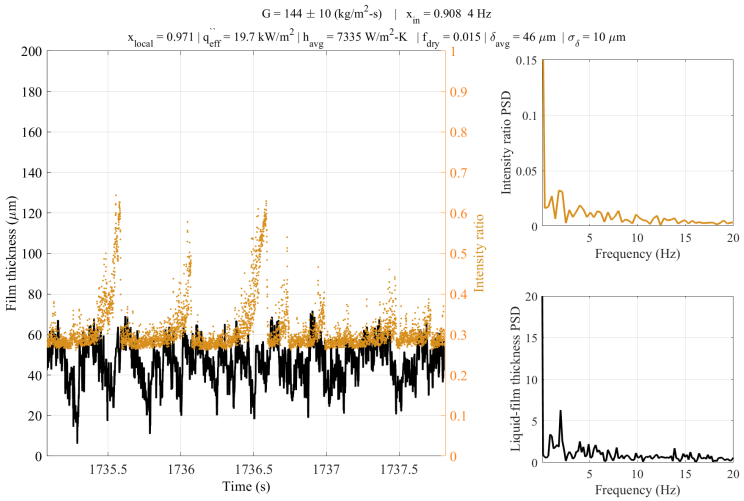

Figure 67: Time trace of liquid-film thickness and laser reflectance measurements for 4 Hz pulses. — 6 of 7

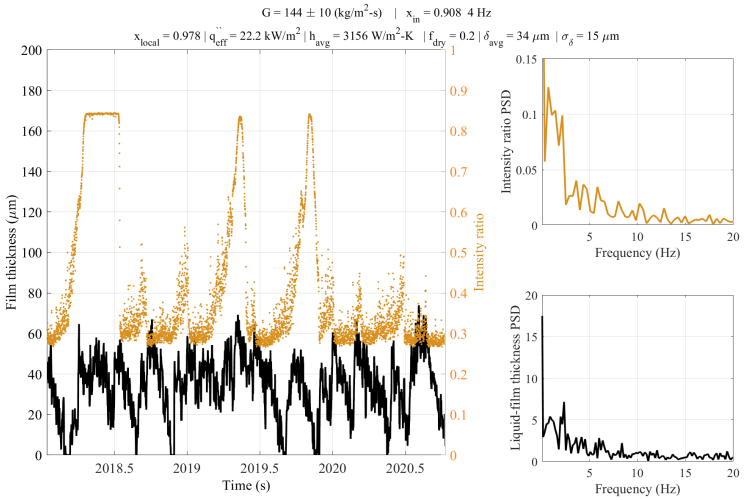

Figure 68: Time trace of liquid-film thickness and laser reflectance measurements for 4 Hz pulses. — 7 of 7